

NANOCRYSTALS AND THIN FILMS OF OXIDE AND CHALCOGENIDE SPINELS FOR  
SPINTRONIC APPLICATIONS

by

YU-HSIANG WANG

A DISSERTATION

Submitted in partial fulfillment of the requirements  
for the degree of Doctor of Philosophy  
in the Department of Chemistry  
in the Graduate School of  
The University of Alabama

TUSCALOOSA, ALABAMA

2010

Copyright Yu-Hsiang Wang 2010  
ALL RIGHTS RESERVED

## ABSTRACT

Spin-based transport in semiconductor systems has been proposed as the foundation of a new class of spintronic devices. For the practical realization of such devices it is important to identify magnetic materials with diverse electronic transport properties (metallic, semiconducting, insulating) and sufficiently high Curie temperature ( $T_C$ ) that can be readily integrated with standard semiconductors. Promising classes of materials for this purpose are the magnetic spinel oxides and chalcogenides. Some of these spinel-based materials are also attractive for biomedical applications.

The facile solution-based synthesis of monodisperse nanocrystals of a wide variety of magnetic ferrites and nanocrystals of the chalcospinel  $\text{CuCr}_2\text{Se}_4$ , along with their structural and magnetic properties, is presented in the first section of the dissertation. The following section presents a theoretical investigation of the electronic band structure of two quaternary chalcospinel systems,  $\text{Cd}_x\text{Cu}_{1-x}\text{Cr}_2\text{Se}_4$  and  $\text{Cd}_x\text{Cu}_{1-x}\text{Cr}_2\text{S}_4$ , and also a number of anion-substituted Cr-based chalcospinels. A wide range of half-metal compositions are predicted both for the cation and anion substituted chalcospinels. The synthesis of spinels has been expanded to the growth of ferrites films using the direct liquid injection chemical vapor deposition (DLI-CVD) technique, which is detailed in the last section of the dissertation. High quality epitaxial  $\text{NiFe}_2\text{O}_4$  films have been grown using this technique with the magnetic properties of the films being comparable to those observed in the bulk, even for films grown at a high deposition rate. The growth of other thin film ferrites, such as lithium ferrite and barium hexaferrite, which are useful for higher frequency microwave applications are being investigated. The eventual goal is to use extend the DLI-CVD technique for the synthesis of chalcospinels films - in particular those

predicted to be half-metallic - which have the potential for a variety of applications in spintronic devices.

## LIST OF ABBREVIATIONS AND SYMBOLS

<i>GMR</i>	giant magnetoresistance
<i>fcc</i>	face-centered cubic
<i>CMR</i>	colossal magnetoresistance
<i>Spintronics</i>	spin-electronics or magnetoelectronics
<i>pH</i>	acidity or basicity of solution
<i>FM</i>	ferromagnet
<i>CIP</i>	current in plane
<i>CPP</i>	current perpendicular to the plane
<i>TMR</i>	tunneling magnetoresistance
<i>MTJ</i>	magnetic tunneling junction
<i>MRAM</i>	magnetoresistive random access memory
<i>P</i>	spin polarization
<i>DOS</i>	density of state
$n^{\uparrow}$	density of state for spin "up" electrons
$n^{\downarrow}$	density of state for spin "down" electrons
<i>LSMO</i>	$\text{La}_{0.7}\text{Sr}_{0.3}\text{MnO}_3$
$\mu\text{B}$	Bohr magneton
$\chi$	susceptibility
$T_c$	Curie temperature
<i>CVD</i>	chemical vapor deposition
<i>DLI-CVD</i>	direct liquid injection chemical vapor deposition

<i>PLD</i>	pulsed laser deposition
<i>XRD</i>	x-ray diffraction
<i>XRR</i>	x-ray reflection
<i>TEM</i>	transmission electron microscopy
<i>AFM</i>	atomic force microscopy
<i>SEM</i>	scanning electron microscopy
<i>AGM</i>	alternating gradient magnetometer
<i>VSM</i>	vibrating samples magnetometer
<i>SQUID</i>	superconducting quantum interference device
<i>d</i>	the lattice plane spacing
$\theta$	the angle between the incident ray and the scattering planes or Bragg angle for the x-ray source wavelength
$\beta$	the line broad at the full width at half maximum
<i>FWHM</i>	the full width at half maximum
$\omega$	out-of-plane tilt angle
$\phi$	in-plane rotation angle
$\psi$	azimuth angle
<i>XRR</i>	x-ray reflectivity
<i>RF</i>	radiofrequency
<i>DC</i>	direct current
<i>BSE</i>	back-scattering electrons
<i>h</i>	Planck's constant
<i>VASP</i>	Vienna <i>ab initio</i> simulation package

<i>DFT</i>	density function theory
$E_F$	Fermi energy
<i>GGA</i>	generalized gradient approximation
<i>LSDA</i>	local spin density approximation
$M_S$	saturation magnetization
$H$	magnetic field
<i>Oe</i>	Oersted
$T$	Tesla
$u$	parameter associated with the anion- sublattice distortion from cubic-close packing
<i>OLA</i>	oleylamine
<i>ODE</i>	1-octadecene
<i>acac</i>	acetylacetonate

## ACKNOWLEDGMENTS

This research would not have been possible without the support of faculty members, friends, and many colleagues who have assisted me throughout my research work. First of all, I am obliged to Dr. Arunava Gupta, my research advisor and the chairman of this dissertation, for patient guidance and uninterrupted encouragement on the research project during the past five years. I would also like to thank all of my committee members, Dr. William Butler, Dr. David Nikles, Dr. Martin Bakker and Dr. Gregory Szulczewski for their invaluable input, inspiring questions, and support of both the dissertation and my academic progress. I would like to thank Dr. William Butler, Dr. Mairbek Chshiev, and Dr. Claudia Mewes for their assistance in the theoretical calculations. Additionally, I would like to express my gratitude to Dr. Kevin Shaughnessy and Dr. Thomas Vaid for valuable advice on the synthesis of metal complexes for thin film applications; Dr. Robin Roger and his group for data collection and analysis of metal-complex single crystals; Dr. Ken Belmore and Dr. Qiaoli Liang for collecting NMR and mass spectra and analyses; and to the staff members of the chemistry department and the MINT Center. Without their help and support the research work could not have been completed.

I have been lucky to have had the opportunity to work with wonderful colleagues in our research group. Specially, I would like to thank Dr. Prahallad Padhan, Dr. Ningzhong Bao, Dr. Jianxing Ma, Ms. Liming Shen and Mr. Ning Li for their helpful suggestions and inputs and scientific discussions.

Finally, thanks to my friends outside of work and my family who never stopped encouraging and supporting me.

# CONTENTS

ABSTRACT.....	ii
LIST OF ABBREVIATIONS AND SYMBOLS .....	iv
ACKNOWLEDGMENTS .....	vii
LIST OF TABLES .....	xi
LIST OF FIGURES .....	xii
1. INTRODUCTION TO SPINELS, NANOCRYSTALS AND SPINTRONICS.....	1
1.1 Spinels.....	2
1.2 Nanocrystals.....	4
1.3 Spintronics .....	7
1.4 Half Metals.....	13
1.5 References.....	15
2. EXPERIMENTAL TECHNIQUES.....	19
2.1 Wet Chemical Synthesis Setup .....	19
2.2 Chemical Vapor Deposition Technique.....	20
2.3 X-ray Diffraction/X-ray Reflectivity .....	22
2.4 Atomic Force Microscopy .....	25
2.5 Vibrating Sample Magnetometer.....	25
2.6 Alternating Gradient Magnetometer .....	26
2.7 Superconducting Quantum Interference Device.....	27
2.8 Scanning Electron Microscopy.....	28
2.9 Transmission Electron Microscopy .....	28

2.10 Vienna <i>ab-initio</i> Simulation Package .....	30
2.10.1 Density Function Theory .....	30
2.10.2 Generalized Gradient Approximation.....	33
2.10.3 The Calculation Parameters of VASP.....	34
2.10.3.1 INCAR File.....	34
2.10.3.2 KPOINTS File .....	35
2.10.3.3 POSCAR File.....	36
2.10.3.4 POTCAR File.....	37
2.11 References.....	37
<b>3. SYNTHESIS OF FERRITES AND COPPER CHROMIUM SELENIDE NANOCRYSTALS .....</b>	<b>39</b>
3.1 Synthesis of Monodisperse Ferrite Nanocrystals and Nanostructures .....	39
3.1.1 Synthesis of Monodisperse Metal Ferrite Nanocrystals .....	40
3.1.2 Synthesis of Spherical and Rod-Like $\text{CoFe}_2\text{O}_4$ Nanostructures .....	44
3.2 Size-Controlled Synthesis of $\text{CuCr}_2\text{Se}_4$ Nanocrystals .....	48
3.2.1 Introduction .....	48
3.3 Experimental of $\text{CuCr}_2\text{Se}_4$ Nanocrystals .....	49
3.3.1 Synthesis of 1-Octadecene/Selenium Complex .....	49
3.3.2 Synthesis of Magnetic $\text{CuCr}_2\text{Se}_4$ Nanocrystals.....	50
3.4 Characterizations of $\text{CuCr}_2\text{Se}_4$ Nanocrystals .....	52
3.5 References.....	59
<b>4. FIRST-PRINCIPLES CALCULATIONS ON CHROMIUM-BASED CHALCOSPINELS .....</b>	<b>62</b>

4.1 Introduction.....	62
4.2 Simulation Package and Parameters .....	64
4.3 Results of Tetrahedral Site Substitutions.....	65
4.4 Results of Anion Site Substitutions .....	70
4.5 References.....	77
5. THIN FILM GROWTH OF NICKEL FERRITE.....	79
5.1 Introduction.....	79
5.2 Experimental .....	82
5.3 Results and Discussions.....	84
5.4 References.....	89
6. CONCLUSIONS.....	91
APPENDIX	
I. SYNTHESIS OF TERNARY AND QUATERNARY $\text{CuIn}_x\text{Ga}_{1-x}\text{Se}_2$ ( $0 \leq x \leq 1$ ) SEMICONDUCTOR NANOCRYSTALS .....	93
II. SHAPE-CONTROLLED SYNTHESIS OF SEMICONDUCTOR $\text{CuFeS}_2$ NANOCRYSTALS .....	104

## LIST OF TABLES

1.1 A list of spinel-based materials exhibiting interesting properties.....	2
3.1 The experimental values of the molecular Curie constant $C_M$ , effective magnetic moments in $\mu_B$ per Cr ion, saturation magnetization in $\mu_B$ per f.u. at $T = 5$ K, Curie-Weiss temperature $\theta$ , and Curie temperature $T_C$ for different size $\text{CuCr}_2\text{Se}_4$ nanocrystal samples.....	58
4.1 Calculated structural and magnetic properties of relaxed $\text{Cd}_x\text{Cu}_{1-x}\text{Cr}_2\text{Se}_4$ and $\text{Cd}_x\text{Cu}_{1-x}\text{Cr}_2\text{S}_4$ supercells, along with comparison with the experimental data: lattice parameters, $u$ parameters, and low temperature magnetic moment .....	70
4.2 Calculated structural and magnetic properties of relaxed $\text{CuCr}_2\text{S}(\text{Se})_{4-x}\text{E}_x$ ( $\text{E}=\text{F}, \text{Cl}, \text{Br}$ ), $\text{Cu}(\text{Cd})\text{Cr}_2\text{S}(\text{Se})_{4-x}$ and $\text{CdCr}_2\text{S}(\text{Se})_{4-x}\text{D}_x$ ( $\text{D}=\text{N}, \text{P}, \text{As}$ ) supercells, along with comparison with the experimental data: lattice parameters, $u$ parameters, and low temperature magnetic moment .....	76
5.1 The properties of $\text{NiFe}_2\text{O}_4$ films grown on $\text{MgO}$ and $\text{MgAl}_2\text{O}_4$ substrates at different temperatures .....	86

## LIST OF FIGURES

1.1 Structure of chalcospinel $\text{CdCr}_2\text{Se}_4$ showing the octahedral (blue) and tetrahedral (yellow) site position of Cr and Cd ions in the lattice .....	3
1.2 Spin-dependent transport in a GMR structure: (a) antiparallel configuration and (b) parallel configuration .....	7
1.3 GMR structure of (a) CIP and (b) CPP geometry .....	8
1.4 Writing (a) and reading (b) process of MTJ MRAM memory array ...	12
1.5 Schematics of the difference in the density of states between a ferromagnet (a) and half-metallic ferromagnet (b).....	13
2.1 Schematic diagram of the nanocrystal synthesis apparatus .....	19
2.2 Schematic diagram of a general CVD system .....	20
2.3 Schematic diagram of a direct liquid injection CVD system.....	21
2.4 (a) A schematic drawing illustrating Bragg's law; (b) a schematic view of the different angles involved in a XRD measurement .....	22
2.5 Schematic diagram of AFM and inset is an image of the AFM tip .....	25
2.6 Schematic diagram of the VSM instrument.....	26
2.7 Schematic diagram of SQUID using a Josephson junction .....	27
2.8 Basic transmission electron microscopy component layout .....	29
2.9 Schematic drawing of eight layers in 28 atom supercell spinel structure .....	34
3.1 TEM images of $\text{MFe}_2\text{O}_4$ nanocrystals: (A1) $\text{CoFe}_2\text{O}_4$ ; (B1) $\text{NiFe}_2\text{O}_4$ ; (C1) $\text{MnFe}_2\text{O}_4$ ; (D1) $\text{FeFe}_2\text{O}_4$ ( $\text{Fe}_3\text{O}_4$ ). The corresponding high resolution TEM image of the individual nanocrystals is shown in the inset .....	41

3.2 XRD patterns of $MFe_2O_4$ nanocrystals: (A) $CoFe_2O_4$ ; (B) $NiFe_2O_4$ ; (C) $MnFe_2O_4$ ; (D) $FeFe_2O_4$ ( $Fe_3O_4$ ) .....	42
3.3 Room-temperature magnetic hysteresis of $MFe_2O_4$ nanocrystals: (A) $CoFe_2O_4$ ; (B) $NiFe_2O_4$ ; (C) $MnFe_2O_4$ ; (D) $FeFe_2O_4$ ( $Fe_3O_4$ ). The insets are hysteresis loops of $CoFe_2O_4$ measured at 10 and 300 K (top), and the zero-field-cooled (ZFC) and field-cooled (FC) magnetization of $MnFe_2O_4$ measured in an applied field of 100 Oe (bottom) .....	43
3.4 TEM images of monodisperse self-supported (a-c) spherical and (d-f) cubic nanostructures composed of intergrown spherical and rod-like $CoFe_2O_4$ nanocrystals, respectively .....	45
3.5 (a) Room-temperature hysteresis loops of spherical and cubic nanostructure after 2 min aging at 320°C. (b) The change in the coercivity of spherical and cubic nanostructure versus aging time ....	47
3.6 TEM and HRTEM images of $CuCr_2Se_4$ nanocrystals with an average size of 25 nm .....	52
3.7 X-ray powder diffraction patterns (using a Co $K\alpha$ source, $\lambda = 1.789 \text{ \AA}$ ) of: a) 15 nm and b) 25 nm size NCs .....	53
3.8 Temperature dependence of the ZFC (solid symbols) and FC (open symbols) magnetization for $CuCr_2Se_4$ nanocrystals with different average size: (a) 15 nm, (b) 18 nm, (c) 25 nm, and (d) 30 nm for a magnetic field $H = 50 \text{ Oe}$ . $\Delta M$ is the difference $M_{FC} - M_{ZFC}$ . The same data for samples (e) 15 nm, (f) 18 nm, (g) 25 nm, and (h) 30 nm for $H = 1000 \text{ Oe}$ are shown on the right .....	54
3.9 Field dependence of the magnetization $M$ of $CuCr_2Se_4$ samples: (a) 15 nm, (b) 18 nm, (c) 25 nm and (d) 30 nm measured at $T = 300, 150$ and $5 \text{ K}$ .....	55
3.10 Saturation magnetization moment $M_S$ and coercivity $H_C$ for $CuCr_2Se_4$ samples as derived from Figure 3.4 .....	56
3.11 Fit of the experimental $M(H)$ curves at $T = 300 \text{ K}$ with the Langevin function incorporating a log-normal distribution function with a standard deviation $\sigma$ for samples: (a) 15 nm, (b) 18 nm and (c) 25 nm .....	57
3.12 Temperature dependence of the magnetization per formula unit and inverse magnetic susceptibility for the 25 nm sample .....	58

4.1	Calculated total and individual Cu <i>d</i> , Cr <i>d</i> and S <i>p</i> density of electronic states (DOS) of the Cd <sub>x</sub> Cu <sub>1-x</sub> Cr <sub>2</sub> S <sub>4</sub> system for both the majority and minority spin bands; (a) and (d) are for CuCr <sub>2</sub> S <sub>4</sub> ; (b) and (e) are for CdCr <sub>2</sub> S <sub>4</sub> ; and (c) and (f) are for Cd <sub>0.75</sub> Cu <sub>0.25</sub> Cr <sub>2</sub> S <sub>4</sub> .....	65
4.2	Calculated total and individual Cu <i>d</i> , Cr <i>d</i> and Se <i>p</i> density of electronic states (DOS) of Cd <sub>x</sub> Cu <sub>1-x</sub> Cr <sub>2</sub> Se <sub>4</sub> system for both the majority and minority spin bands; (a) and (d) are for CuCr <sub>2</sub> Se <sub>4</sub> ; (b) and (e) are for CdCr <sub>2</sub> Se <sub>4</sub> ; and (c) and (f) are for Cd <sub>0.5</sub> Cu <sub>0.5</sub> Cr <sub>2</sub> Se <sub>4</sub> .....	66
4.3	Majority and minority energy bands near the Fermi energy (dashed line) along $\Gamma$ -X, $\Gamma$ -K and $\Gamma$ -L directions for (a) Cd <sub>0.5</sub> Cu <sub>0.5</sub> Cr <sub>2</sub> S <sub>4</sub> and (b) Cd <sub>0.5</sub> Cu <sub>0.5</sub> Cr <sub>2</sub> Se <sub>4</sub> .....	68
4.4	Calculated total density of electronic states (DOS) of the CuCr <sub>2</sub> S(Se) <sub>3.5</sub> Br <sub>0.5</sub> , CuCr <sub>2</sub> S(Se) <sub>3.5</sub> , and CdCr <sub>2</sub> S(Se) <sub>3.5</sub> P <sub>0.5</sub> systems for both the majority and minority spin bands .....	71
4.5	The calculated range of ferromagnetic metal (FM), ferromagnetic half-metal (FHM) and ferromagnetic semiconductor (FS) as a function of total valence electrons per formula unit for the different anion substituted systems .....	73
4.6	Majority and minority energy bands near the Fermi energy (dashed line) along $\Gamma$ -X, $\Gamma$ -K and $\Gamma$ -L directions for (a) CuCr <sub>2</sub> S <sub>4</sub> and (b) CuCr <sub>2</sub> S <sub>3.5</sub> Br <sub>0.5</sub> .....	74
4.7	Majority and minority energy bands near the Fermi energy (dashed line) along $\Gamma$ -X, $\Gamma$ -K and $\Gamma$ -L directions for (a) CdCr <sub>2</sub> S <sub>3.5</sub> P <sub>0.5</sub> and (b) CdCr <sub>2</sub> S <sub>4</sub> .....	75
5.1	Phase diagram of hexaferrites .....	80
5.2	$\theta$ - $2\theta$ x-ray diffraction patterns of NiFe <sub>2</sub> O <sub>4</sub> films grown on (a) MgO (100) and (b) MgAl <sub>2</sub> O <sub>4</sub> (100) substrates at various temperatures .....	83
5.3	$\phi$ scan for the (404) reflection of NiFe <sub>2</sub> O <sub>4</sub> films grown on (a) MgO (100) and (b) MgAl <sub>2</sub> O <sub>4</sub> (100) substrates at 650°C .....	84
5.4	AFM images of NiFe <sub>2</sub> O <sub>4</sub> films grown on (a) MgO (100) and (b) MgAl <sub>2</sub> O <sub>4</sub> (100) substrates at 650°C. The SEM Cross-section view of NiFe <sub>2</sub> O <sub>4</sub> films grown on (c) MgO (100) and (d) MgAl <sub>2</sub> O <sub>4</sub> (100) substrates at 650°C .....	85

5.5 The magnetization of  $\text{NiFe}_2\text{O}_4$  films grown on  $\text{MgO}$  (100) and  $\text{MgAl}_2\text{O}_4$  (100) substrates at  $650^\circ\text{C}$ .....87

## CHAPTER 1

### INTRODUCTION TO SPINELS, NANOCRYSTALS AND SPINTRONICS

For the past several decades, the size of materials and devices being investigated and fabricated have been steadily decreasing from micro-scale to the nano-scale. The materials in the nanometer range are referred to as nanomaterials (such as nanoparticles or nanocrystals, nanowires, nanotubes, etc.) and their size is between those of bulk materials and atoms or molecules. Nanomaterials have been studied extensively in recent years because they exhibit many interesting properties that are different from bulk materials such as large surface area, blue shift of the optical absorption and superparamagnetism. For instance, copper nanoparticles that are smaller than 50 nm are considered super hard materials that do not exhibit the same malleability and ductility as bulk copper.<sup>1</sup> Similarly, superparamagnetic nanoparticles have shown great potential for many technological applications, ranging from information storage and electronic devices to medical diagnostics and drug delivery.<sup>2</sup>

Spintronics devices are another example of nanotechnology. Since the discovery of giant magnetoresistance (GMR), the field of spintronics has advanced rapidly and has had a significant impact on storage and memory devices. Because of the dramatic advances in spintronics over the past two decades, the size of information storage devices have decreased down to tens of nanometer range as scientists continue to explore options for increasing the data storage density well beyond 1 Tbit/in<sup>2</sup>. Undoubtedly, nanotechnology will continue to make rapid strides in the coming decades and will have a major impact in various fields of science and technology. Promising classes of materials for spintronics are the magnetic spinel oxides and chalcogenides. Some of these spinel-based materials are also attractive for biomedical applications.

## 1.1 Spinel

The history of spinel, documented in literature, dates back to the sixteenth century.<sup>3</sup> Spinel is an ancient name that originally referred to red gemstones, which today are recognized as crystals of magnesium aluminum oxide,  $\text{MgAl}_2\text{O}_4$ . It was not until the nineteenth century that the common structure of many natural compounds of spinel family came to be appreciated.<sup>4</sup> The list of compounds in Table 1.1 illustrates the amazingly wide variety of spinels.<sup>5</sup> Spinel ferrites have been investigated for almost a century because of their unique magnetic properties that make them suitable for use as permanent magnets, cores for transformers, and in various other applications. Over the years a wide variety of methods have been utilized for the synthesis of these materials, particularly in bulk form, with improved properties for various applications.<sup>6</sup> In recent years the lithium-based spinel  $\text{LiMn}_2\text{O}_4$  has attracted attention as a potential cathode material for lithium-ion batteries because they are cheaper, less toxic and considered safer in the overcharged state.<sup>7</sup>

**Table 1.1** A list of spinel-based materials exhibiting interesting properties.

Compound	Characteristics
$\text{MgAl}_2\text{O}_4$	Spinel itself, base for natural gemstones
$\text{ZnAl}_2\text{O}_4$	Gahnite, a transparent diamagnetic spinel
$\text{FeAl}_2\text{O}_4$	Hercynite, a classical paramagnet
$\gamma\text{-Fe}_2\text{O}_3$	Maghemite, a natural material for magnetic recording
$\text{FeCr}_2\text{O}_4$	Chromite, the chrome ore of Rhodesia
$\text{Mn}_3\text{O}_4$	Hausmannite, a natural tetragonal spinel
$\text{Fe}_3\text{O}_4$	Magnetite, the ancient navigator's lodestone
$\text{Fe}_3\text{S}_4$	Greigite, a ferromagnetic semimetal
$\text{NiFe}_2\text{O}_4$	Trevorite, a ferromagnetic semiconductor
$\text{ZnFe}_2\text{O}_4$	Franklinite, the paramagnetic ferrite
$\text{CuCo}_2\text{S}_4$	Carrollite, a natural metallic spinel
$\text{FeTi}_2\text{O}_4$	Ulvöspinel, with giant magnetostrictive properties
$\text{Mg}_2\text{SiO}_4$	High-pressure spinel polymorph of forsterite (olivine)
$\text{LiV}_2\text{O}_4$	A heavy fermion transition metal oxide
$\text{Fe}_{1-x}\text{Cu}_x\text{Cr}_2\text{S}_4$	A chalcogenide with colossal magnetoresistive properties

Spinel has a complicated crystal structure and has two common forms: normal spinel and inverse spinel. The general formulation of spinel is  $A^{2+}B_2^{3+}X_4^{2-}$  which is based on a cubic-close-packing of anions. It consists of a face-centered cubic (*fcc*) lattice and belongs to the centrosymmetric space group *Fd3m*.<sup>8</sup> *A* is a divalent cation such as Ni, Co, Cu, Cd, Zn or Hg; *B* is a trivalent cation such as Fe, Cr, Mn or Rh; anion site can be O, S, Se and Te. In a *normal* spinel the nominally divalent metal ions *A* occupy the tetrahedral sites (1/8 filled by *A*) and the trivalent ion *B* occupies the octahedral sites (1/2 filled by *B*) as shown in Fig. 1.1. The general

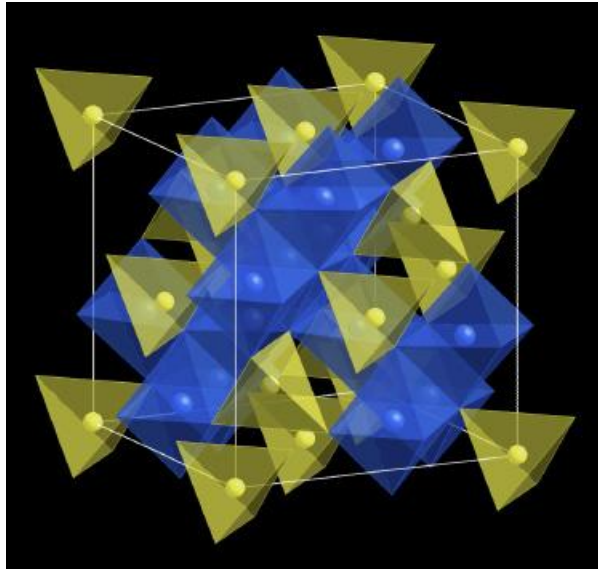


**Figure 1.1** Structure of chalcospinel  $CdCr_2Se_4$  showing the octahedral (blue) and tetrahedral (yellow) site position of Cr and Cd ions in the lattice. Courtesy of Prof. Annett, ref [9].

formula is thus  $A'B_2^oX_4^c$  and a cubic unit cell ( $a \sim 9.75 - 10.75 \text{ \AA}$  for  $X = S, Se$ , as compared to  $\sim 8 - 8.5 \text{ \AA}$  for O) contains 32 *X* anions, 8 *A* cations and 16 *B* cations. *Inverse* spinels are unusual in that the divalent *A* ions switch places with half of the trivalent *B* ions; their general formula is thus  $A'[AB]^oX_4^c$ . A mixed spinel structure is also possible and does exist for some of the chalcogenides over a range of composition. While the degree of covalent bonding plays a key role, the factors determining specific cation arrangements are not yet completely understood.

The II-Cr<sub>2</sub>-VI<sub>4</sub> spinel, which is one of main focus of this dissertation, are unique in adopting

only the *normal* spinel structure because of the clear octahedral preference for the  $\text{Cr}^{3+}$  ( $d^3$ ) ions, resulting in predominant ferromagnetic ordering. This spinel family ( $\text{ACr}_2\text{X}_4$ ; X=Se, Te) has been investigated in some detail, in part motivated by their unique properties. While their oxide counterpart, the spinel oxochromites (X= O), are super-exchange mediated antiferromagnetic insulators, a number of the chalcospinels (chalcogenide spinels) are distinguishably ferri/ferromagnetic insulators, semiconductors or even metals.<sup>10</sup>

Magnetic materials with diverse electronic transport properties (metallic, semiconducting, insulating) and sufficiently high Curie temperature ( $T_C$ ) are needed for room temperature operation of spin-based electronic (spintronic) devices.<sup>11</sup> In view of the high  $T_C$  requirement, the chromium based chalcospinels are potentially attractive candidates. The compounds  $\text{CuCr}_2\text{S}_4$ ,  $\text{CuCr}_2\text{Se}_4$  and  $\text{CuCr}_2\text{Te}_4$  are metallic with Curie temperatures of 377, 430, and 360 K, respectively. Furthermore, a number of the Cr-based chalcospinels have generated renewed interest in recent years because of their unique magnetotransport and magnetodielectric properties. For example, the Cu-chromium chalcogenides exhibit unusual transport properties characterized by a large, temperature-dependent magnetoresistance.<sup>12</sup> Similarly,  $\text{CdCr}_2\text{S}_4$  and  $\text{HgCr}_2\text{S}_4$  display unusual time dependent ferroelectric and colossal magnetocapacitance properties.<sup>13</sup> A dissipationless anomalous Hall current has also been observed in the ferromagnetic spinel  $\text{CuCr}_2\text{Se}_{4-x}\text{Br}_x$ . These observations have provoked strong interest in these materials for possible spintronic applications, including new types of storage media and magnetic memory devices.

## 1.2 Nanocrystals

Inorganic nanocrystals and nanoparticles have received considerable interest because of their

fascinating shape- and size-dependent properties, not only for fundamental scientific research but also for a wide range of technological applications. For example, nanocrystals exhibit size-dependent properties such as quantum confinement in semiconductor nanocrystals,<sup>14</sup> surface plasmon resonance in some metal nanocrystals,<sup>15</sup> and superparamagnetism in magnetic nanocrystals.<sup>16</sup>

Considerable effort has been devoted to preparing monodisperse nanocrystals with controlled size and shape. There are primarily three methods for the synthesis of nanocrystals: thermal decomposition, co-precipitation, and microemulsion. Of these, the thermal decomposition method is the one that is most widely used. Relatively high temperatures are required for this method and a general scheme consists of three components - precursors, organic surfactants and solvent. In some cases, the surfactant also serves as a solvent. The formation of monodisperse nanocrystals generally involves two steps: nucleation of initial seed and its growth. In the nucleation step, the precursors chemically transform to reactive intermediate species leading to homogenous nucleation. The individual nuclei then grow by incorporation of the supersaturated monomers present in the reaction media. This thermolysis approach usually generates nanocrystalline materials in which the constituent atoms or ions having sufficient time and energy to rearrange and anneal during the growth process.<sup>17</sup> The energy correlation to the melting temperature of the solid is therefore a decisive factor in the growth of nanocrystals. Hence, both the choice of suitable reaction temperature and precursors play an important role in the synthesis of monodisperse nanocrystals.

Co-precipitation is a facile method to synthesize nanocrystals from aqueous salt solution of precursors by addition of base under inert atmosphere at room temperature or an elevated temperature. The size, shape and even the composition depend upon the type of salt used (e.g.

chlorides, sulfates, nitrates), the reaction temperature, pH value and ionic strength of the media. In the microemulsion technique a mixture of oil, water and surfactant, frequently in combination with a co-surfactant, is utilized. The aqueous phase may contain the salts and/or other reagents, and the oil may actually be a complex mixture of different hydrocarbons.<sup>18</sup> Both the coprecipitation and microemulsion methods are better suited for nanocrystal synthesis of simple materials, such as metals or binary compounds.

It is important to stabilize the nanocrystals after growth in the form of a colloidal dispersion both for studying their intrinsic properties and various applications. A common route for the preparation of monodisperse nanocrystals is the 'polyol' method based on alcohol (such as ethylene glycol, 1,2-hexadecanediol, polyethylene glycol, etc.) acting as reducing agent of the cation. This technique has been widely used for synthesis of variety of metal and oxide nanocrystals.<sup>16,19</sup> As well as a reducing agent, the polyol reagent can act as a protective agent and solvent for the reaction. This route usually results in highly crystalline nanocrystals that are stabilized with a monolayer of organic molecules, such as oleic acid, trioctylphosphine, octadecene, etc. The surface stabilization avoids agglomeration and aids in forming a colloidal suspension of the nanocrystals.

Nanocrystals are attractive for a broad range of biomedical applications. In particular, magnetic nanocrystals represent an extremely interesting group of inorganic materials having a close connection to living systems.<sup>20</sup> These nanocrystals offer exciting possibilities for use in the detection, manipulation and functional control of biomolecules and cells, with potential medical applications in such diverse area as targeted drug delivery, magnetic fluid hyperthermia and contrast imaging.<sup>21</sup> It is anticipated that the synthesis of compatible core-shell structures, wherein magnetic nanocrystals are encapsulated in a luminescent semiconductor shell such as CdSe, can

lead to dual functionality with novel applications for biological labeling.<sup>22</sup>

### 1.3 Spintronics

Unlike traditional electronics based on the charge of the electron, spintronics aims to additionally exploit the intrinsic spin of the electron and its associated magnetic moment. Spintronics is a term used for ‘spin transport electronics’, first coined by program managers at the Defense Advanced Research Project Agency (DARPA). The origins can be traced back to 1988 with the discovery of the giant magnetoresistance (GMR) by the groups of Albert Fert<sup>23</sup> and Peter Grünberg.<sup>24</sup> However, this phenomenon has been understood since 1936 when Mott

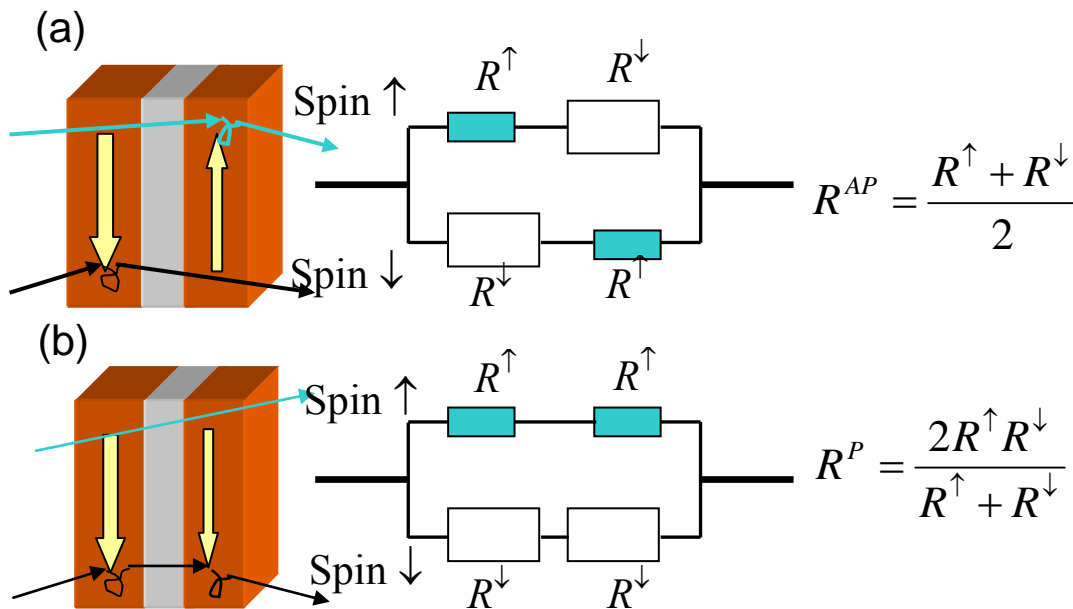


**Figure 1.2** Spin depend transport in a GMR structure: (a) antiparallel configuration and (b) parallel configuration.

explained that at low temperatures the conductivity in a ferromagnet (FM) could be considered as a sum of the two currents arising from the spin up and spin down.<sup>25</sup> This is known as the two spin current model.

A significant effect was observed by Fert and Grunberg when a thin layer of a nonmagnetic

material was sandwiched between two ferromagnetic electrodes (Fig. 1.2). In this case the resistance of the structure for parallel magnetic moment configuration was found to be low, while the resistance for the antiparallel configuration was high.<sup>26</sup> The change of resistance was expected to be 100 % for ideal devices and hence this phenomenon was known as the GMR effect.

The GMR effect can be described using a simple parallel resistor model as shown in Fig. 1.2.<sup>27</sup> The electrons scatter when they pass through a layer with opposite moment configuration. The box shown in the figure represents the resistance that the majority and minority spin channel electrons will experience in each layer. The resistance values for the minority spin channel electrons are going to be higher compared to the resistance experienced by the majority spin channel electrons. As per the equation show in the figure, the total resistance in the parallel

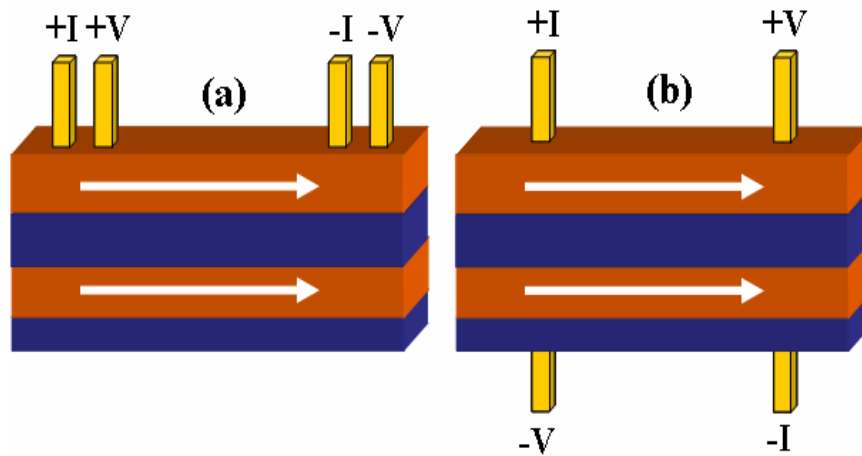


**Figure 1.3** GMR structure of (a) CIP and (b) CPP geometry.

configuration will be smaller than that in the antiparallel configuration.

GMR structure can work in two configurations called the current in plane (CIP)<sup>28</sup> and the current perpendicular to the plane (CPP)<sup>29</sup> configuration. In CIP configuration the current flow direction is in the plane and in CPP configuration the current flow is perpendicular to the layers as shown in Fig. 1.3. It is much more convenient to measure the resistivity in CIP geometry than

in CPP geometry, because in CPP geometry the resistance of the metallic film is extremely small. Further, no patterning is required for making contacts in the CIP geometry. However, the GMR effect is expected to be much larger in CPP geometry than in CIP geometry. Current perpendicular to the plane GMR is very attractive from an application point of view, but there are experimental difficulties in fabricating a CPP GMR structure. Even though both configurations show the change in resistance with different magnetic orientation, the physical explanation is different. In CIP configuration the spin up and spin down electrons have different mobility and the electrons experience momentum in the magnetic layers since the nonmagnetic interlayer is very thin. In case of parallel orientation, one spin type electron experiences scattering but the other does not, resulting in a low resistance referred to as high mobility. In case of antiparallel orientation, both spin type electrons experience scattering resulting in high resistance or low mobility.

The ferromagnetic electrodes can have either positive or negative spin polarization, which is determined by the relative density of states of the electrons at the Fermi energy. If the density of majority electrons is larger than that of the minority electrons at the Fermi energy, then the electrode will have positive spin polarization. On the other hand, if the density of the majority electrons is higher, then the spin polarization is negative. If the ferromagnetic electrodes used for a GMR structure have opposite polarization then an inverse GMR is usually observed.

Another important effect that is observed in magnetic multilayer nanostructures, with close similarity to GMR, is termed tunneling magnetoresistance (TMR).<sup>30</sup> TMR is based on spin tunnel junction and its principle is based on the fact that an electron passing through two conducting electrodes separated by a thin insulating layer experience quantum mechanical tunneling. The tunneling rate depends on the density of states of the metal electrodes, the barrier

height and the thickness of the insulating layer. A spin tunnel junction consists of two ferromagnetic electrodes separated by a very thin (of a few nanometers) electrically insulating layer. The magnetotransport characteristic of a magnetic tunnel junction (MTJ) is very similar to CPP GMR. When the relative magnetic orientation of the ferromagnetic electrodes is parallel, the junction shows low resistance and for antiparallel orientation, the resistance is high. Although spin tunnel junction is analogous to CPP GMR device, there are some advantages of spin tunnel junction over CPP GMR. One advantage is that the resistance of the tunnel junction is higher than CPP GMR structure of comparable size, and is non-Ohmic. In addition, the MR effect in tunnel junction is larger than that observed in a CPP GMR system.

Recently, GMR and MTJ structures have received unprecedented attention due to their wide range of applicability in the field of magnetoelectronics. Some of the important applications are magnetic field sensors, read heads for hard drive, galvanic isolator and magnetoresistive random access memory (MRAM) devices.<sup>31</sup> CIP GMR spin valve sensors are widely used in storage hard drive in which information is stored in tiny magnetized regions, with up and down orientations. The transitions between the magnetized regions are detected by the GMR sensor to encode the information. The size of each magnetic domain and separation between them determines the storage density of the hard drive. To keep pace with the increasing demand of higher bit density, the bit size needs to be as small as possible and simultaneously the size of the read sensor has to be of comparable size with the bit in a hard drive. It is possible to decrease the size of the read sensors using advanced technology to keep pace with the decreasing size of the magnetic bit. In a CIP GMR spin valve, the magnetization direction of one of the ferromagnetic electrode is held fixed by an adjacent anti-ferromagnetic layer. The other ferromagnetic electrode is free to respond to an externally applied magnetic field. In the absence of an external magnetic field the

magnetization of the ferromagnetic electrodes orients perpendicular to each other resulting in high resistance. When a magnetic field is applied, the magnetization direction of both the ferromagnetic layer becomes parallel to each other, leading to a small resistance. When a CIP GMR sensor is brought close to the magnetic bit, the magnetization direction of the free layer will be parallel or perpendicular to the pinned layer, depending on the magnetic orientation of the bit. Thus the magnetic orientation of the bit can be read as low or high resistance.

TMR read sensors have some advantages over CIP GMR sensors due to the larger magnetoresistive signal. The fact that in TMR read sensors the current flow perpendicular to the layers has made it possible to decrease the size of the TMR sensor. Bill Butler's prediction on Fe/MgO/Fe TMR structure using the concept of symmetry filter has made it possible to realize a very large signal from a very small TMR device.<sup>32</sup> Although TMR sensors show very high MR signals, it reaches a limit due to noise problems as the bit size continues to decrease. The read sensor size is going to be as small as 100 nm for bit densities of 100 Gbits per square inch and the total current becomes very small. Small TMR sensors lead to a random fluctuation in the current as the electron tunnels through the barrier randomly. To overcome this limitation, CPP GMR is expected to be a better choice for future read head sensors.

MTJ based structures are also used to design a new class of memory cell known as Magnetic Random Access Memory (MRAM). The development of MRAM is expected to add few features to the existing memory technologies, such as high performance, high density, low power, non volatility and high endurance.<sup>33</sup> The architecture of the MRAM is shown in Fig. 1.4. The bit information is stored in a parallel and an antiparallel magnetization direction of the two magnetic layers in a magnetic tunnel junction. The higher junction resistance for the antiparallel state of the magnetic layer is assigned "1" and the lower junction resistance for the parallel orientation is

assigned “0”. The magnetic tunnel junction lies between a word line and a bit line arranged at a right angle to each other. For reading a particular bit, a current is passed with an associated transistor from a supply line through the tunnel junction to the ground. By measuring the resulting current, the magnetic orientation of the magnetic layer is determined, which tells us about the present state of the bit. To write a bit, certain amount of current is passed through the word line in order to generate a magnetic field on the addressed memory cell. The current pulses are selected in such a way that only those cells which are at the cross point of the two lines are switched, all other cells remain unswitched. The disadvantage of this mode of switching is that it

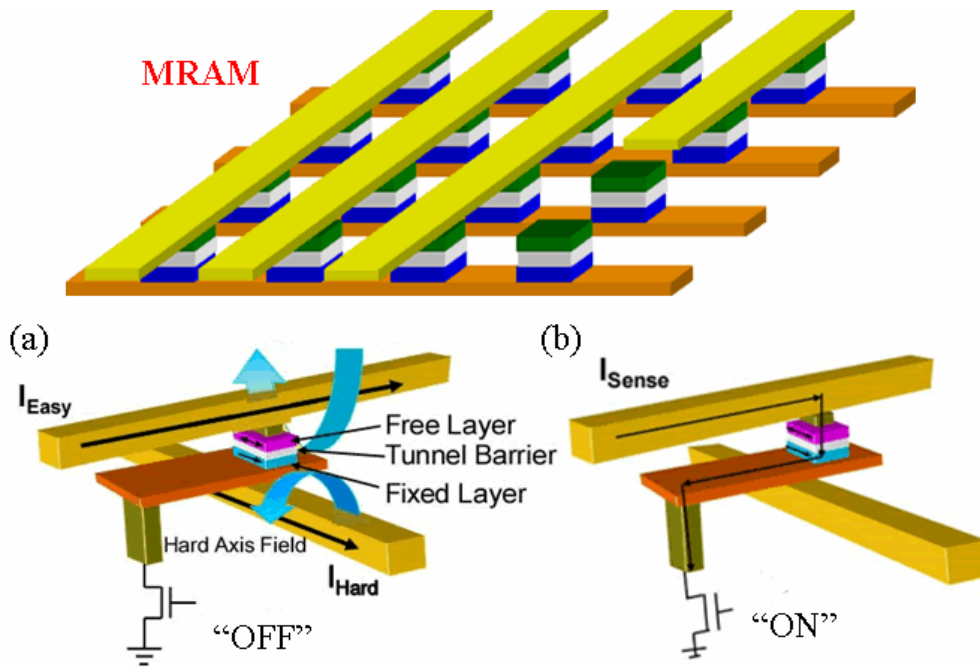


**Figure 1.4** Writing (a) and reading (b) process of MTJ MRAM memory array. Adapted from ref. [34].

requires substantial current to switch the magnetic layer and in addition, for smaller cell size, the induced field overlaps with the adjacent cell, sometimes causing a false write. To avoid this problem a different mode of switching is used known as spin polarized current induced switching. In this approach a spin polarized current is passed through a magnetic layer. The

imbalance in the spin due to spin polarized current generates a torque on the system, which eventually causes a complete reversal of the magnetization. Although there are many advantages of using current induced switching, one drawback is that it needs high current density to induce switching.

#### 1.4 Half-metals

Since the MR ratio is closely associated with spin polarization, finding a fully polarized room temperature ferromagnetic material will revolutionize the field of spintronics. Half-metallic ferromagnetic materials appear as potential candidates because they act as a metal for a majority spin channel and as an insulator for a minority spin channel with a gap in the spin polarized density of states (Fig. 1.5).<sup>35</sup> Half-metals are predicted to have 100 % spin polarization in theory.

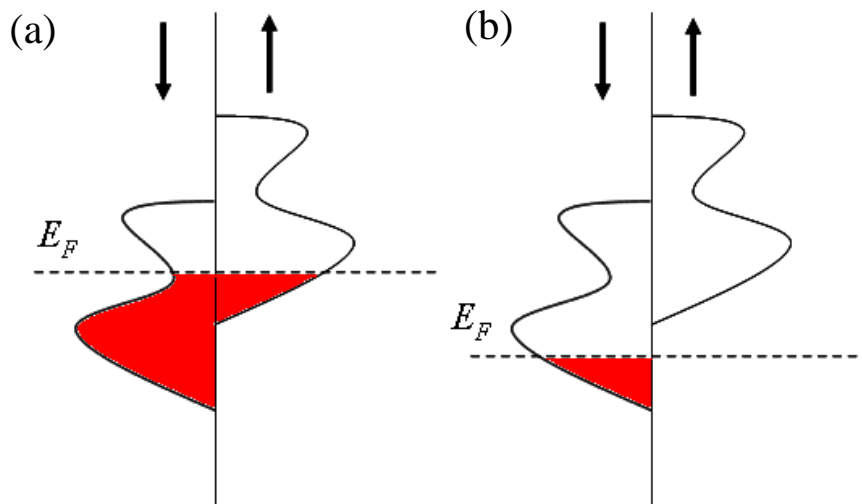


**Figure 1.5** Schematics of the difference in the density of states between a ferromagnet (a) and a half metallic ferromagnet (b).

According to the Julliere model<sup>30a</sup> the magnetoresistance in a TMR structure depends on the spin polarization of the electrode by the following relation:

$$TMR = \frac{2P_1P_2}{1 - P_1P_2} \quad (1.1)$$

where  $P_i = \frac{n^\uparrow - n^\downarrow}{n^\uparrow + n^\downarrow}$ ,  $n^\uparrow$  and  $n^\downarrow$  represent the density of state for up and down spin electron, respectively. The tunnel junctions fabricated with half metals ( $P=100\%$ ) as electrodes are expected to provide very high TMR. Therefore, half metals are considered to be ideal materials for TMR and GMR devices. Half metal ferromagnet can also be used as an ideal spin injector and detector in spin-logic devices, because they ideally conduct electrons in only one spin channels. In case of normal ferromagnets that are partially spin polarized, such as cobalt and nickel, the  $4s$  band crosses the Fermi level, which carries most of the current. For a normal metal the current is carried equally by spin up and spin down electrons. In order to obtain a gap at the minority spin channel, the  $3d$  and  $4s$  bands need to be reordered by hybridization. In hybridization the bottom of the  $4s$  band is pushed up above Fermi level or the Fermi level in  $d$  band is pushed below the bottom of the  $4s$  band. Therefore, it needs more than one element for the hybridization to occur. In other word, all half metals are either alloys or compounds. Thus far two main classes of half-metallic materials have been identified - Heusler alloys and oxides. Heusler alloys are considered to be very attractive as a half metal ferromagnet at room temperature due to their lattice matching with the traditional III-V semiconductors and high Curie temperature.<sup>36</sup> Heusler alloys are classified into two categories based on their crystalline structure, half Heusler alloy XYZ with  $C1_b$  structure and  $X_2YZ$  with  $L2_1$  structure, where X and Y represents the transition metal atoms and Z is either a semiconductor or a nonmagnetic metal. NMnSb and PtMnSb belongs to the half-Heusler alloys and  $Co_2MnSi$  and  $Co_2(Cr,Fe)Al$  belongs to the full-Heusler alloys.

Typical examples of oxide half metals are  $Fe_3O_4$ ,  $La_{0.7}Sr_{0.3}MnO_3$ ,  $CrO_2$ ,  $Tl_2Mn_2O_7$  and

$\text{Sr}_2\text{FeMoO}_6$ .<sup>37</sup> Transition metal oxides have a large degree of freedom, which can be exploited to tune the physical properties according to the required function. Recently the need for multifunctional materials has been realized in spintronics. The freedom of tuning the properties of transition metal oxide like ferromagnetism, ferroelectricity, superconductivity, antiferromagnetism, optical properties, *etc.* make them potential candidates for spintronics.  $\text{Fe}_3\text{O}_4$  is theoretically predicted to be a half metal and has a very high Curie temperature (860 K).  $\text{Fe}_3\text{O}_4$  has a spinel structure, where *A* sites are occupied by  $\text{Fe}^{3+}$  ions and *B* sites are occupied by  $\text{Fe}^{2+}$  and  $\text{Fe}^{3+}$  ions. The ferrimagnetic ordering arises from the strong antiferromagnetic coupling between the *A* and *B* sublattices. Within the *B* sublattice, the Fe ions are coupled ferromagnetically.  $\text{Fe}_3\text{O}_4$  undergo a metal-insulator phase transition below 120K.  $\text{La}_{0.7}\text{Sr}_{0.3}\text{MnO}_3$  has a rhombohedrally distorted perovskite structure. In this system, hopping of electrons results in ferromagnetism by double exchange interaction. Although LSMO has a low Curie temperature around 360-380 K, there has been a lot of interest in LSMO for spintronics application recently.<sup>38</sup>  $\text{Sr}_2\text{FeMoO}_6$  has a double perovskites structure. It crystallizes in a tetragonal structure with NaCl type order of Fe and Mo. This is a ferromagnetic compound with a Curie temperature ( $T_C$ ) around 420 K and a saturation magnetic moment of  $4\mu_B$ . Our recent band structure calculations indicate the exciting possibility of inducing half-metallicity in some of the mixed chalcospinels, as described in Section 4 of this thesis.

## 1.5 References

- (a) G. Schmid, *Cluster and Colloids: From Theory to Applications*, VCH, New York, 1994.  
(b) C. N. R. Rao, *J. Mater. Chem.* **1**, 1-14 (1999).
- (a) C. Xu, S. Sun, *Dalton Trans.*, 5583 (2009). (b) N. A. Frey, S. Peng, K. Cheng, S. Sun, *Chem. Soc. Rev.* **38**, 2532 (2009). (c) R. Hao, R. Xing, Z. Xu, Y. Hou, S. Gao, S. Sun, *Adv. Mater.* **22**, 2729 (2010).

3. R. Eden, *The Decades of the New World or West India*, p. 264, 1555 (reprinted 1885).
4. J. Scoffern, *Orr's Circle of Science, A Series of Treatises on the Principles of Science*; p. 448. 1854.
5. R. Hughes, K. E. Sickafus, *J. Am. Ceram. Soc.* **82**, 3277 (1999).
6. A. R. West, *Basic Solid State Chemistry*, John Wiley & Sons: New York, 1988; R. C. O'Handley, *Modern Magnetic Materials-Principles and Applications*, John Wiley & Sons: New York, 2000.
7. J.-Y. Luo, Y.G. Wang, H.-M. Xiong, Y.-Y. Xia, *Chem. Mater.* **19**, 4791 (2007).
8. A. F. Wells, *Structural Inorganic Chemistry* (Oxford University Press, Oxford, 1986).
9. <http://www.phy.bris.ac.uk/groups/theory/index.html>
10. K. G. Nikiforov, *Prog. Cryst. Growth and Charact. Mat.* **39**, 1 (1999); Landolt-Börnstein, *Magnetic and other properties of oxides and related compounds* (New Series, ed. K.-H. Hellwege Vol.III/4b, Springer, 1970).
11. *Semiconductor Spintronics and Quantum Computation*, edited by D. D. Awschalom, D. Loss and N. Samarth (Springer, Berlin, 2002).
12. A. P. Ramirez, R. J. Cava, J. Krajewski, *Nature*, **386**, 156 (1997).
13. J. Hemberger, P. Lunkenheimer, R. Fichtl, H.-A. Krug von Nidda, V. Tsurkan, A. Loidl, *Nature*, **434**, 364 (2005).
14. A. P. Alivisatos, *Science*, **271**, 225 (1996).
15. P. K. Jain, X. Huang, I. H. El-Sayed, M. A. El-Sayed, *Plasmonics*, **2**, 107 (2007).
16. S. Sun, H. Zeng, D. B. Robinson, S. Raoux, P. M. Rice, S. X. Wang, G. Li, *J. Am. Ceram. Soc.*, **126**, 273 (2003).
17. Y. Yin, A. P. Alivisatos, *Science*, **437**, 664 (2005); O. Masals, R. Seshadri, *Ann. Rev. Mater. Res.*, **34**, 41 (2004).
18. A.-H. Lu, E. L. Salabas, F. Schüth, *Angew. Chem. Int. Ed.*, **46**, 1222 (2007).
19. J. Zhang, Z.-L. Wang, J. Liu, S. Chen, G.-Y. Liu, *Self-assembled nanostructures*, Kluwer Academic, Boston (2003); T. Hyeon, *Chem. Comm.* **8**, 927 (2003).
20. S. Mann, *Biomineralization: principles and concepts in bioinorganic materials chemistry* (Oxford University Press, 2001).

21. S. Mornet, S. Vasseur, F. Grasset, E. Duguet, *J. Mat. Chem.*, **14**, 2161 (2004); I. Šafařík and M. Šafaříková, *Monatshefte für Chemie*, **133**, 737 (2002).
22. D. A. La Van, T. McGuire, R. Langer, *Nature Biotech.*, **21**, 1184 (2003) ; M. Han, X. Guo, J. Z. Su, S. Nie, *Nature Biotech.*, **19**, 631 (2001).
23. M. N. Baibich, J. M. Broto, A. Fert, F. Nguyen van Dau, F. Petroff, P. Eitne, G. Creuzet, A. Friederich, J. Chazelas, *Phys. Rev. Lett.* **61**, 2472 (1988).
24. P. Grünberg, R. Schreiber, Y. Pang, M. B. Brodsky, H. Sowers, *Phys. Rev. Lett.* **57**, 2442 (1986).
25. N. Mott, *Proc. Roy. Soc.* **156**, 368 (1936).
26. M. N. Baibich and A. Fert, *Phys Rev. Lett.* **61**, 2472 (1988).
27. T. Valet and A. Fert, *Phys. Rev. B* **48**, 7099, (1993); Albert Fert, *Rev. Mod. Phys.* **80**, 1517 (2008).
28. (a) A. Barthelemy, A. Fert, *Phys. Rev. B* **43**, 13124 (1991). (b) A. Vedyayev, B. Dieny, N. Ryzhanova, *Europhys. Lett.* **19**, 329 (1992). (c) J. Barnas, Y. Bruynseraede, *Phys. Rev. B* **53**, 5449 (1996).
29. P. Levy, *Solid State Phys* **47**, 367 (1994).
30. (a) M. Julliere, *Phys. Lett.* **54A**, 225 (1975). (b) T. Miyazaki, N. Tezuka, *J. Magn. Magn. Mater.* **139**, L231 (1995). (c) J. S. Moodera, L. R. Kinder, T. M. Wong, R. Meservey, *Phys. Rev. Lett.* **74**, 3273 (1995).
31. S. A. Wolf, D. D. Awschalom, R. A. Buhrman, J. M. Daughton, S. Von Molnar, M. L. Roukes, A. Y. Chtchelkanova, D. M. Treger, *Science* **294**, 1488 (2001).
32. W. H. Butler, X.-G. Zhang, T. C. Schulthess, and J. M. MacLaren, *Phys. Rev. B* **63**, 054416 (2001).
33. S. Tehrani, J. M. Slaughter, E. Chen, M. Durlam, J. Shi, M. DeHerrera, *IEEE Trans. Magn.* **35**, 2814 (1999).
34. <http://thefutureofthings.com/articles/36/mram-the-birth-of-the-super-memory.html>
35. R. A. de Groot, F. M. Mueller, P. G. van Engen, and K. H. J. Buschow, *Phys. Rev. Lett.* **50**, 2024 (1983).
36. G. Engels, J. Lange, Th. Schapers, and H. Luth, 1997, *Phys. Rev. B* **55**, R1958 (1997).

37. H. Y. Hwang, S. W. Cheong, *Science* **278**, 1607 (1997); J. H. Park, E. Vescovo, H. J. Kim, C. Kwon, R. Ramesh, T. Venkatesan, *Nature* **392**, 794 (1998); Z. Zhang, S. Satpathy, *Phys. Rev. B* **44**, 13319 (1991).
38. M. Bowen, M. Bibes, A. Barthélémy, J.-P. Contour, A. Anane, Y. Lemaître, and A. Fert, *Appl. Phys. Lett.* **82**, 233 (2003).

## CHAPTER 2

### EXPERIMENTAL TECHNIQUES

The principal experimental techniques used for synthesizing and characterizing the oxide and chalcogenide spinel materials are introduced in this chapter. The first section covers the solution-based method for nanocrystal synthesis and chemical vapor deposition (CVD) / direct liquid injection CVD (DLICVD) technique for thin film deposition. Subsequently, characterization techniques including structure (XRD, TEM), surface (AFM, SEM) and magnetic (AGM, VSM, SQUID) are discussed.

#### 2.1 Wet Chemical Synthesis Setup

A schematic of the apparatus used for nanocrystal synthesis is shown in Fig. 2.1. A 50 ml

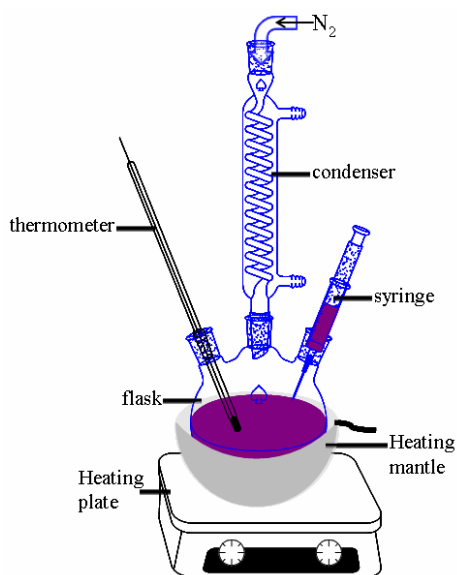


*Figure 2.1* Schematic diagram of nanocrystal synthesis.

four-neck flask is connected with a water-cooled condenser. A thermometer is inserted through one of the port for temperature measurement, while the other port is used for injection of the

precursor into the solution using a syringe. The reaction temperature is controlled manually using a heating mantle with power controller. An inert gas - nitrogen or argon - is continuously flushed through the flask during the reaction process.

In a typical synthesis, the metal-organic precursors are dissolved in oleylamine (OLA) or 1-octadecene (ODE) and the solution is injected into a solution containing the anion source at the reaction temperature, or at room temperature and then heated up. The detail reaction conditions are described in Chapter 3.

## 2.2 Chemical Vapor Deposition Technique

Chemical vapor deposition (CVD) is a chemical process for the growth of films using suitable precursor(s). The CVD process essentially relies on the decomposition of one or more

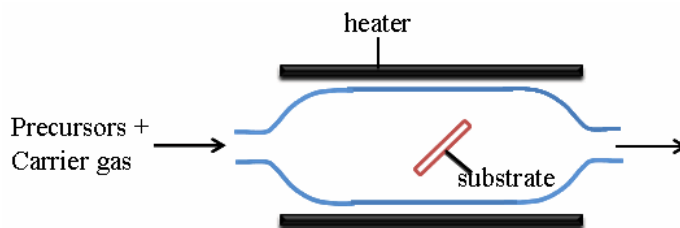


**Figure 2.2** Schematic diagram of a general CVD system.

volatile precursors, transported to a reaction zone in a vapor phase, where they subsequently decompose on a heated substrate resulting in solid film deposition. (Fig. 2.2), The use of gaseous reactants, often generated from a (gas) liquid or solid precursor material in a pre-reactor, gives CVD a number of advantages over other deposition methods, chief among them the high degree of conformal coverage and reactive nature of deposition. CVD allows the synthesis of high-quality films of materials that are otherwise problematic, such as chalcogenides, borides and nitrides. Further, CVD allows one to take advantage of selective growth, one of its greatest advantages. Various forms of deposited thin film including single crystalline, polycrystalline and

amorphous films can be deposited using the CVD process. As with any deposition method, CVD

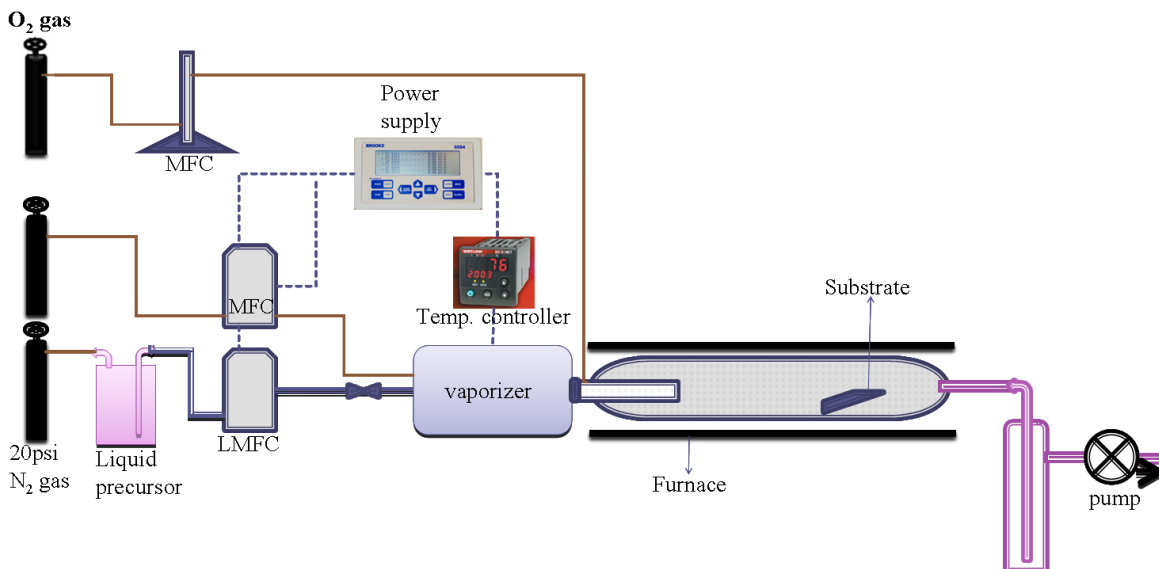


**Figure 2.3** Schematic diagram of a direct liquid injection CVD system.

has its limitations. In practice, the availability of suitable precursors is a limitation. The CVD of complex, multi-component materials is beset by probability of contamination, film heterogeneity, and the synchronized delivery of multiple precursors.

For precursors having low volatility a direct liquid injection process is better suited for delivery of the precursors after vaporization into the reactor. For direct liquid injection chemical vapor deposition (DLI-CVD), the precursors are dissolved in a suitable organic solvent and directly injected into the deposition furnaces so the problems associated with vapor pressure and decomposition during delivery can be essentially eliminated (Fig. 2.3). The precursor solution is vaporized in the vaporizer so the precursor (s) entrained in the vaporized solvent is transported to the heated substrate placed in the oven by a carrier gas, argon, as in a typical CVD process. A separate flow of oxygen is used as an oxidant during the deposition process. The adjustable parameters are precursor concentration, precursor flow rate, vaporizer temperature, carrier gas flow rate, oxygen flow rate, reaction chamber pressure, and substrate temperature. The detail condition parameters for deposition will be described in Chapter 5. DLI-CVD is a particularly

useful method for multi-component system as several precursors can be dissolved in the same solution and the relative delivery rates of precursors are determined by the composition.

### 2.3 X-ray Diffraction/ X-ray Reflectivity

X-ray diffraction is an analytical technique that provides information about the crystallographic structure, chemical composition, and physical properties of materials and thin films. X-rays are electromagnetic radiation with photon energy ranging from 120 eV to 120 keV. X-rays can be used to probe the structural order of atoms and molecules because their wavelength is comparable with the size of an atom.

X-rays are generated from a high energy focused electron beam bombarding a metal target. The electron beam is accelerated by applying a high voltage on cathode of the x-ray source.

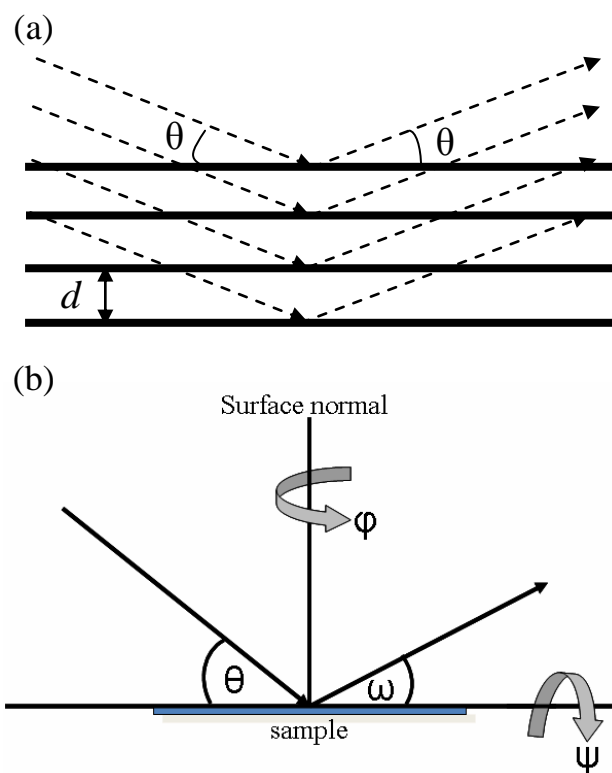


**Figure 2.4** (a) schematic drawing of Bragg's law; (b) schematic view of the different angles involved in a XRD measurement.

When electrons collide with the target, they are de-accelerated a continuous spectrum of energy is emitted known as Bremsstrahlung radiation. X-rays can also eject inner shell electrons from the atom of the target material through an ionization process. The ion of the target material leaves a vacancy in the deep K shell. When an electron from the outer shell falls into the K shell, it emits the excess energy as x-ray photon which is characteristic of the target material. The transition of electrons from L to K shell causes the most intense radiation known as  $K\alpha$  line. When x-rays interact with electrons in an atom, a portion of the incident beam will be deflected away from their original pathway. If the wavelength of the scattered beam remains constant, then the process is called elastic scattering. If the scattered beam has a different wavelength from the incident beam, then the process is called inelastic scattering. The diffracted wave from a periodic arrangement of atoms forms a sharp interference of maxima (peaks) with the same symmetry as the distribution of atoms. The peaks in the X-ray diffraction pattern are related to the atomic distances by the Bragg's law (Fig. 2.4a.):

$$n\lambda = 2d \sin \theta, \quad (2.1)$$

where  $d$  is the lattice plane spacing,  $\theta$  is the position of peak,  $n$  is the order of diffraction and  $\lambda$  is the wavelength of X-rays. The width of peaks also provides information about the grain size. The mean grain size can be estimated by the Debye-Scherrer equation:

$$\tau = \frac{K\lambda}{\beta \cos \theta}, \quad (2.2)$$

where  $K$  is the shape factor,  $\lambda$  is the x-ray source wavelength,  $\beta$  is the line broad at the full width at half maximum (FWHM), and  $\theta$  is the Bragg angle.

The rocking curve, which is obtained from the  $\omega$  scan around a peak (Fig. 2.4b), provides valuable information about the orientation spread of the film. The ideal FWHM of rocking curve should be around  $0.02^\circ$  for a single crystalline sample. For the films, rocking curve indicates the

crystalline quality of the film. The smaller the FWHM of rocking curve, the better the quality of films.

The other powerful tool using x-ray is the x-ray reflectivity (XRR). XRR is carried out by the  $\theta$  scan at low angles, in the range from  $0.5^\circ$  to  $7^\circ$ . Kiessig fringes are observed for thin films that have very smooth interface and surface. The period of the oscillation corresponds to the film thickness. The difference of the path length of the beam reflected at the surface of the film and the beam reflected at the film/substrate interface can be calculated:

$$\Delta l = 2d_t \sqrt{k^2 - \cos^2 \theta_i} , \quad (2.3)$$

where  $d_t$  is the thickness of the film,  $k$  is the optical constant of the film, and  $\theta_i$  is the angle of the incident beam. The optical constant of the film is given by the relation

$$k = 1 - \delta - i\beta_a , \quad (2.4)$$

where  $\delta$  denotes the refraction of x-ray and  $\beta_a$  is the absorption of x-ray. A maximum in the reflectivity curve corresponds to a constructive interference, thus

$$\Delta l = n\lambda , \quad (2.5)$$

where  $n$  is the order of diffraction of the fringe appearing. After inserting eq. 2.5 and 2.4 into eq. 2.3, the following relation between  $d_t$  and  $\theta_i$  can be obtained:

$$\sin^2 \theta_i = \frac{\lambda^2}{4d_t^2} n^2 + 2\delta . \quad (2.6)$$

The slope of the  $\sin^2 \theta_i$  versus  $n^2$  linear fit is proportional to thickness  $d_t$ .

Taking into account the optical density of the material of film, the surface and interface roughness can be calculated from the decay of the intensity. The measureable thickness is limited between tens to a few hundred nanometers; otherwise the fringes are too wide or too narrow to be analyzed properly.

## 2.4 Atomic Force Microscopy

Atomic force microscopy (AFM) is a technique to image the surface topography from atomic scale to sub-micron scale. The AFM consists of cantilever with a sharp tip at its end. When the tip is on the top of sample surface, force between the tip and the sample results in a deflection of the cantilever according to Hooke's law. AFM measures a variety of forces including mechanical contact force, van der Waals force, chemical bonding, electrostatic force, magnetic force, etc. The magnetic force mode is useful for magnetic samples, which can visualize the magnetic domain of the sample. Typically, the deflection is measured using a laser spot reflected from the top surface of the cantilever into an array photodiodes (Fig. 2.5.). While the tip scans the surface of the sample, the tip height variation is recorded to produce a topographic image of the surface.

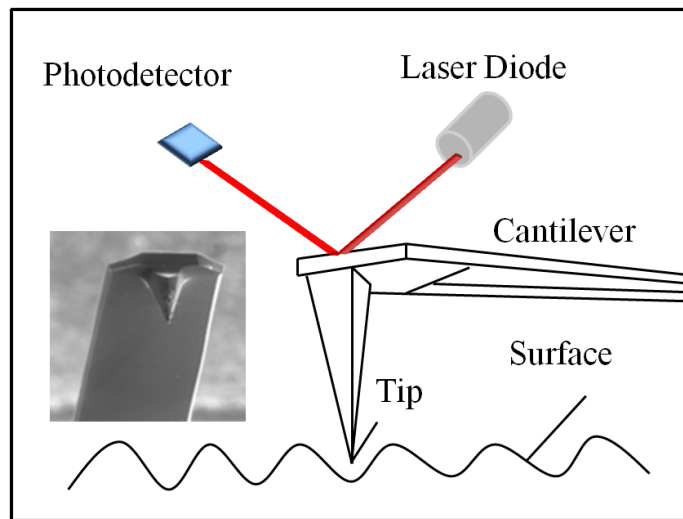


**Figure 2.5** Schematic diagram of AFM and inset is an image of AFM tip. Adapted from ref. [1]

## 2.5 Vibrating Sample Magnetometer

A vibrating sample magnetometer (VSM) is a technique for measuring the magnetic properties of the materials. The VSM measurement is based on the Faraday's law of induction. When a sample is placed inside a uniform magnetic field, its magnetism induces a dipole

moment. The induced dipole moment creates a magnetic field around the sample. While the sample is vibrating, the magnetic field around the sample is changed and the change in magnetic field can be sensed by a pickup coil as an induced electrical signal (Fig. 2.6.). This signal is amplified by a lock-in amplifier. A lock-in amplifier is used to eliminate the noise from environment and only pick up signal from the sample at the vibrating frequency. The amplitude of the induced current is proportional to the magnetization of the sample. Therefore, the hysteresis loop of a material is obtained.

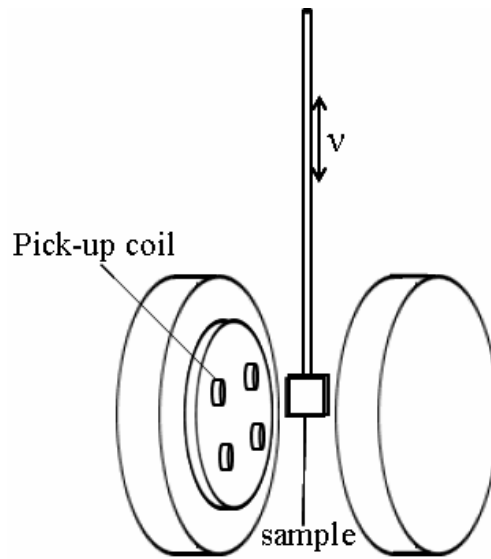


**Figure 2.6** Schematic diagram of VSM system.

## 2.6 Alternating Gradient Magnetometer

Alternating gradient magnetometer (AGM) is also used for magnetic property measurements, and it is more sensitive than VSM. A gradient coil is installed in the AGM instead of pick-up coil in VSM. An oscillating current is applied to the gradient coil to produce a non-uniform alternating current field. This gradient field exerts oscillating force sensed by a transducer on sample which is proportional to magnetic moment of the sample. It takes only a few minutes to

complete a hysteresis loop in AGM measurement. Some disadvantages of the AGM magnetic measurements include the limited sample size (5mm x 3mm) and the magnetization reversal can occur in soft materials.

## 2.7 Superconducting Quantum Interference Device

Superconducting quantum interference device (SQUID) is one of the most sensitive detectors of magnetic flux. The SQUID is a magnetic flux-to-voltage transducer with the Josephson junction (Fig. 2.7.)<sup>2</sup> as the heart of this equipment. A Josephson junction device consists of a superconducting coil which is broken by one (RF SQUID) or two (DC SQUID) thin insulating

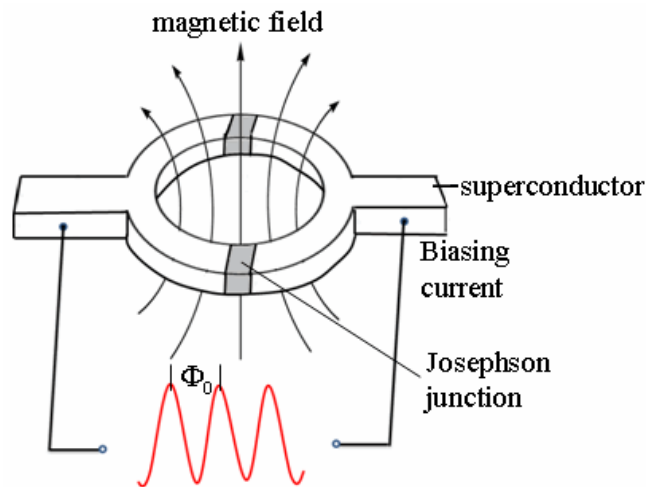


**Figure 2.7** Schematic diagram of SQUID with Josephson junction.

layers which can experience electron tunneling through the junction. These insulating layers restrict the value of supercurrent flowing in the coil to less than  $10^{-5}$  A. SQUID detection system is a detection gradiometer coils. They can balance and arrange accurately in detecting the magnetic flux induced by the magnetization of the samples. As the sample moves through the coils, the magnetic moment of the sample induces an electric current in the detecting coil. This critical current is not damped so any tiny change in magnetic flux can be detected by the

detection coils. The critical current is usually obtained by measuring the voltage drop across the junction as a function of the total current through the device.

## 2.8 Scanning Electron Microscopy

Scanning electron microscopy (SEM) is a type of microscope to image the sample surface by scanning it with high energy electron beam. A stream of electrons are formed by a cathode filament and accelerated towards the sample by applying a positive voltage. The types of signals produced by SEM include secondary electrons, backscattered electrons and characteristics X-ray. The signals result from interaction of the electron beam with atoms or near the surface of the sample. Secondary electron imaging is the most common detector and can produce very high-resolution of about 1 to 5 nanometer in size. Back-scattered electrons (BSE) are electrons that are reflected by the sample due to elastic scattering. Because the intensity of BSE signal is strongly related to the atomic number ( $Z$ ), BSE images can provide information about the distribution of different element in the sample. Characteristic X-rays are emitted when the electron beam removes an inner shell electron from the sample, causing a higher energy electron to fill the outer shell and release energy. These characteristic X-rays are used to identify the composition and measure the quantities of elements in the sample.

## 2.9 Transmission Electron Microscopy

Transmission electron microscopy (TEM) works exactly the same as its optical counterpart except that a focused beam of electrons is used instead of light to image the specimen and determine its structure and composition (Fig. 2.8.). A stream of electrons is formed by an electron source and accelerated toward the ultra thin specimen using a positive electric potential.

This stream is confined by metal apertures and magnetic lenses into a focused, monochromatic beam. These monochromatic electrons are focused onto the sample using a magnetic lens. Interactions occurring inside the irradiated sample are affecting the electron beam and these interactions and effects detected and transformed into an image.

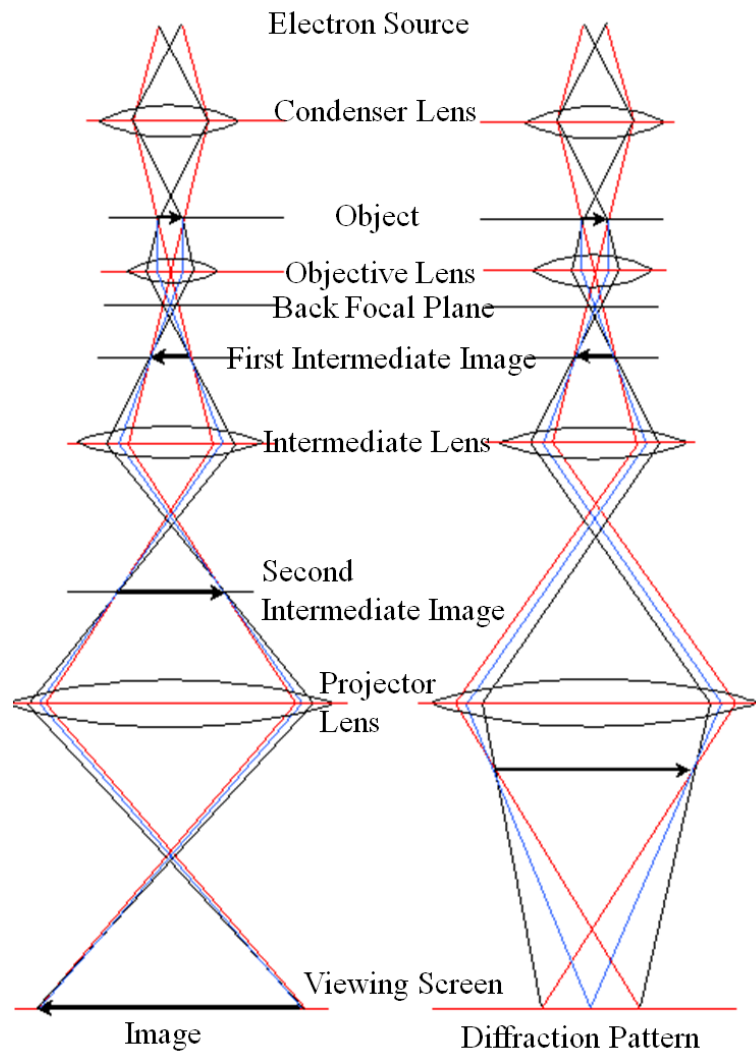


**Figure 2.8** Basic transmission electron microscopy component layout. Adapted from ref. [3].

The resolution of microscopy can be estimated from:

$$d_{res} = \frac{\lambda_s}{2n \sin \alpha}, \quad (2.7)$$

where  $\lambda_s$  is the wavelength of source,  $n$  is the refraction index of the medium, and  $\alpha$  is the half-angle of the cone of beam entering the lens. In optical microscope, the limit in resolution is due to the large wavelength of the photons compare to that of the electron. The wavelength ( $\lambda_e$ ) of electrons used in TEM imaging is formulated by applying de Broglie equation to the kinetic energy of an electron. An additional correction must be made to account for relativistic effect as an electron's velocity approaches the speed of light.<sup>3</sup>

$$\lambda_e = \frac{h}{\sqrt{2m_0E\left(1 + \frac{E}{2m_0C^2}\right)}}, \quad (2.8)$$

where  $h$  is Planck's constant,  $m_0$  is the mass of an electron, and  $E$  is the energy of the accelerated electron.

## 2.10 Vienna *ab initio* Simulation Package (VASP)

VASP is a simulation package for quantum mechanical molecular dynamics simulations based on density function theory (DFT). In this dissertation, the basis sets are generalized gradient approximation (GGA) for exchange-correlation potential and the projector-augmented wave method.

### 2.10.1 Density Function Theory

Predecessors of the DFT are the Thomas-Fermi model and the Hartree-Fock-Slater method. The Thomas-Fermi model is a statistical model developed by Thomas<sup>4</sup> and Fermi<sup>5</sup> in 1927 postulating that interacting electrons moving in an external potential are distributed uniformly in phase space. They developed an expression for the relation between the external potential and the density distribution of the electrons. Even though their model works well for systems with

slowly changing densities, their model is limited by the fact that all exchange and correlations effects are completely neglected. In 1928, Dirac<sup>6</sup> enhanced the Thomas-Fermi model by incorporating the exchange interaction.

The Hartree-Fock-Slater method is another *ab initio* method which goes back to the ideas by Hartree<sup>7</sup> in 1928 and Fock<sup>8</sup> in 1930, in which the many-electron wave function is approximated by an anti-symmetric product of one electron wavefunctions and the spin orbitals (Slater determinant). Using the variational principle it is possible to derive a set of N coupled equations for the N spin orbitals. Since in each effective one electron equation the orbitals of the other electrons are incorporated in an averaged density, this set of equations has to be solved iteratively. This procedure is repeated until a self consistent solution is found. An exact solution can only be found in the simple case of a hydrogen-like one-electron atom where the Hamilton operator is represented by:

$$H = -\frac{\hbar^2}{2m} \sum_{i=1}^N \nabla_i^2 - \sum_{i=1}^N \frac{Ze^2}{r_i} + \sum_{i<j} \frac{e^2}{|r_i - r_j|} \quad (2.9)$$

Slater<sup>9</sup> enhanced and simplified the Hartree-Fock by adding exchange potential to the model in 1951, but still the one-electron wave function remains a problem and in all systems other than hydrogen-like atoms requires an enormous computational effort.

The new approach is the realization that it is possible to calculate all physical quantities of interest with the knowledge of the ground state density of the many electron system. Instead of the knowledge of the many body wave function of the system, knowledge of the ground state density becomes crucial. The basis of DFT is theorems by Hohenberg and Kohn<sup>10</sup> in 1964. The first theorem states that the ground state of an N-electron system has a unique space-dependent electron density  $n(r)$  or there exists a one to one mapping between the ground state density and

the external potential. Historically this was first only proven for a non-degenerate ground state. Later in 1990, R. M. Dreizler<sup>11</sup> extended the theorem to include degenerate ground states. Since  $n(r)$  determines the total number of electrons and the full many electron system Hamilton operator (H), it implicates all properties determined by H. Therefore all those quantities are expressed as functionals of the ground state density, for example, the ground state energy can be expressed as  $E[n(r)]$ . The second Hohenberg-Kohn theorem states that this ground state energy can be obtained via a variational method: the exact ground state density minimizes the total energy functional.

Unfortunately, Hohenberg and Kohn theorems do not provide any applicable calculation method. The practical theorem was introduced by Kohn and Sham<sup>12</sup> in 1965. After the introduction of Kohn-Sham theorem, DFT became a practical method for calculating characteristic properties in solid state and molecular physics and has been widely used ever since. To determine the electron density Kohn and Sham had introduced system of N non-interacting one electron wave functions ( $\psi_i$ ). There are the N solutions of the Schrödinger equation in an effective potential  $V_{eff}(r)$ . These one electron Schrödinger equations are called Kohn-Sham equations and can be written down as:

$$\left[ -\frac{\hbar^2}{2m} \nabla^2 + V_{eff}(r) \right] \psi_i(r) = E_i \psi_i(r). \quad (2.10)$$

The Kohn-Sham effective potential  $V_{eff}$  is here defined by

$$V_{eff}(r) = V(r) + \int \frac{n(r')}{|r-r'|} r' + V_{xc}(r), \quad (2.11)$$

where the first term  $V(r)$  is the external potential which describes the interaction between the electrons and the nuclei. The second term accounts for the electrostatic interaction between the

electrons themselves and  $V_{xc}(r)$  is an exchange-correlation potential, given by  $V_{xc}(r) = \frac{\delta E_{xc}}{\delta n(r)}$

with the exchange correlation energy and the electron density given by  $n(r) = \sum_{f=1}^N |\psi_f(r)|^2$ .

The Kohn-Sham equations must be solved self consistently. In each calculation cycle, the exchange correlation potential is calculated with an appropriate approximation for the exchange correlation energy. With the exact knowledge of this energy the Kohn Sham equations are exact. The determination and approximation of the exchange correlation potential is therefore an essential problem in the solution of the Kohn Sham equations. In brief, it can be said that DFT maps the many body problem on an effective single particle Schrödinger equation by introducing an exchange correlation functional.

### 2.10.2 Generalized Gradient Approximation

The exchange correlation function can also be written as a sum of an exchange functional and a correlation functional. Different sets of exchange-correlation functional can be used based on time or accuracy considerations. The generalized gradient approximation<sup>13</sup> (GGA) is an attempt to include the non-homogeneity of the true electron density into account. Therefore, the energy functional includes both the electron density and the density gradient which can be written as:

$$E_{xc}^{GGA}[n_{\uparrow}, n_{\downarrow}] = \int d^3r f(n_{\uparrow}(r), n_{\downarrow}(r), \nabla n_{\uparrow}, \nabla n_{\downarrow}) \quad (2.12)$$

This approximation gives, for example, very good results for ground state energies. It can reduce local spin density approximation (LSDA) atomization energy errors by about a factor of 5. There exists many other approximations depending on the considered physical problem, such as the Lee-Yang-Parr<sup>14</sup> functional, the Gill<sup>15</sup> functional or Hybrid methods and the GGA approximation

is the most commonly used. In the Hybrid method, only one part of the exchange correlation potential is evaluated within GGA while the other part is calculated as the exchange energy of the Kohn-Sham equation. This method is computational much more time consuming but gives very good results in molecular physics.

### 2.10.3 Calculation Parameters for VASP

VASP uses a relatively large number of input and output files. The primary input files are INCAR, KPOINTS, POSCAR and POTCAR. The function of these four files and input parameters for the calculations are described. We used the VASP 4.6 version and performed calculations using the MINT Center clusters and one at the Alabama supercomputer center.

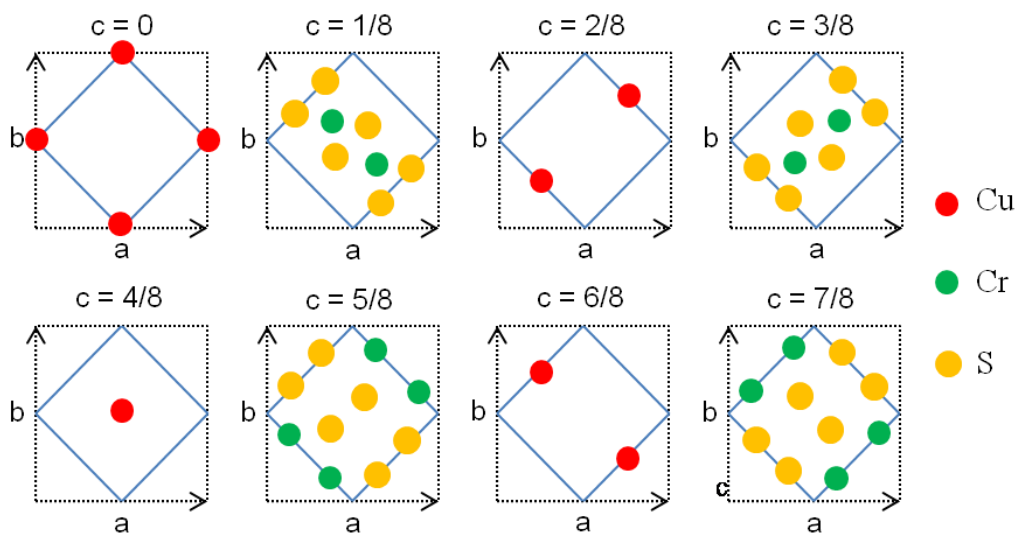


**Figure 2.9** Schematic drawing of eight layers in 28 atom supercell spinel structure.

#### 2.10.3.1 INCAR File

INCAR is the central input file of VASP. It contains a relatively a large number of parameters even though most of these parameters have convenient default values. The user is not necessarily



### 2.10.3.3 POSCAR File

POSCAR file describes the lattice geometry and the ionic positions. The first line is a comment line and the second line provides the universal lattice constant, which is used to scale all lattice vectors and all atomic coordinates. The following three lines provide the lattice vectors defining the unit cell of the given system. The sixth line supplies the number of atoms per each species, which must be consistent with INCAR and POTCAR files. Finally, the coordinate of all atoms are supplied from this line onward. The example of POSCAR is as follows.

```
Comment (name)
9.814
0.7071 0.0000 0.0000
0.0000 0.7071 0.0000
0.0000 0.0000 1.0000
4 8 16
direct
0.000 0.000 0.000 Cu
0.500 0.000 0.250 Cu
0.500 0.500 0.500 Cu
0.000 0.500 0.750 Cu
0.250 0.500 0.125 Cr
0.750 0.500 0.125 Cr
0.000 0.250 0.375 Cr
0.000 0.750 0.375 Cr
0.250 0.000 0.625 Cr
0.750 0.000 0.625 Cr
0.500 0.250 0.875 Cr
0.500 0.750 0.875 Cr
0.000 0.250 0.125 S
0.000 0.750 0.125 S
0.500 0.250 0.125 S
0.500 0.750 0.125 S
0.250 0.000 0.375 S
0.750 0.000 0.375 S
0.250 0.500 0.375 S
0.750 0.500 0.375 S
0.000 0.250 0.625 S
0.000 0.750 0.625 S
0.500 0.250 0.625 S
```

0.500 0.750 0.625 S  
0.250 0.000 0.875 S  
0.750 0.000 0.875 S  
0.250 0.500 0.875 S  
0.750 0.500 0.875 S

#### 2.10.3.4 POTCAR File

The POTCAR file contains the information of atom mass, valence electrons, the energy of the reference configuration for which the pseudopotential and so on for each atomic species used in the calculations. In addition, this file contains the default energy cutoff (ENMAX and ENMIN) so it is no longer necessary to specify these values in the INCAR file. The POTCAR file is generated from the database.

In summary, besides the theoretical methods summarized above this chapter has introduced synthesis methods for nanocrystals and direct liquid injection chemical vapor deposition (DLI-CVD) for thin film growth. Additionally, common characterization techniques of structure, surface and magnetic properties of materials are described. All of these techniques have enabled us to characterize the properties of nanocrystals and thin films, which will be discussed in the following chapters.

#### 2.11 References

1. <http://mrsec.wisc.edu/Edetc/nanoquest/afm/index.html>
2. B. D. Josephson, *Rev. Mod. Phys.* **46**, 251 (1974).
3. (a) P. E. Champness, *Electron Diffraction in the Transmission Electron Microscope*, (2001).  
(b) <http://www.mete.metu.edu.tr/pages/tem/TEMtext/TEMtext.html>
4. L.H. Thomas, *Proc. Cambridge Phil. Soc.*, **23**, 542 (1927).
5. E. Fermi, *Rend. Accad. Naz. Lincei*, **6**, 602 (1927).

6. P. A. M. Dirac, Proc. Roy. Soc., A117 (1928).
7. D. R. Hartree, Proc. Camb. Phil. Soc. **24**, 111 (1928).
8. V. Fock, Z. Phys. **61**, 126 (1930).
9. J. C. Slater, Phys. Rev. **81**, 385 (1951).
10. P. Hohenberg, W. Kohn, Phys. Rev. B **136**, 864 (1964).
11. R. M. Dreizler, E. K. U. Gross, *Density Functional Theory: An Approach to the Quantum Many-Body Problem*, Springer-Verlag, (1990).
12. W. Kohn, L. J. Sham, Phys. Rev. A **140** 1133(1965).
13. K. Burke, J. P. Perdew, and M. Levy, *Modern Density Functional Theory: A Tool for Chemistry*, Amsterdam (1995).
14. C. Lee, W. Yang, R. G. Parr, Phys. Rev. B. **37**, 785(1988).
15. P. M. W. Gill, Mol. Phys. **89**, 433 (1996).

## CHAPTER 3

### SYNTHESES OF FERRITES AND COPPER CHROMIUM SELENIDE NANOCRYSTALS

Reproduced in part with permission from [Wang, Y.-H. A. *et al. J. Am. Chem. Soc.* **129**,12408–12409 (2007).] Copyright [2007] American Chemical Society. [Bao, N. *et al. J. Am. Chem. Soc.* **129**, 12374-12375 (2007).] Copyright [2007] American Chemical Society. [Bao, N. *et al. J. Am. Chem. Soc.* **131**, 12900-12901 (2009).] Copyright [2009] American Chemical Society.

In this chapter, the syntheses of nanocrystals using thermolysis of precursors will be presented. We have used the simple metal-oleate precursors for synthesizing monodisperse spinel ferrites,  $MFe_2O_4$  ( $M = Co, Ni, Mn, Fe, \text{etc.}$ ), and metal-acetylacetonate precursor for synthesizing copper chromium selenide. We are able to control the size and shape of the nanocrystals and they readily form a colloidal suspension in a number of organic solvents.

#### 3.1 Size and Shape Controlled Synthesis of Monodisperse Ferrite Nanocrystals

The spinel ferrites of composition  $MFe_2O_4$  ( $M = Co, Ni, Mn, Fe, \text{etc.}$ ) exhibit interesting magnetic, magnetoresistive, and magnto-optical properties that are potentially useful for a broad range of applications.<sup>1</sup> Their magnetic properties can be systematically varied by changing the identity of the divalent  $M^{2+}$  cation or by partial substitution while maintaining the basic crystal structure.<sup>1</sup> The properties can additionally be tuned by controlling the shape, size, and crystallinity of the nanocrystals. For biomedical application, the use of spherical ferrite nanocrystals with a smooth surface, narrow size distribution, and high magnetic moment is desirable.<sup>2</sup> On the other hand, monodisperse ferrite nanocrystals with a preferential magnetic easy axis direction are needed for nanodevice and data storage applications. Thus, a simple and cost-effective synthesis route for large-scale production of monodisperse ferrite nanocrystals, with tunable shape and size, would be very attractive for practical applications.

My colleagues, especially Dr. Ningzhong Bao, and I have synthesized monodisperse ternary ferrite ( $MFe_2O_4$ ,  $M = Co, Ni, Mn,$  and  $Fe$ ) nanocrystals through a facile and general route involving thermolysis of an intimately mixed binary metal-oleate complex with similar decomposition temperature of the constituents.<sup>3</sup> In addition, novel shape- and structural-controlled superparamagnetic nanostructures composed of self-supported spherical and rod-like  $CoFe_2O_4$  colloidal nanocrystals have been prepared.<sup>4</sup>

### 3.1.1 Synthesis of Monodisperse Metal Ferrites Nanocrystals

Synthesis of metal oleate complexes: The mixed metal ( $M^{2+}Fe_2^{3+}$ )-oleate complexes (expressed as  $M^{2+}Fe_2^{3+}(C_{18}H_{33}O_2)_8^-$ , where  $M^{2+}$  are  $Co^{2+}, Ni^{2+}, Mn^{2+}, Fe^{2+},$  and  $Cu^{2+}$ ) were prepared by reaction of sodium oleate and the respective metal chlorides (the mixture of  $Fe^{3+}$  and  $M^{2+} = Co^{2+}, Ni^{2+}, Mn^{2+}, Fe^{2+}$  and  $Cu^{2+}$ ). For example, in the synthesis of  $Co^{2+}Fe_2^{3+}(C_{18}H_{33}O_2)_8^-$ , 4 mmol  $FeCl_3$ , 2 mmol  $CoCl_2$ , 16 mmol sodium oleate ( $C_{18}H_{33}NaO_2$ ), 10 ml  $H_2O$ , 10 ml ethanol and 20 ml hexane were mixed and refluxed at  $60^\circ C$  for 4 h. The mixed  $Co^{2+}Fe_2^{3+}$ -oleate complex ( $CoFe_2(C_{18}H_{33}O_2)_8$ ) was obtained by the separation of the water phase and subsequent evaporation of the residual ethanol and hexane at  $70^\circ C$ , and water at  $110^\circ C$ .

Synthesis of monodisperse ferrite nanocrystals: Monodisperse  $MFe_2O_4$  nanocrystals were obtained by thermolysis of the  $M^{2+}Fe_2^{3+}$ -oleate complex dissolved in 1-octadecene at  $300^\circ C$  under  $N_2$ . The size and shape of the synthesized  $MFe_2O_4$  nanocrystals were investigated using transmission electron microscopy (TEM). Figure 3.1 shows representative images of four different ferrites. The shape and average size vary from cubic for 9 nm  $CoFe_2O_4$  (Figure A1), near-spherical for 11 nm  $NiFe_2O_4$  (Figure B1), and perfectly spherical for both 7 nm  $MnFe_2O_4$  (Figure C1) and 24 nm  $FeFe_2O_4$  (Figure D1). All of the products have narrow size distributions

(~5 %, the size distribution is obtained by measuring the actual size of a large number of nanocrystals and then calculating the standard deviation). The insets show the high-resolution images of the various ferrites. Lattice fringes corresponding to a group of atomic planes within each particle are clearly visible, indicating the

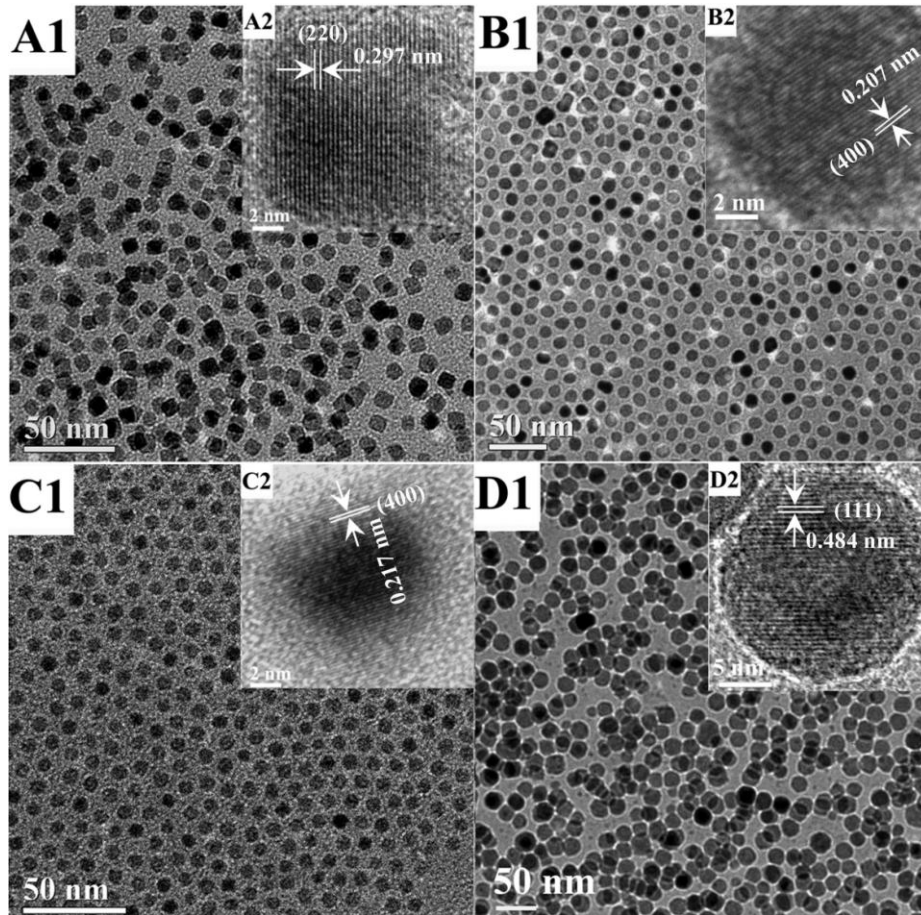


**Figure 3.1** TEM images of  $MFe_2O_4$  nanocrystals: (A1)  $CoFe_2O_4$ ; (B1)  $NiFe_2O_4$ ; (C1)  $MnFe_2O_4$ ; (D1)  $FeFe_2O_4$  ( $Fe_3O_4$ ). The corresponding high resolution TEM image of the individual nanocrystals is shown in the inset.

single crystalline nature of the nanocrystals. The crystallinity and structure of the  $MFe_2O_4$  nanocrystals were also confirmed by powder X-ray diffraction (XRD). As shown in Figure 3.2, the peak position and relative intensity of all diffraction peaks for the four products match well with standard powder diffraction data. From the peak widths, the average crystalline size is

estimated to be 10.4 nm for  $\text{CoFe}_2\text{O}_4$ , 12.6 nm for  $\text{NiFe}_2\text{O}_4$ , 7.8 nm for  $\text{MnFe}_2\text{O}_4$ , and 20.2 nm for  $\text{FeFe}_2\text{O}_4$ , agreeing with the TEM results.

The room-temperature hysteresis loop of the ferrites was measured using a vibrating sample magnetometer (VSM). The magnetization curves, as shown in Figure 3.3, display relatively high

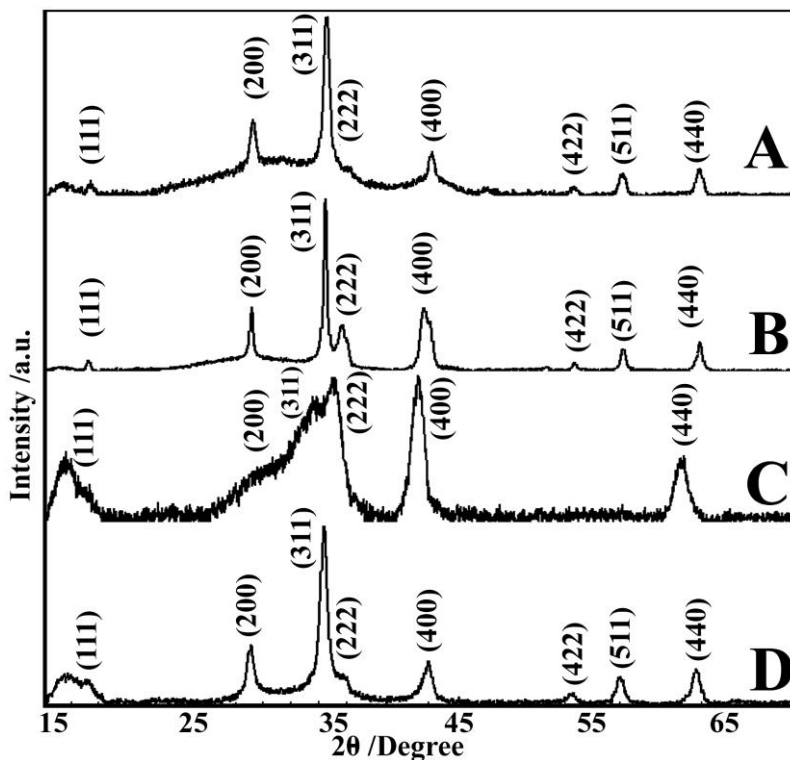


**Figure 3.2** XRD patterns of  $\text{MFe}_2\text{O}_4$  nanocrystals: (A)  $\text{CoFe}_2\text{O}_4$ ; (B)  $\text{NiFe}_2\text{O}_4$ ; (C)  $\text{MnFe}_2\text{O}_4$ ; (D)  $\text{FeFe}_2\text{O}_4$  ( $\text{Fe}_3\text{O}_4$ ).

saturation magnetization. The magnetic saturation values of  $\text{CoFe}_2\text{O}_4$ ,  $\text{NiFe}_2\text{O}_4$ , and  $\text{FeFe}_2\text{O}_4$  are 69.7, 34.2, and 58.6 emu/g, respectively, close to the theoretical values of 71.2, 47.5, and 96.2 emu/g. The observed values are within the range reported in the literature.<sup>1,5</sup> However, the  $\text{MnFe}_2\text{O}_4$  nanocrystals exhibit a low saturation magnetization of 23.9 emu/g, which is much smaller than the theoretical values of 120.8 emu/g. The reduced saturation magnetization of ferrite nanocrystals is generally believed to be due to the decreased particles size and presence of

a magnetic dead or antiferromagnetic layer on the surface.<sup>6</sup> As indicated by the ZFC-FC curves in the inset of Figure 3.3, the  $\text{MnFe}_2\text{O}_4$  has a low blocking temperature ( $\sim 140$  K) as compared

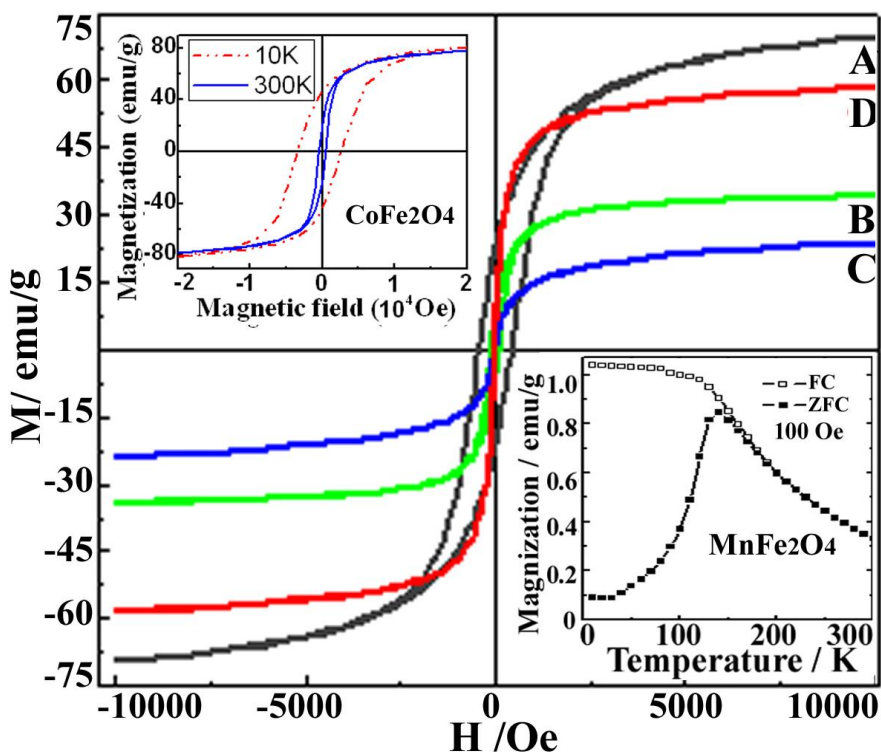


**Figure 3.3** Room-temperature magnetic hysteresis of  $\text{MFe}_2\text{O}_4$  nanocrystals: (A)  $\text{CoFe}_2\text{O}_4$ ; (B)  $\text{NiFe}_2\text{O}_4$ ; (C)  $\text{MnFe}_2\text{O}_4$ ; (D)  $\text{FeFe}_2\text{O}_4$  ( $\text{Fe}_3\text{O}_4$ ). The insets are hysteresis loops of  $\text{CoFe}_2\text{O}_4$  measured at 10 and 300 K (top), and zero-field-cooled (ZFC) and field-cooled (FC) magnetization of  $\text{MnFe}_2\text{O}_4$  measured in an applied field of 100 Oe (bottom).

with that of other ferrites. This is because of the smaller size and lower Curie temperature ( $\sim 300$  °C in the bulk) than the other ferrites. Other than  $\text{CoFe}_2\text{O}_4$ , the hysteresis loops for the other ferrites display very low coercivities, with no remanence, as would be expected for superparamagnetic behavior. Despite the relatively small size, the  $\text{CoFe}_2\text{O}_4$  nanocrystals display a markedly high coercivity of 430 Oe at room temperature and 3000 Oe at 10 K. This is likely because of its higher magnetocrystalline anisotropy because of spin-orbit contribution as compared to the other ferrites. On the basis of Langevin fits<sup>7</sup> to the magnetization loops, the average size of superparamagnetic  $\text{MnFe}_2\text{O}_4$  and  $\text{FeFe}_2\text{O}_4$  nanocrystals is estimated to be 5.2 and

19.8 nm, respectively, which are very close to the observed sizes of 7.8 and 20.2 nm from TEM images.

### 3.1.2 Synthesis of Spherical and Rod-Like $\text{CoFe}_2\text{O}_4$ Nanostructures

In this section, the shape- and structure-controlled synthesis of self-supported monodisperse cobalt ferrite ( $\text{CoFe}_2\text{O}_4$ ) superparamagnetic (SP) nanostructures of both spherical and cubic morphology will be described. The individual nanostructures are composed of intergrown spherical or rod-like  $\text{CoFe}_2\text{O}_4$  nanocrystals. This results in the formation of larger more complex nanostructures with tunable morphology, size, structure, and magnetic properties.

#### Synthesis of self-supported spherical nanostructures of inter-grown spherical $\text{CoFe}_2\text{O}_4$ nanocrystals.

For the synthesis of spherical nanostructures, 5 g of the mixed metal ( $\text{Co}^{2+}\text{Fe}_2^{3+}$ )-oleate complex, 20 ml 1-octadecene, and 0.5 g oleic acid were mixed and magnetically stirred for 1 hour under flowing  $\text{N}_2$ . The mixture was then heated to 320 °C at a heating rate of 10 °C/min and maintained at this temperature for up to 3h under  $\text{N}_2$  flow with continuous stirring. A small amount (0.05 ml) of hexane was injected into the reaction system at 300, 305, 310, 314, 316, 318, 320 °C, during heating, and also at 320 °C after aging for 0, 2, 5, 10, 17, 25, 30, 70, 85, and 95 minutes. A burst of boiling accompanied by a temperature drop (maximum of about 10 °C) due to the evaporation of hexane was observed following each injection. The final product, in the form of a black powder, prepared after aging at 320 °C for 3h minutes was obtained by centrifugation at 8000 rpm for 15 minutes, which was then washed with hexane several times and then dried.

#### Synthesis of self-supported cubic nanostructures of inter-grown rod-like $\text{CoFe}_2\text{O}_4$ nanocrystals.

For the synthesis of cubic nanostructures, 5 g of the mixed metal ( $\text{Co}^{2+}\text{Fe}_2^{3+}$ )-oleate complex, 20 ml 1-octadecene, and 0.5 g oleic acid were mixed and magnetically stirred for 1 hour under flowing  $\text{N}_2$ . The mixture was then heated to 320 °C at a heating rate of 5 °C/min and maintained at this temperature for up to 3h under  $\text{N}_2$  flow with continuous stirring. A small amount (0.05 ml) of hexane was injected into the reaction system at 300, 310, 314, 318, 320 °C, during heating, and also at 320 °C after aging for 0, 2, 4, 6, 8, 10, 12, 20, 30, 45, 75, and 95 minutes. A burst of boiling accompanied by a temperature drop (maximum of about 10 °C) due to the evaporation of hexane was observed following each injection. The final product, in the form of a black powder, prepared after aging at 320 °C for 3h minutes was obtained by centrifugation at 8000 rpm for 15 minutes, which was then washed with hexane for several times and then dried.

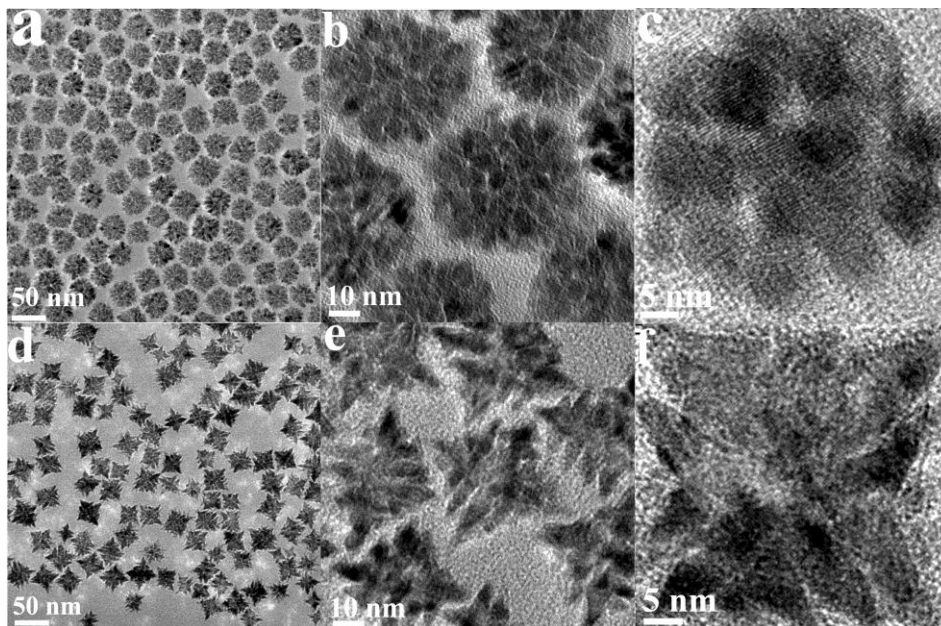


**Figure 3.4** TEM images of monodisperse self-supported (a-c) spherical and (d-f) cubic nanostructures composed of intergrown spherical and rodlike  $\text{CoFe}_2\text{O}_4$  nanocrystals, respectively.

The shape, size, and structure of the as-synthesized  $\text{CoFe}_2\text{O}_4$  nanostructures have been investigated using transmission electron microscopy (TEM). Figure 3.4 shows typical TEM

images of two different nanostructures obtained by aging at 320 °C for 2 min. By merely changing the heating rate, the product shape and size vary from being spherical ( $40.5\pm 4.5$  nm, Figure 3.4a-c) to cubic ( $36.5\pm 2.5$  nm, Figure 3.4d-f). These nanostructures are composed of individual spherical nanocrystals of  $<5$  nm in size (Figure 3.4c) or nanorods with dimensions of  $\sim 3.6$  nm in diameter and  $<25$  nm in length (Figure 3.4f), respectively. They can form highly ordered two-dimensional (2D) assemblies over a large area.

To better understand the formation mechanism, we studied the nucleation, self-assembly, and secondary growth of the  $\text{CoFe}_2\text{O}_4$  nuclei leading to the formation of the nanostructures shown in Figure 3.4. Without hexane injection, only monodisperse nanocrystals are formed through initial homogeneous nucleation and subsequent diffusion-controlled growth of the initial nuclei.<sup>8</sup> With interval injection of hexane into the reaction mixture during the heating cycle, novel types of complex nanostructures (Figure 3.4) are produced. This is likely because the burst boiling accompanied by a temperature drop slows down the growth of the nuclei and promotes their assembly to form clusters by particle coalescence (from interaction between the nuclei)<sup>8</sup> or oriented attachment<sup>9</sup> to decrease the surface energy. The uniform nuclei initially formed at 305°C during synthesis of both types of nanostructures are the same as those formed without hexane injection but are difficult to observe because of the very small size ( $<2$  nm). However, with increasing the temperature to 314°C, novel monodisperse nanostructures composed of assembled nanocrystals are produced, which is very different from the monodisperse single-crystalline nanocrystals formed in a steady heating process without hexane injection.<sup>10</sup>

The room-temperature magnetization curves (Figure 3.5a) display relatively high saturation magnetization values of 40.2 and 49.5 emu/g for the spherical and cubic nanostructures, respectively, after 2 min of aging at 320°C. These values are, however, somewhat lower than the

bulk value (71.2 emu/g). The unique self-supported nanocrystal assemblies exhibit SP behavior at room temperature even though the size of an individual assembly exceeds 10 nm. The hysteresis loop shows essentially no coercivity ( $H_C$ ) for the spherical nanostructures and a low value of 134

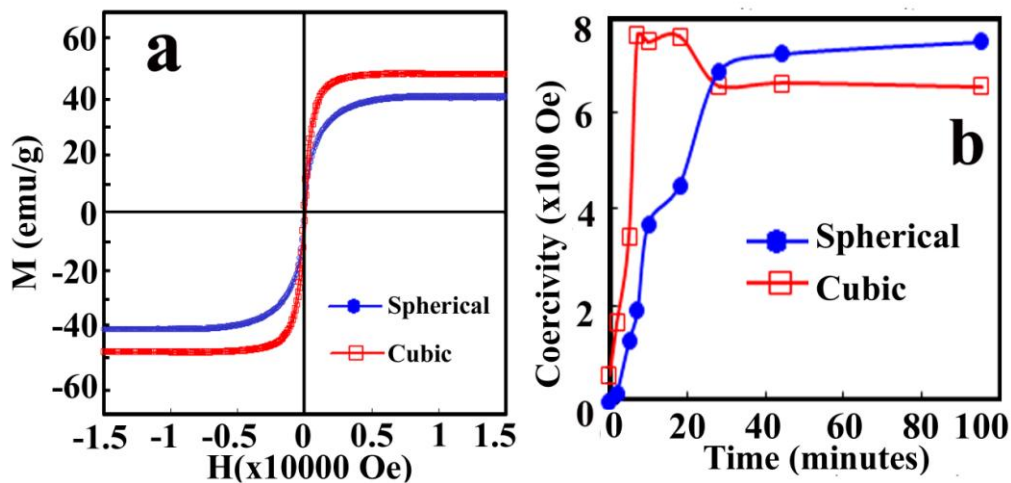


**Figure 3.5** (a) Room-temperature hysteresis loops of spherical and cubic nanostructures after 2 min aging at 320 °C. (b) The change in the coercivity of spherical and cubic nanostructures versus aging time.

Oe for the cubic nanostructures, suggesting that the crystalline subunits are magnetically decoupled. Based on Langevin fits<sup>7</sup> to the magnetization loops at 300 K, the estimated sizes are 3.9 nm in diameter for the spherical nanostructures and 8.2 nm in length (assuming a 3.6 nm rod diameter) for the cubic nanostructures, respectively. These values match well with the average sizes of the nanocrystal subunits observed by TEM. The thermal energy can overcome the anisotropy energy barrier for these sizes and the net magnetization of the nanocrystal assemblies in the absence of an external field averages to zero. After prolonged aging for 3 h, both the saturation magnetization and the coercivity for the spherical nanostructures at room temperature increase to 50.6 emu/g and 540 Oe, respectively. Similarly, the saturation magnetization for the cubic nanostructures increases to 62.3 emu/g, and the coercivity to 1200 Oe. Thus, improved coalescence of the crystallites in the nanostructures results in increased magnetic coupling and higher magnetization.

### 3.2 Size-Controlled Synthesis of $\text{CuCr}_2\text{Se}_4$ Nanocrystals

Nanocrystals (15-30 nm) of the magnetic chalcogenide  $\text{CuCr}_2\text{Se}_4$  have been synthesized using a facile solution-based method with good size control. They have close to cubic morphology with a narrow size distribution and exhibit superparamagnetic behavior at room temperature.

#### 3.2.1 Introduction

The controlled synthesis of inorganic nanocrystals (NCs) has generated much interest in recent years, motivated in large part by the unusual electronic, optical and magnetic properties that are exhibited in this size regime.<sup>9a</sup> Controlling the growth of NCs of widely divergent shapes and sizes is non-trivial and in most cases the crystals adopt thermodynamically favored forms, including spheres, cubes, hexagons, rods, wires, etc.<sup>11</sup> The solution-based synthesis of a wide range of magnetic NCs of different morphologies has been reported, including those of transition metals (Fe, Co, Ni), alloys (FePt, CoPt, etc), and oxide materials (ferrites, perovskites, etc).<sup>9a,13</sup> Their properties have been studied quite extensively, both from the viewpoint of fundamental understanding and applications, ranging from magnetic resonance imaging, drug delivery, biosensing, and nanoelectronic devices.<sup>12</sup> These studies notwithstanding, the synthesis and properties of a number of other nanocrystalline magnetic materials, such as those based on the rare earths and chalcogenides, remain largely unexplored. Of particular interest are the chromium-based spinel chalcogenides,  $\text{ACr}_2\text{X}_4$  (A= Cu, Cd, Hg, Fe, Co; X = S, Se, Te),<sup>13</sup> which are ferro/ferrimagnetic insulators, semiconductors, or even metals that display unique properties in the bulk.<sup>14,15</sup> As in the case of the standard magnetic systems, the utility of the chalcospinels

can be augmented if they can be synthesized as colloidal nanocrystals with highly controlled dimensions.

Room temperature ferromagnetism with a Curie temperature of 430 K makes  $\text{CuCr}_2\text{Se}_4$  an interesting system of study amongst the chalcospinel. <sup>13</sup> Additionally, it is metallic and exhibits a pronounced magneto-optic Kerr effect at room temperature. <sup>15</sup> Solution-based synthesis of  $\text{CuCr}_2\text{Se}_4$  and other chalcospinels has, however, been limited by the complexity involved in the synthesis; particularly since they cannot be precipitated from aqueous solution. Furthermore, it is difficult to synthesize the stoichiometric compound and/or the desired spinel phase because of the volatility of Se and the availability of a number of oxidation states of chromium. <sup>13,16</sup> Recently, there have been reports of solution-based solvothermal <sup>17</sup> and microwave synthesis <sup>18</sup> of  $\text{CuCr}_2\text{Se}_4$  crystals. While the phase-pure material has been stabilized, these reactions result in the formation of relatively large crystallites or agglomerates with a broad size and shape distribution. The facile synthesis of size-controlled  $\text{CuCr}_2\text{Se}_4$  nanocrystals (~15-30 nm) that are nearly monodisperse and readily form a colloidal suspension is described in this chapter.

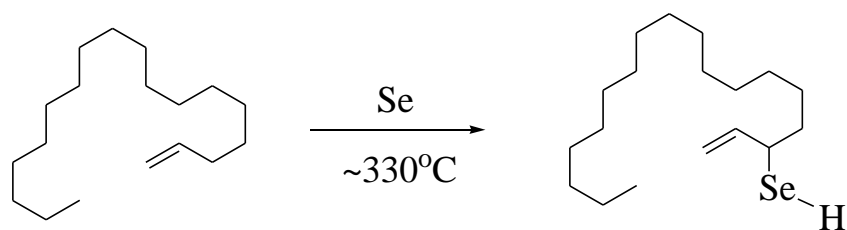
### 3.3 Synthesis of $\text{CuCr}_2\text{Se}_4$ Nanocrystals

The synthesis of  $\text{CuCr}_2\text{Se}_4$  nanocrystals can be divided into two parts. One is the synthesis of selenide source and the second part is the synthesis of  $\text{CuCr}_2\text{Se}_4$  nanocrystals using selenium complexes as anion source. Both parts will be described in this section.

#### 3.3.1 Synthesis of 1-Octadecene /Selenium Complex

The ODE-Se complex was obtained using selenium powder (2.4 mmol) dissolved in 1-octadecene (8 ml) at 330°C. The solution was cooled to room temperature and 3 ml hexane was

added to isolate the ODE-Se complex (scheme 3.1.) and then filtered for the nuclear magnetic resonance (NMR) and mass spectrometry (MS) analysis. Adequate precaution was taken in the handling and disposal of selenium and its products since they are generally quite toxic and can cause eye, skin, digestive tract and respiratory tract irritation.



**Scheme 3.1** The allylic insertion reaction of Se with 1-octadecene (ODE) to form ODE-Se.

**ODE-Se.**  $^1\text{H}$  NMR ( $\delta$ ,  $\text{CDCl}_3$ , 500MHz): 0.87 (t, 3H,  $-\text{CH}_3$ ), 1.26 (m, 26H,  $-\text{C}_{13}\text{H}_{26}\text{CH}_3$ ), 1.62 (q, 2H,  $-\text{CHSeCH}_2-$ ), 2.14 (s, 1H,  $-\text{CHSe}-$ ), 4.93 (d, 1H,  $\text{CH}_2=\text{CH}-$ ), 5.01 (d, 1H,  $\text{CH}_2=\text{CH}-$ ), 5.39 (q, 1H,  $\text{CH}_2=\text{CHCHSe}-$ ). Mass spectrum: (FAB positive)  $m/z$  333  $[\text{C}_{18}\text{H}_{36}\text{Se}+\text{H}]^+$ .

### 3.3.2 Synthesis of Magnetic $\text{CuCr}_2\text{Se}_4$ Nanocrystals

In a typical reaction for the synthesis of 15 nm average diameter NCs, 2.4 mmol selenium (Se) powder was dissolved in 8 ml of OLA at  $330^\circ\text{C}$  under nitrogen atmosphere and then cooled down to room temperature. Separately, 0.3 mmol of copper (II) acetylacetonate (acac) and 0.6 mmol of chromium (III) acetylacetonate (acac) were co-dissolved in 2 ml of OLA at  $\sim 175^\circ\text{C}$  under vacuum and then backfilled with nitrogen. After cooling down to room temperature, the mixture was injected under nitrogen atmosphere into the Se solution and the resulting mix heated up to  $350^\circ\text{C}$  in 30 minutes. The reaction mixture was maintained at this temperature for 1 hour while being continually stirred, during which a brown-black solution was formed. After cooling down to room temperature, a mixture of hexane and ethanol (1:3) was added to the solution and a

black product with yield in the range of 70-85 % was isolated via centrifugation (6000 rpm). The average size of the NCs could be systematically increased up to 30 nm by using a solvent mixture of OLA and ODE. For example, to synthesize 25 nm CuCr<sub>2</sub>Se<sub>4</sub> NCs, a solvent mixture ODE and OLA with volume ratio of 1:1 was used for dissolution and formation of the selenium compound. The other reaction steps were the same as those used for the synthesis of the smaller NCs. Interestingly, for higher concentrations of ODE (above ~75 %) the average size again decreased, with ~18 nm crystals being obtained using pure ODE.

We have found that 100 % excess Se is optimum for the CuCr<sub>2</sub>Se<sub>4</sub> nanocrystal synthesis. A significantly broader size distribution of the product and/or formation of secondary phases, such as CuCrSe<sub>2</sub>, are observed at much higher or lower concentrations. Similarly, lowering the Se reaction temperature from 330°C to 270°C results in the formation of random shaped NCs. Based on nuclear magnetic resonance and mass spectral data we conclude that while both ODE and OLA can react with Se at 330°C, only the latter is effective at the lower temperature. Based on this and other reported mechanisms in the literature,<sup>15,16</sup> The proposed reaction scheme using OLA as solvent as following:  $\text{Cu}(\text{acac})_2 + 2 \text{Cr}(\text{acac})_3 + 8 \text{C}_{18}\text{H}_{36}\text{NSeH} \rightarrow \text{Cu}(\text{C}_{18}\text{H}_{36}\text{NSe})_2 + 2 \text{Cr}(\text{C}_{18}\text{H}_{36}\text{NSe})_3 + 8 (\text{acac})\text{-H} \rightarrow \text{CuCr}_2\text{Se}_4 + \text{C}_{18}\text{H}_{35} + 4 \text{H}_2\text{Se} + 8 (\text{acac})\text{-H}$ . In addition, tri-octyl phosphine is not suitable as a solvent because of its reaction with the chromium intermediate; addition of oleic acid or tri-octyl phosphine oxide as surfactants to the OLA/ ODE solvent mixture does not result in any significant size or shape variations.

### 3.4 Characterizations and Magnetic Properties of $\text{CuCr}_2\text{Se}_4$ Nanocrystals

The morphology of the synthesized nanocrystals has been investigated using TEM. As shown in Fig. 3.6, the NCs synthesized using OLA+ODE, with an average size of 25 nm, exhibit close to cubic morphology. A similar shape is observed for the smaller size NCs. The NCs are close to

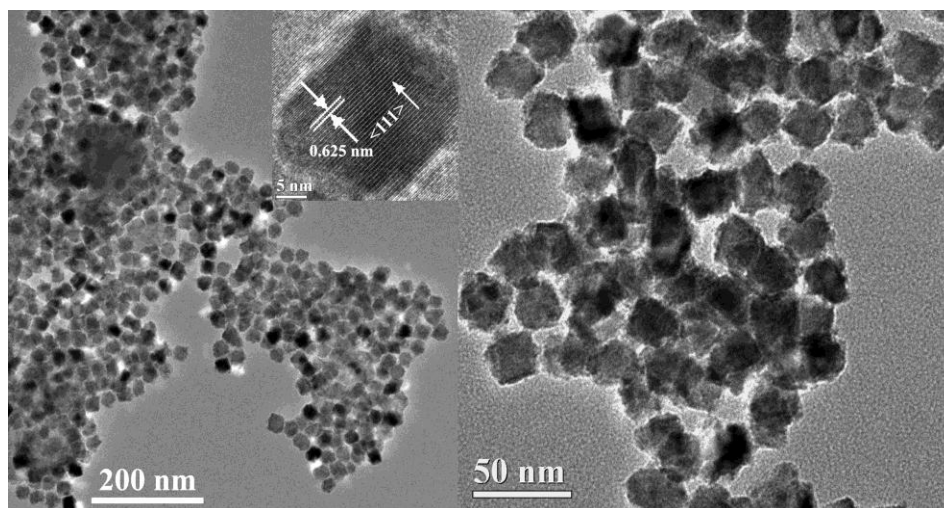


**Figure 3.6** TEM and HRTEM images of  $\text{CuCr}_2\text{Se}_4$  nanocrystals with an average size of 25 nm.

monodisperse, as seen in Fig. 3.6, with a size distribution of  $\pm 15\%$ . A similar distribution is obtained for the 18 nm NCs. The inset to Fig. 3.6 shows the high resolution TEM (HRTEM) image of a NC that exhibits lattice fringes. A lattice spacing of  $d=0.625$  nm is observed, corresponding to the (111) lattice planes of the face-central cubic chalcospinel phase.

As shown in Fig. 3.7, the peak positions and relative intensities of all the x-ray diffraction peaks for the 15 and 25 nm NCs match well with the powder diffraction data for  $\text{CuCr}_2\text{Se}_4$  (JCPDS No. 81-1986). As expected, the peaks are broader for the smaller size NCs. From the peak widths, the average crystalline size is estimated to be 16.3 and 22.9 nm, respectively, which is in very good agreement with the TEM results. The composition has also been confirmed using energy dispersive x-ray analysis (EDX), which indicates that the Cu:Cr:Se concentration to be very close to the expected 1:2:4 ratio for these two samples.

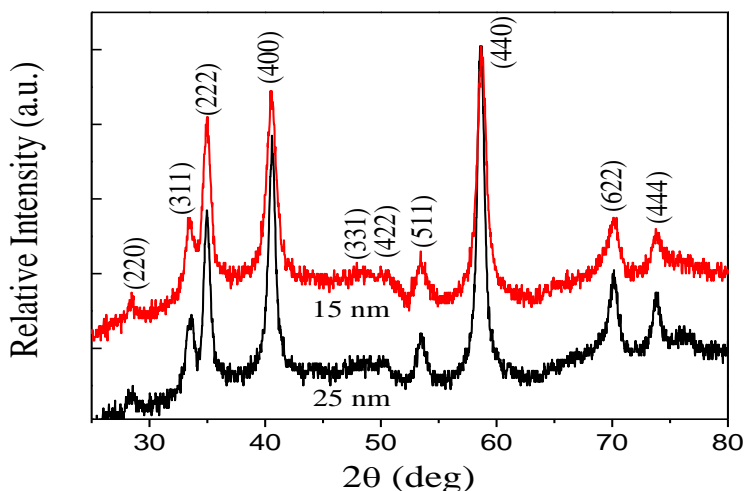


**Figure 3.7** X-ray powder diffraction patterns (using a Co  $K\alpha$  source,  $\lambda = 1.789 \text{ \AA}$ ) of: a) 15 nm and b) 25 nm size NCs.

Figure 3.8 (left panel) shows the temperature dependence of the ZFC and FC magnetization for the four samples measured in a magnetic field  $H = 50 \text{ Oe}$ . The Curie temperatures ( $T_C$ 's), estimated from the  $M(T)$  inflection point for each curve, ranges between 395 - 409 K, which is lower than the reported  $T_C$  of 430 K for single crystal samples<sup>19</sup>. The magnetization curves exhibit a behavior resembling superparamagnetic relaxation when considering that the ZFC and FC magnetization bifurcate and the ZFC curve demonstrates a broad peak. In addition, while the FC magnetization continues to increase with decreasing temperature for the 15 and 18 nm samples, the FC magnetization is essentially constant below 150 K for the 25 and 30 nm samples. The latter is characteristic of a dense magnetic nanoparticle system exhibiting spin-glass behavior, the so called superspin glass<sup>20,21</sup>. This behavior can be explained by the fact that the free-energy difference between the two states of a spin cluster is determined not only by the Zeeman energy, but also by the interactions between the cluster and its surroundings. For small magnetic fields the latter contribution is dominant and correspondingly the low temperature branch of the FC magnetization levels off with decreasing temperature.

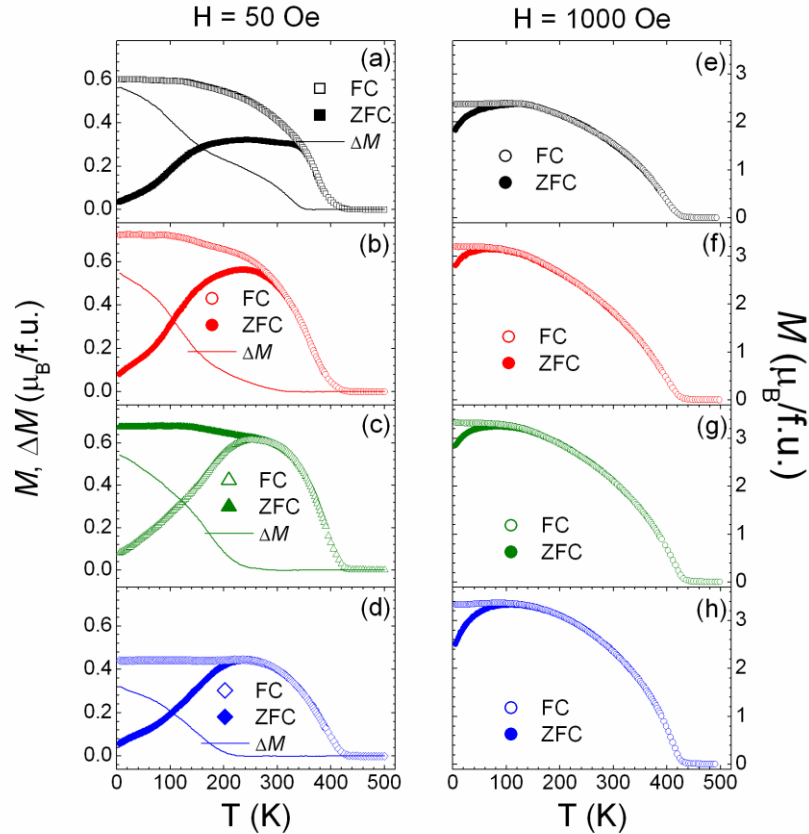


**Figure 3.8** Temperature dependence of the ZFC (solid symbols) and FC (open symbols) magnetization for  $\text{CuCr}_2\text{Se}_4$  nanocrystals with different average size: (a) 30 nm, (b) 25 nm, (c) 18 nm, and (d) 15 nm for a magnetic field  $H = 50$  Oe.  $\Delta M$  is the difference  $M_{\text{FC}} - M_{\text{ZFC}}$ . The same data for samples (e) 30 nm, (f) 25 nm, (g) 18 nm, and (h) 15 nm for  $H = 1000$  Oe are shown on the right.

In thermodynamic equilibrium, the ZFC and FC magnetization should be the same,  $M_{\text{FC}} = M_{\text{ZFC}}$ , while the thermoremanent magnetization ( $M_{\text{TRM}}$ ), *i.e.* when the sample is cooled in a field and the magnetization is recorded in zero field during reheating is zero. However, in an irreversible regime the FC magnetization is expected to be different from ZFC magnetization,  $M_{\text{FC}} \neq M_{\text{ZFC}}$ . The ZFC magnetization of a spin glass exhibits a linear response to small magnetic fields and the principle of superposition can be applied<sup>22</sup>:  $\Delta M = M_{\text{FC}} - M_{\text{ZFC}} = M_{\text{TRM}}$ . To emphasize the nonequilibrium character of the spin glass state, the  $\Delta M(T)$  for all samples is also shown in the left panel of Fig.3.8. It should be noted that for classical superparamagnetic

particles  $\Delta M \sim \int_T^\infty T_B f(T_B) dT_B$ , where  $f(T_B)$  is a distribution function of blocking temperatures  $T_B$ <sup>23,24</sup>. This function is assumed to be a log-normal distribution and usually fits the experimental data quite well.

On the right panel of Fig. 3.8 we present the FC and ZFC magnetization curves for the same set of samples measured in a magnetic field  $H = 1000$  Oe. For this higher field the ZFC peak shifts to lower temperatures and the bifurcation temperature range between the ZFC and FC magnetization curves are very similar for the different size samples.

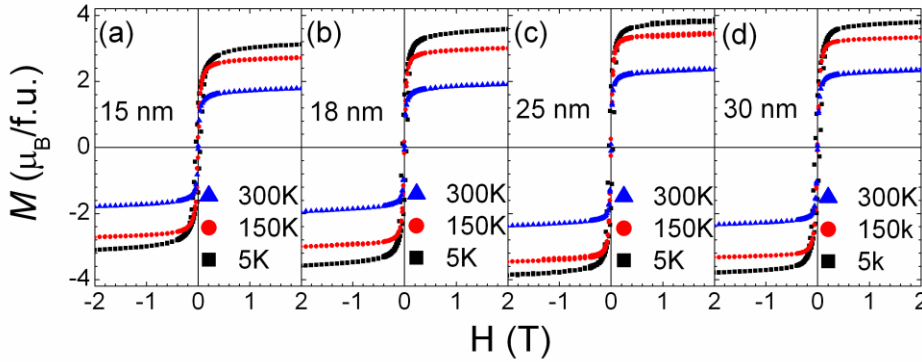


**Figure 3.9** Field dependence of the magnetization  $M$  of  $\text{CuCr}_2\text{Se}_4$  samples: (a) 15 nm, (b) 18 nm, (c) 25 nm and (d) 30 nm measured at  $T = 300, 150$  and 5 K.

The magnetization,  $M$ , as a function of magnetic field,  $H$ , acquired at  $T = 5, 150$  and 300 K for the four samples are shown in Fig. 3.9. The values of the saturation magnetization,  $M_S$ , and the coercivity,  $H_C$ , derived from Fig. 3.9 are plotted in Fig. 3.10. The  $M_S$  values at 5 K range between 3.2 to 3.9  $\mu_B/\text{f.u.}$ , which are smaller than the reported values of 5.07  $\mu_B/\text{f.u.}$  from reference 14 and 5.2  $\mu_B/\text{f.u.}$  from reference 25, both obtained for bulk single crystals. The measured  $M_S$  values are also somewhat lower than that reported for sub-micron size  $\text{CuCr}_2\text{Se}_4$  particles prepared by solvothermal and thermolysis methods<sup>26,27</sup>. As seen in Fig. 3.10, a relatively high coercive field is obtained at low temperatures ( $H_C = 410 - 470$  Oe at 5 K) for the different size nanocrystals, but sharply drops essentially to zero at room temperature. Analysis of the  $M$

( $H$ ) curves reveals that the data does not collapse on to a single curve when plotted as a function of  $H/T$ . This suggests that the nanocrystals do not display an ideal superparamagnetic behavior.

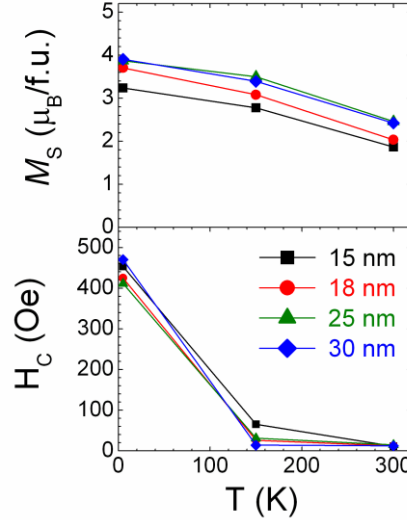


**Figure 3.10** Saturation magnetization moments  $M_S$  and coercivities  $H_C$  for  $\text{CuCr}_2\text{Se}_4$  samples as derived from figure 3.9.

Despite the deviation of the sample behavior from a classic superparamagnetic system, we have attempted to fit the experimental  $M(H)$  curves with a Langevin function incorporating a distribution of particle volume<sup>27</sup>:

$$\frac{M(H)}{M_S} = \frac{\int_0^{\infty} Lf(y)dy}{\int_0^{\infty} f(y)dy}, \quad (3.1)$$

where  $L(x) = \coth x - 1/x$  is the Langevin function,  $x = M_S V H / k_B T$ ,  $V = \pi D^3 / 6$ ,  $D$  is the particle diameter,  $f(y)$  is a volume distribution function, where  $y = D / D_V$  is the reduced diameter and  $D_V$  is the median diameter of the distribution. As is usually assumed in the literature for analyzing superparamagnetic nanoparticles, we have used a log-normal distribution given by the following equation:

$$f(y) = \frac{1}{y\sigma\sqrt{2\pi}} \exp\left(-\frac{(\ln y)^2}{2\sigma^2}\right), \quad (3.2)$$

where  $\sigma$  is the standard deviation and the parameter for fitting the experimental  $M(H)$  curves. The results of the calculations, as fits to the  $T = 300$  K experimental magnetization data, are shown by solid lines in Fig. 3.11 for the (a) 15 nm, (b) 18 nm and (c) 25 nm samples. The

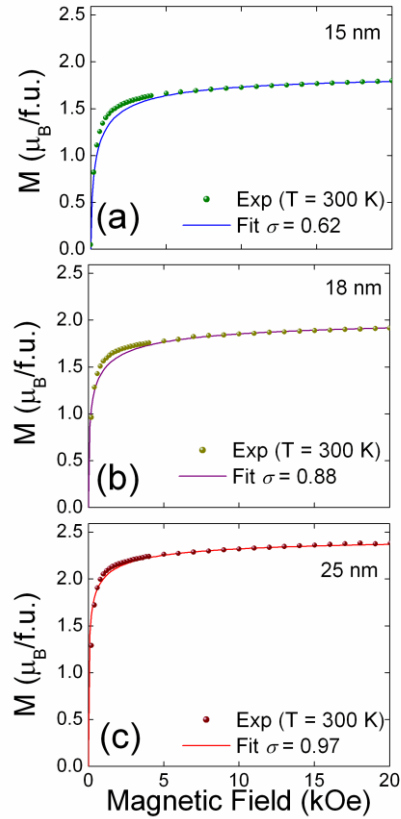


**Figure 3.11** Fit of the experimental  $M(H)$  curves at  $T = 300$  K with the Langevin function incorporating a log-normal distribution function with a standard deviation  $\sigma$  for samples: (a) 15 nm, (b) 18 nm and (c) 25 nm.

respective median particle diameter  $D_V$  are used for the fitting and the deduced standard deviations  $\sigma$  are listed in the plots. The fitting curves deviate somewhat at low fields from the experimental data for  $D_V = 15$  and 18 nm samples, but a very good fit is obtained over the whole temperature range for  $D_V = 25$  nm.

The high-temperature magnetization measurements in the paramagnetic regime follow the Curie-Weiss behavior, as shown in Fig. 3.12 for the 25 nm sample. The molar Curie constant,

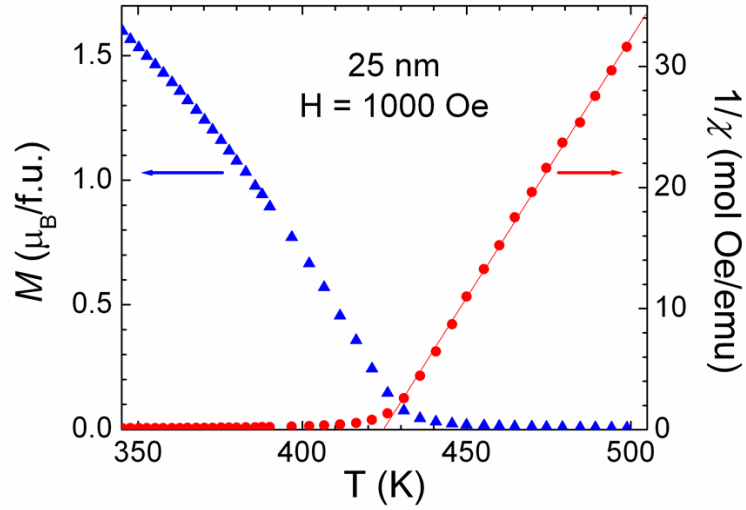


**Figure 3.12** Temperature dependence of the magnetization per formula unit and inverse magnetic susceptibility for the 25 nm sample,  $H = 1000$  Oe.

$C_M$ , and the asymptotic Curie-Weiss paramagnetic temperature,  $\theta$ , are determined to be 2.32 emu K/Oe mol and 425 K, respectively. From these parameters the effective magnetic moment of chromium is calculated using the relation  $\mu_{\text{eff}} = 2.83\sqrt{C_M/2}$  to be  $3.05 \mu_B$ , which smaller than that reported for a polycrystalline sample of  $\text{CuCr}_2\text{Se}_4$ <sup>28</sup>, but close to  $\mu_{\text{eff}} = 3.20 \mu_B$  measured for a single crystal sample<sup>18</sup>. However, the calculated value of  $\mu_{\text{eff}}$  is lower than the spin only value of  $\text{Cr}^{3+}$  ion of  $3.87 \mu_B$ . The experimental values for all the samples are summarized in Table 3.1. The also  $M_S$  values at  $T = 5$  K, as obtained from the data in Fig. 3.9, are also listed.

**Table 3.1** The experimental values of the molecular Curie constant  $C_M$ , effective magnetic moments in  $\mu_B$  per Cr ion, saturation magnetization in  $\mu_B$  per f.u. at  $T = 5$  K, Curie-Weiss temperatures  $\theta$ , and Curie temperatures  $T_C$  for different size  $\text{CuCr}_2\text{Se}_4$  nanocrystal samples.

Sample	$C_M$ (emu K/Oe mol)	$\mu_{\text{eff}}/\text{Cr}$ ( $\mu_B$ )	$M_S@5\text{K}$ ( $\mu_B/\text{f.u.}$ )	$\theta$ (K)	$T_C$ (K)
15 nm	1.73	2.64	3.24	419	395
18 nm	1.83	2.70	3.70	420	402
25 nm	2.32	3.05	3.87	425	414
30 nm	2.13	2.92	3.90	421	409

It is perhaps not surprising that the magnetic moment of the chalospinel nanocrystals is lower than that of the bulk material, as has been observed for a number of other systems<sup>29</sup>. This effect is attributed primarily to spin canting at the surface, i.e. disorientation of spin directions. Another effect of the disorder induced by the size confinement surface disorder is a decrease in the Curie temperature with the respect to the corresponding bulk value, which is also observed in our samples.

To summarize, we have developed a simple solution-based route for the synthesis of size-controlled cubic  $\text{CuCr}_2\text{Se}_4$  nanocrystals. The process involves the thermal decomposition of the metal acetylacetonate precursors and their reaction with complexed Se in a high boiling solvent mixture of OLA and ODE. In addition to acting as surfactants, the coordinating solvents form organo-Se adducts via insertion. Chalcopyrite structure  $\text{CuIn}_x\text{Ga}_{1-x}\text{Se}_2$  and  $\text{CuFeS}_2$  nanocrystals have been synthesized using similar process as  $\text{CuCr}_2\text{Se}_4$  synthesis. The detailed synthesis and properties of these materials are provided in Appendix I and II. We plan to expand the process for synthesizing other chalcospinel ( $\text{CuCr}_2\text{S}_4$ ,  $\text{CdCr}_2\text{S}_4$ ,  $\text{CdCr}_2\text{Se}_4$  etc.) nanocrystals, which are expected to exhibit unusual magnetic and transport properties.

### 3.5 References

1. (a) M. J. Sugimoto, *J. Am. Ceram. Soc.* **82**, 269-280 (1999). (b) S Yu, M. Yoshimura, *Chem. Mater.* **12**, 3805-3810 (2000). (c) M. Abe, M. Tada, N. Matsushita, Y. Shimada, *J. Appl. Phys.* **99**, 08M907 (2006). (d) C. Kim, J. Lee, S. Katoh, R. Murakami, M. Yoshimura, *Mater. Res. Bull.*, **36**, 2241-2250 (2001). (e) A. Subramani, N. Matsushita, T. Watanabe, M. Tada, M. Abe, M. Yoshimura, *J. Appl. Phys.* **101**, 09M504 (2007). (f) J. Park, J. Joo, S. Kwon, Y. Jang, T. Hyeon, *Angew. Chem., Int. Ed.*, **46**, 4630-4660 (2007). (g) X. Wang, J. Zhuang, Q. Peng, Y. Li, *Nature*, **437**, 121-124 (2005).
2. (a) Y. Sun, Y. Xia, *Science*, **298**, 2176-2179 (2002). (b) Y. L. Wang, Y. N. Xia, *Nano Lett.*, **4**, 2047-2050 (2004). (c) S. H. Gee, Y. K. Hong, D. W. Erickson, M. H. Park, *J. Appl. Phys.*, **93**, 7560-7562 (2003).

3. N. Bao, L. Shen, Y.-H. Wang, P. Padhan, A. Gupta, *J. Am. Chem. Soc.* **129**, 12374 (2007).
4. N. Bao, L. Shen, Y.-H. Wang, J. Ma, D. Mazumdar, A. Gupta, *J. Am. Chem. Soc.* **131**, 12900-12901 (2009).
5. (a) K. E. Mooney, J. A. Nelson, M. J. Wagner, *J. Chem. Mater.*, **16**, 3155 (2004). (b) C. Liu, B. Zou, A. J. Rondinone, Z. J. Zhang, *J. Am. Chem. Soc.*, **122**, 6263 (2000). (c) Y. Lee, J. Lee, C. J. Bae, J. G. Park, H. J. Noh, J. H. Park, T. Hyeon, *Adv. Funct. Mater.*, **15**, 503 (2005). (d) Z. J. Zhang, Z. L. Wang, B. C. Chakoumakos, J. S. Yin, *J. Am. Chem. Soc.*, **120**, 1800 (1998).
6. (a) B. Y. Geng, J. Z. Ma, X. W. Liu, Q. B. Du, M. G. Kong, L. D. Zhang, *Appl. Phys. Lett.*, **90**, 043120 (2007). (b) M. Zheng, X. C. Wu, B. S. Zou, Y. J. Wang, *J. Magn. Magn. Mater.*, **183**, 152 (1998). (c) Q. A. Pankhurst, R. J. Pollard, *Phys. Rev. Lett.*, **67**, 248 (1991).
7. B. D. Cullity, *Introduction to Magnetic Materials*; Addison-Wesley: 1972.
8. (a) H. Zheng, R. K. Smith, Y. Jun, C. Kisielowski, U. Dahmen, A. P. Alivisatos, *Science*, **324**, 1309 (2009). (b) V. Privman, D. V. Goia, J. Park, E. J. Matijevic, *Colloid Interface Sci.*, **213**, 36 (1999).
9. (a) Y. Yin, A. P. Alivisatos, *Nature*, **437**, 664 (2005). (b) R. L. Penn, J. F. Banfield, *Science*, **281**, 969 (1998). (c) A. Narayanaswamy, H. Xu, N. Pradhan, M. Kim, X. J. Peng, *J. Am. Chem. Soc.*, **128**, 10310 (2006).
10. (a) S. G. Kwon, Y. Piao, J. Park, S. Angappane, Y. N. Jo, M. Hwang, J. G. Park, T. Hyeon, *J. Am. Chem. Soc.*, **129**, 12571 (2007). (b) J. Park, K. An, Y. Huang, J. G. Park, H. J. Noh, J. Y. Kim, J. H. Park, N. M. Hwang, T. Hyeon, *Nat. Mater.*, **3**, 891 (2004).
11. Hyeon, T. *Chem. Commun.*, 927-934 (2003).
12. (a) K. G. Nikiforov, *Prog. Cryst. Growth and Charact. Mat.*, **39**, 1-104 (1999). (b) Landolt-Börnstein, *Magnetic and Other Properties of Oxides and Related Compounds: Vol. III/4b*, Springer, 1970.
13. (a) J. Hemberger, P. Lunkenheimer, R. Fichtl, H. A. K. von Nidda, V. Tsurkan, A. Loidl, *Nature*, **434**, 364-367 (2005). (b) A. P. Ramirez, R. J. Cava, J. Krajewski, *Nature*, **386**, 156 (1997).
14. H. Brandle, J. Schoenes, P. Wachter, F. Hullinger, *Appl. Phys. Lett.*, **56**, 2602-2603 (1990).
15. V. A. Fedorov, Y. A. Kesler, E. G. Zhukov, *Inorg. Mater.*, **39**, S68-S88 (2003).
16. K. Ramesha, R. Seshadri, *Solid State Sci.*, **6**, 841-845 (2004).
17. D. Kim, A. Gedanken, Y. S. Tver'yanovich, D. W. Lee, B. K. Kim, *Mater. Lett.*, **60**, 2807-

2809 (2006).

18. I. Nakatani, H. Nose, K. Masumoto, *J. Phys. Chem. Solids* **39**, 743 (1978).
19. H. Mamiya, I. Nakatani, *Nanostructured Mater.* **12**, 859. (1999).
20. M. Sasaki, P. E. Jönsson, H. Takayama and H. Mamiya, *Phys. Rev. B* **71**, 104405 (2005).
21. C. Djurberg, J. Mattsson, P. Nordblad, *Europhys. Lett.* **29**, 163 (1995).
22. M. Respaud, J. M. Broto, H. Rakoto, A. R. Fert, L. Thomas, B. Barbara, M. Verelst, E. Snoeck, P. Lecante, A. Mosset, J. Osuna, T. Ould Ely, C. Amiens and B. Chaudret, *Phys. Rev. B* **57**, 2925 (1998).
23. P. P. Vaishnava, U. Senaratne, E. C. Buc, R. Naik, V. M. Naik, G. M. Tsoi and L. E. Wenger, *Phys. Rev. B* **76**, 024413 (2007).
24. W.-L. Lee, S. Watauchi, V. L. Miller, R. J. Cava and N. P. Ong, *Science* **303**, 1647 (2004).
25. K. Ramesha, R. Seshadri, *Solid State Sciences* **6**, 841 (2004).
26. M. L. Rao, M. Shamsuzzoha and A. Gupta, *J. Cryst. Growth* **306**, 321 (2007).
27. R. Chantrell, J. Popplewell, S. Charles, *IEEE Trans. Magn.* **14**, 975 (1978).
28. D. Rodic, B. Antic, R. Tellgren, H. Rundlof and J. Blanusa, *J. Magn. Magn. Mater.* **187**, 88 (1998).
29. D. Fiorani (Ed.), *Surface Effects in Magnetic Nanoparticles*, Springer, 2005.

## CHAPTER 4

### FIRST-PRINCIPLES CALCULATIONS ON CHROMIUM-BASED CHALCOSPINELS

Reproduced in part with permission from [Wang, Y.-H. A. *et al. Appl. Phys. Lett* **92**, 062507–062509 (2008).] Copyright [2008] American Institute of Physics. [Wang, Y.-H. A. *et al. Appl. Phys. Lett* **94**, 062515–062517 (2009).] Copyright [2009] American Institute of Physics.

First-principles calculations of the electronic structures of chalcogenide spinels with  $\text{Cd}_x\text{Cu}_{1-x}\text{Cr}_2\text{S}(\text{Se})_4$ ,  $\text{Cu}(\text{Cd})\text{Cr}_2\text{S}(\text{Se})_{4-x}$ ,  $\text{CuCr}_2\text{S}(\text{Se})_{4-x}\text{E}_x$  ( $\text{E}=\text{F}, \text{Cl}, \text{Br}$ ) and  $\text{CdCr}_2\text{S}(\text{Se})_{4-x}\text{D}_x$  ( $\text{D}=\text{N}, \text{P}, \text{As}$ ) predict half-metallic behavior over a range of concentrations. The magnetic moment is found to scale approximately linearly on adding or withdrawing electrons and varies between 5.0 and 6.0  $\mu_{\text{B}}/\text{f.u.}$

#### 4.1 Introduction

Magnetic materials with diverse electronic transport properties (metallic, semiconducting, insulating) and sufficiently high Curie temperature ( $T_C$ ) are needed for room temperature operation of spin-based electronic (spintronic) devices. In view of the high  $T_C$  requirement, the chromium based chalcospinels (chalcogenide-based spinel)  $\text{ACr}_2\text{X}_4$  ( $\text{A} = \text{Cu}, \text{Cd}, \text{Hg}, \text{Fe}, \text{Co}$ ;  $\text{X} = \text{S}, \text{Se}, \text{Te}$ ) are potentially attractive candidates. The compounds  $\text{CuCr}_2\text{S}_4$ ,  $\text{CuCr}_2\text{Se}_4$  and  $\text{CuCr}_2\text{Te}_4$  are metallic with Curie temperatures of 377 K, 430 K and 360 K, respectively.<sup>1-5</sup> Furthermore, a number of the Cr-based chalcospinels have generated renewed interest in recent years because of their unique magnetotransport and magnetodielectric properties. For example, the Cu-chromium chalcogenides exhibit unusual transport properties characterized by a large, temperature-dependent magnetoresistance.<sup>6</sup> Similarly,  $\text{CdCr}_2\text{S}_4$  and  $\text{HgCr}_2\text{S}_4$  display unusual time-dependent ferroelectric and colossal magnetocapacitance properties.<sup>7</sup> A dissipationless anomalous Hall current has also recently been observed in the ferromagnetic spinel  $\text{CuCr}_2\text{Se}_4$ .

$x\text{Br}_x$ .<sup>8</sup> These observations have provoked strong interest in these materials for possible spintronic applications.

The chromium-based compounds are *normal* spinels that have a face-centered cubic lattice and belong to the centrosymmetric space group  $Fd3m$ . A basic structural component of the chalcospinels is an anion bonded to one  $A$  cation and three Cr ions. The nominally divalent metal ions  $A$  occupy the tetrahedral sites (1/8 filled by  $A$ ), while the trivalent Cr ions occupy the octahedral sites (1/2 filled by Cr). The positions of the cations are fixed by the symmetry of the structure, but the anion positions are variable and are specified by the parameter  $u$ . A local structural deformation induced by the cation-anion interaction is observed in these materials and is characterized by a small deviation of the anion parameter  $u$  from the ideal value of 0.375. These distortions along with cation valence play an important role in determining the properties of these materials.

Although the properties of the chalcospinels have been the subject of recent experimental studies, their electronic structure has received less attention, due at least in part to their rather complicated crystal structure. The electronic structure of  $\text{CuCr}_2\text{X}_4$  ( $\text{X} = \text{S}, \text{Se}, \text{Te}$ ) chalcogenides was discussed in the past,<sup>2,3</sup> but until recently no detailed band structure calculations were reported. Band structure calculations suggest that a number of chalcospinels are highly spin-polarized.<sup>7-10</sup> Indeed, complete spin polarization - so called half-metallic (HM) materials - where there is a gap in one spin band at the Fermi level and no gap in the other spin band have been predicted in the  $\text{Fe}_{1-x}\text{Cu}_x\text{Cr}_2\text{S}_4$  system.<sup>7</sup> Shanthi *et al.* have reported the band structure of  $\text{CdCr}_2\text{S}_4$  and  $\text{CdCr}_2\text{Se}_4$  based on *ab initio* calculations, for both the nonmagnetic and the ferromagnetic states.<sup>8</sup> Their calculations predict  $\text{CdCr}_2\text{S}_4$  to be a ferromagnetic insulator and  $\text{CdCr}_2\text{Se}_4$  to have a ferromagnetic semi-metallic ground state with very low density of states at

the Fermi energy and a nearly gapped structure. Strong exchange splitting in both the compounds suggests the tantalizing possibility of realizing a half-metallic ferromagnetic state in the Cr-chalcospinels. In this chapter, systematic spin-polarized electronic calculations of quaternary or anion vacancies chalcospinels are performed.

## 4.2 Simulation Package and Parameters

The Vienna *ab initio* simulation package (VASP) is used,<sup>11</sup> and it is based on density functional theory with generalized gradient approximation (GGA),<sup>12</sup> for the exchange correlation potential and projector augmented wave (PAW) based pseudopotentials.<sup>13</sup> The detail description of VASP is provided in section 2.10. The largest chalcospinel unit cell used in this work contains 56 atoms, which includes 32 anions, 8 *A*-site Cd/Cu cations, and 16 *B*-site Cr cations. The Cd/Cu ions occupy the tetrahedral sites, while the octahedral site is occupied exclusively by Cr. Because of the clear octahedral preference for the Cr<sup>+3</sup> ions a *normal* spinel structure is adopted for all these compounds. Using a 56 atom supercell for the calculations involves *A*-site Cd substitution in 1/8<sup>th</sup> increments of  $x$ . No significant change in the results is observed when arbitrary changes are made in the choices of the *A* sites for making the Cd substitutions. For  $x$  increments of 1/4<sup>th</sup>, we have used a 28 atom supercell to simplify the calculations (see Table 4.1). As a test, we calculated the end cases ( $x = 0$  and 1) with 14, 28 and 56 atoms and verified that the calculated DOS per formula unit is essentially independent of the cell size. For the anion substituted calculations were used a 14 atom cell in which the anion-sites (S or Se) were substituted by F, Cl, Br, N, P and As. We present results for substituting 1/8<sup>th</sup> and 1/4<sup>th</sup> of the anion sites for the entire series of *A*-site Cu and Cd-based chalcospinels. The results presented here do not depend on arbitrary changes in the choice of the anion site(s) for making the substitution(s).

### 4.3 Results of Tetrahedral Site Substitutions

As a first step the structures are fully relaxed in shape and volume to determine the lowest energy configuration. The calculated relaxed positions of the S/Se away from the ideal  $u$  value of 0.375 are in very good agreement with the experimentally determined values of  $u$  (Table I). Figures 4.1a and 4.1b display the calculated total densities of states (DOS) of the majority and minority spin bands for  $\text{CuCr}_2\text{S}_4$  and  $\text{CdCr}_2\text{S}_4$ , respectively. The partial DOS of the Cu/Cd  $d$ , Cr

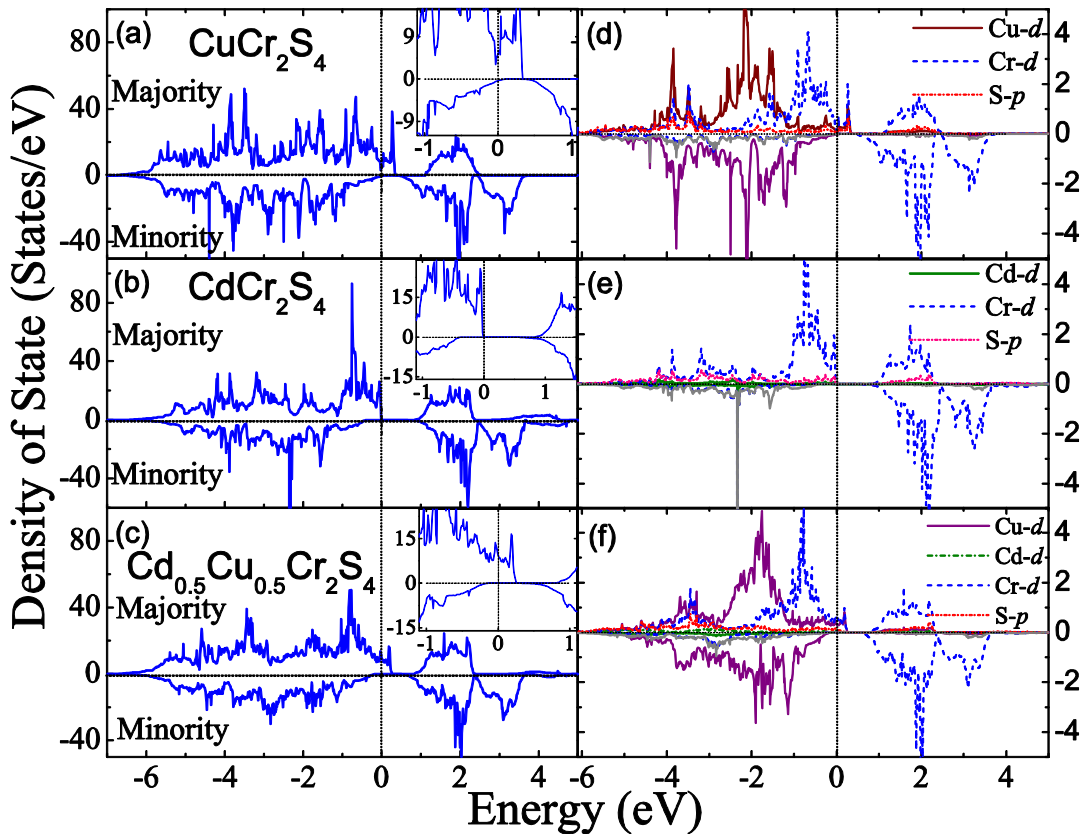


**Figure 4.1** Calculated total and individual Cu  $d$ , Cr  $d$  and S  $p$  density of electronic states (DOS) of the  $\text{Cd}_x\text{Cu}_{1-x}\text{Cr}_2\text{S}_4$  system for both the majority and minority spin bands; (a) and (d) are for  $\text{CuCr}_2\text{S}_4$ ; (b) and (e) are for  $\text{CdCr}_2\text{S}_4$ ; and (c) and (f) are for  $\text{Cd}_{0.75}\text{Cu}_{0.25}\text{Cr}_2\text{S}_4$ .

$d$  and S  $p$  for the two systems are shown in Figs. 4.1d and 4.1e. Similarly, the calculated DOS for  $\text{CuCr}_2\text{Se}_4$  and  $\text{CdCr}_2\text{Se}_4$  are shown in Fig. 4.2a and 4.2b, respectively, and the partial DOS of Cu/Cd  $d$ , Cr  $d$  and Se  $p$  shown in Fig. 4.2d and 4.2e. It is apparent that for all cases the total DOS

for energies around the Fermi level originate almost completely from the Cu/Cd and Cr  $d$  bands and S/Se  $p$  bands for both spin bands. These calculations are in qualitative agreement with previously reported results.<sup>7-10</sup>

Our calculations for  $\text{CdCr}_2\text{Se}_4$  differ in an important detail, however, from those reported in Refs. 8 and 9. Experiment shows the material to be a direct band gap semiconductor with a gap

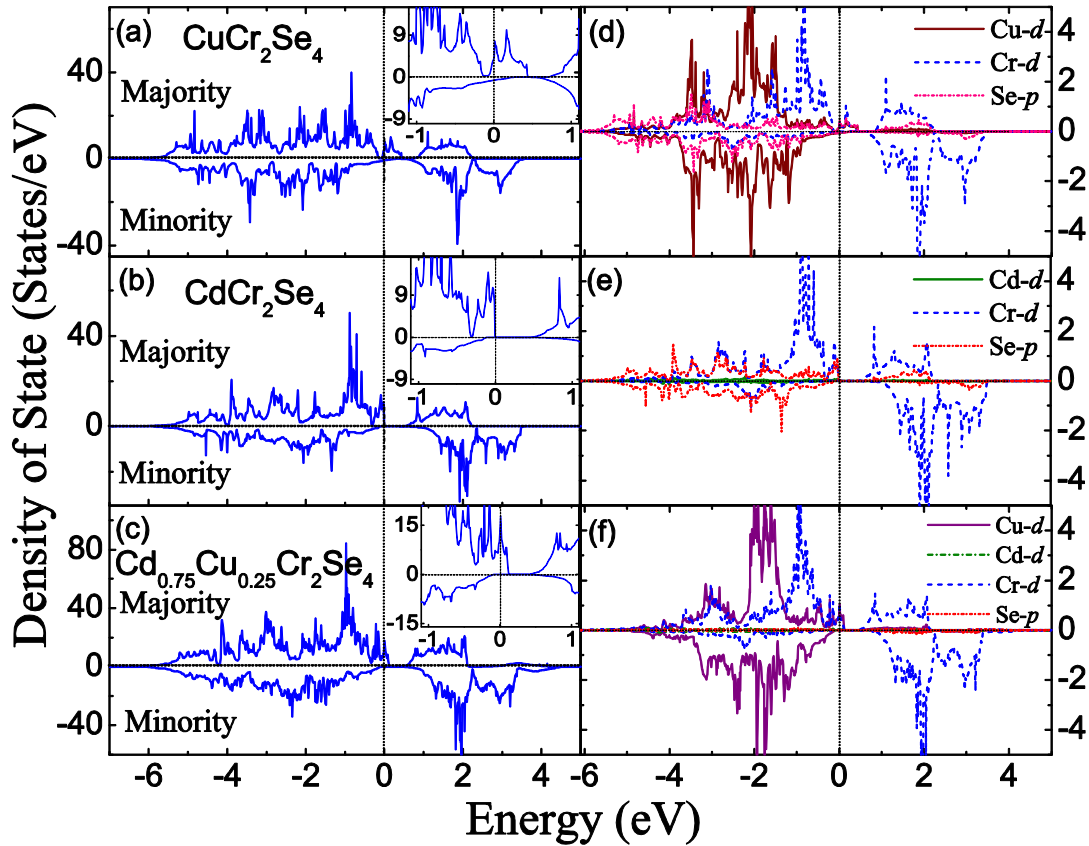


**Figure 4.2** Calculated total and individual Cu  $d$ , Cr  $d$  and Se  $p$  density of electronic states (DOS) of  $\text{Cd}_x\text{Cu}_{1-x}\text{Cr}_2\text{Se}_4$  system for both the majority and minority spin bands; (a) and (d) are for  $\text{CuCr}_2\text{Se}_4$ ; (b) and (e) are for  $\text{CdCr}_2\text{Se}_4$ ; and (c) and (f) are for  $\text{Cd}_{0.5}\text{Cu}_{0.5}\text{Cr}_2\text{Se}_4$ .

of  $1.3 \text{ eV}^{14}$ . Our calculations yield a direct band gap semiconductor with a somewhat smaller gap ( $0.4 \text{ eV}$ ). The calculations of Ref. 8 and 9 yield a semi-metallic ground state. The disagreement with experiment was ascribed in both cases to inadequacies of density functional theory (DFT).

Although the tendency of DFT to underestimate band gaps is well documented, from the calculated data the band gap error may be less than originally believed. Possible reasons for the disagreement between our calculations and those cited, is the use of the atomic sphere approximation in Ref. 8 and the use of ultra-soft pseudo-potentials in Ref. 9. The atomic sphere approximation is severe for spinel structure materials. Ultra-soft pseudopotentials may not be as reliable for transition metal ions as the Projector Augmented Wave (PAW) pseudopotentials used the calculations reported here.

In addition to predicting the correct ground state structural properties for  $\text{CdCr}_2\text{S}_4$  and  $\text{CdCr}_2\text{Se}_4$ , the calculated magnetic moments match very well with the experimental values reported for these systems (Table 4.1). For instance, the calculated magnetic moment of both  $\text{CdCr}_2\text{S}_4$  and  $\text{CdCr}_2\text{Se}_4$  is  $6.0 \mu_B$  /formula unit, which would be expected for the  $t_{2g}^3$  ( $S=3/2$ ) electron configuration of  $\text{Cr}^{3+}$  in octahedral coordination. This is in excellent agreement with the experimentally reported values of 6.0 and  $5.98\mu_B$ / formula unit, respectively, for single crystal samples.<sup>6,15</sup> It should be noted that the experimentally reported saturation moments values for polycrystalline samples are generally lower, particular for those with stoichiometry deviations.<sup>16</sup>

For the Cu chalcogenides, the DOS at the Fermi level ( $E_F$ ) is consistent with metallic behavior and suggests a high degree of spin polarization as shown in Figs. 4.1a and 4.2a. However, they cannot be considered to be true half-metals because of the small but finite density of minority states at  $E_F$ . The results for  $\text{CuCr}_2\text{Se}_4$  are also in good agreement with those reported recently.<sup>10</sup> Our calculated moments for  $\text{CuCr}_2\text{S}_4$  and  $\text{CuCr}_2\text{Se}_4$  are 5.0 and  $5.1 \mu_B$  /formula unit, respectively, again close to the experimentally reported values of 4.85 and  $5.2 \mu_B$  /formula unit, respectively. While the value for  $\text{CuCr}_2\text{S}_4$  is for a polycrystalline sample,<sup>17</sup> that for  $\text{CuCr}_2\text{Se}_4$  is for a single crystal.<sup>18</sup> Unlike the Cd chalcogenides, for which the magnetization arises almost

exclusively from the  $B$  site Cr, the magnetic moment of the  $A$  site Cu  $3d$  state in the Cu chalcogenides is finite and aligned antiparallel to that of Cr. This results in a reduction of the total moment for the latter.

The band structure of the quaternary systems  $\text{Cd}_x\text{Cu}_{1-x}\text{Cr}_2\text{Se}_4$  and  $\text{Cd}_x\text{Cu}_{1-x}\text{Cr}_2\text{S}_4$  have also been performed. These calculations employed supercells consisting of 28 and 56 atoms, as mentioned previously. While the unmixed cases (end members) are metallic ( $x = 0$ ) and semiconducting ( $x = 1$ ), respectively, consistent with experimental results, we find that half-metallicity can be induced in both systems for a range of Cd-Cu compositions. Specifically, for

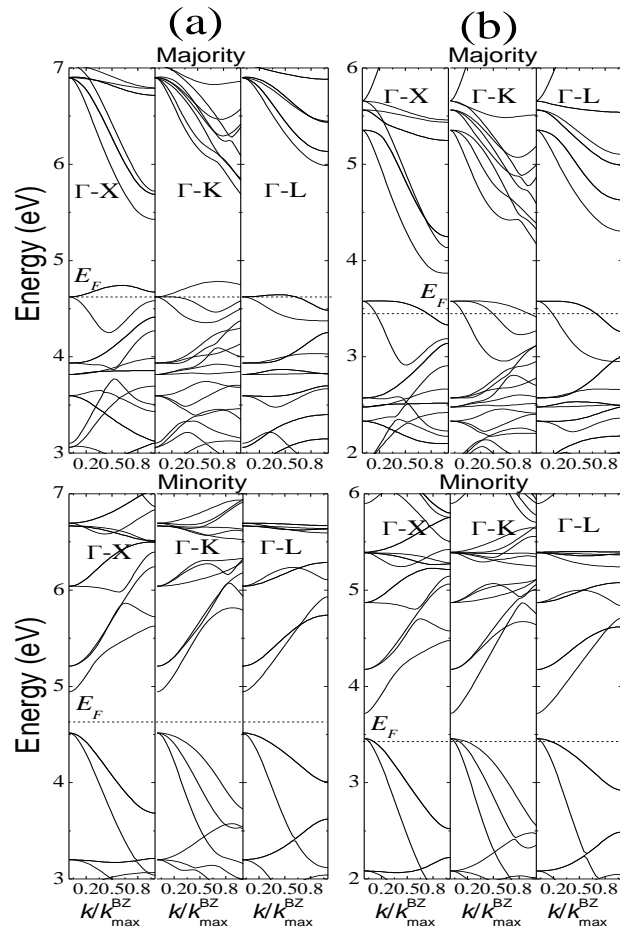


**Figure 4.3** Majority and minority energy bands near the Fermi energy (dashed line) along  $\Gamma$ -X,  $\Gamma$ -K and  $\Gamma$ -L directions for (a)  $\text{Cd}_{0.5}\text{Cu}_{0.5}\text{Cr}_2\text{S}_4$  and (b)  $\text{Cd}_{0.5}\text{Cu}_{0.5}\text{Cr}_2\text{Se}_4$ .

the  $\text{Cd}_x\text{Cu}_{1-x}\text{Cr}_2\text{S}_4$  system, while  $x = 0.125$  is predicted to be metallic, the compositions with  $x = 0.25, 0.375, 0.5$  (Fig. 4.1c),  $0.625, 0.75$  and  $0.875$  are predicted to be half-metallic, with the minority gap at the Fermi energy increasing with increasing cadmium concentration. For  $\text{Cd}_x\text{Cu}_{1-x}\text{Cr}_2\text{Se}_4$  we observe that  $x = 0.125, 0.25, 0.375$  and  $0.5$  show metallic behavior, while  $x = 0.625, 0.75$  (Fig. 4.2c) and  $0.875$  are half-metallic. Similar to the case of  $\text{Cd}_x\text{Cu}_{1-x}\text{Cr}_2\text{S}_4$  system, the energy gap increases with increasing cadmium concentration. As an example, Fig. 4.3a shows the energy bands near the Fermi energy for  $\text{Cd}_{0.5}\text{Cu}_{0.5}\text{Cr}_2\text{S}_4$ , demonstrating that the Fermi energy lies in a gap for the minority channel, while for the same composition ratio in case of  $\text{Cd}_{0.5}\text{Cu}_{0.5}\text{Cr}_2\text{Se}_4$  (Fig. 4.3b) the Fermi level still crosses the minority bands being close to the bottom of the gap. Again, further increase of Cd concentration to  $0.625$  and above in  $\text{Cd}_x\text{Cu}_{1-x}\text{Cr}_2\text{Se}_4$  moves the Fermi level up into the gap, thereby tuning the structure to half-metallic state. This picture is corroborated by a systematic analysis of the band structures of both  $\text{Cd}_x\text{Cu}_{1-x}\text{Cr}_2\text{Se}_4$  and  $\text{Cd}_x\text{Cu}_{1-x}\text{Cr}_2\text{S}_4$  which clearly show an increase of minority gap combined with the shift of the Fermi level as a function of  $x$ .

Among the two quaternary systems that we have investigated so far, the  $\text{Cd}_{0.25}\text{Cu}_{0.75}\text{Cr}_2\text{S}_4$  tends to favor formation of a half-metallic state at lower cadmium concentrations. Since the experimentally determined ferromagnetic Curie temperatures of the sulfospinel end members  $\text{CdCr}_2\text{S}_4$  and  $\text{CuCr}_2\text{S}_4$  are  $85$  and  $377$  K, respectively, it may be possible for the quaternary system with low Cd concentrations to be half-metallic at room temperature.

The magnetic moment per formula unit as a function of composition for both of the quaternary systems  $\text{Cd}_x\text{Cu}_{1-x}\text{Cr}_2\text{S}_4$  and  $\text{Cd}_x\text{Cu}_{1-x}\text{Cr}_2\text{Se}_4$  have been calculated as well. The calculated values are listed in Table I. The moment is found to increase and scale linearly with increasing Cd concentration. For completeness, we have performed similar calculations on the

analogous Te compounds. Unlike the Se and S cases, no half-metallic behavior was observed for  $\text{Cd}_x\text{Cu}_{1-x}\text{Cr}_2\text{Te}_4$ . The end members,  $\text{CdCr}_2\text{Te}_4$  and  $\text{CuCr}_2\text{Te}_4$  both show metallic behavior.

**Table 4.1** Calculated structural and magnetic properties of relaxed  $\text{Cd}_x\text{Cu}_{1-x}\text{Cr}_2\text{Se}_4$  and  $\text{Cd}_x\text{Cu}_{1-x}\text{Cr}_2\text{S}_4$  supercells, along with comparison with the experimental data: lattice parameters, u parameters, and low temperature magnetic moment.

Supercell	Lattice parameter (Å)		“u” parameter		Magnetic moment		Number of electrons	
	Exp.	Cal.	Exp.	Cal.	Exp.	Cal.	$N^\uparrow$	$N^\downarrow$
$\text{CuCr}_2\text{Se}_4$	10.337	10.374	0.382	0.383	5.20	5.10	26.05	20.95
$\text{Cd}_{0.25}\text{Cu}_{0.75}\text{Cr}_2\text{Se}_4$	-	10.497	-	0.384	-	5.32	26.285	20.965
$\text{Cd}_{0.5}\text{Cu}_{0.5}\text{Cr}_2\text{Se}_4$	-	10.557	-	0.390	-	5.50	26.5	21.00
$\text{Cd}_{0.625}\text{Cu}_{0.375}\text{Cr}_2\text{Se}_4$	-	10.662	-	0.390	-	5.63	26.63	21.00
$\text{Cd}_{0.75}\text{Cu}_{0.25}\text{Cr}_2\text{Se}_4$	-	10.722	-	0.389	-	5.75	26.75	21.00
$\text{Cd}_{0.875}\text{Cu}_{0.125}\text{Cr}_2\text{Se}_4$	-	10.786	-	0.391	-	5.87(5)	26.875	21.00
$\text{CdCr}_2\text{Se}_4$	10.721	10.839	0.390	0.390	5.98	6.00	27.00	21.00
$\text{CuCr}_2\text{S}_4$	9.814	9.812	0.383	0.383	4.85	5.00	26.005	20.995
$\text{Cd}_{0.125}\text{Cu}_{0.875}\text{Cr}_2\text{S}_4$	-	9.873	-	0.383	-	5.13	26.127	20.997
$\text{Cd}_{0.25}\text{Cu}_{0.75}\text{Cr}_2\text{S}_4$	-	9.946	-	0.386	-	5.25	26.25	21.00
$\text{Cd}_{0.5}\text{Cu}_{0.5}\text{Cr}_2\text{S}_4$	-	10.050	-	0.392	-	5.50	26.5	21.00
$\text{Cd}_{0.75}\text{Cu}_{0.25}\text{Cr}_2\text{S}_4$	-	10.212	-	0.389	-	5.75	26.75	21.00
$\text{Cd}_{0.875}\text{Cu}_{0.125}\text{Cr}_2\text{S}_4$	-	10.223	-	0.391	-	5.87(5)	26.875	21.00
$\text{CdCr}_2\text{S}_4$	10.207	10.295	0.390	0.391	6.00	6.00	27.0	21.00

#### 4.4 Results of Anion Site Substitutions

Again, the structures both in shape and volume are relaxed completely to determine the lowest energy configuration. To investigate the band structure of  $\text{CuCr}_2\text{S}(\text{Se})_{4-x}\text{E}_x$  ( $\text{E}=\text{F}, \text{Cl}, \text{Br}$ ),  $\text{Cu}(\text{Cd})\text{Cr}_2\text{S}(\text{Se})_{4-x}$  and  $\text{CdCr}_2\text{S}(\text{Se})_{4-x}\text{D}_x$  ( $\text{D}=\text{N}, \text{P}, \text{As}$ ), we have assumed a normal spinel structure over the entire composition range and used 14-atom supercells as mentioned earlier.

According to the calculated results, the electronic properties at the Fermi level are strongly dependent on the amount of anionic substitution. The sulfide compounds, except for the  $\text{CdCr}_2\text{S}_{3.5}\text{As}_{0.5}$  and  $\text{CdCr}_2\text{S}_{3.5}$ , are half-metallic (shown underlined in Table I) for  $x = 0.5$  composition. As an example, density of states (DOS) are shown in Figs. 4.4a, 4.4b and 4.4c for  $\text{CuCr}_2\text{S}_{3.5}\text{Br}_{0.5}$ ,  $\text{CuCr}_2\text{S}_{3.5}$  and  $\text{CdCr}_2\text{S}_{3.5}\text{P}_{0.5}$ , respectively. There is a clear gap appearing around  $E_F$  for all cases. In addition, for the composition with  $x = 1$ , namely  $\text{CuCr}_2\text{S}_3\text{F}$ ,  $\text{CdCr}_2\text{S}_3\text{N}$  and  $\text{CdCr}_2\text{S}_3$  also show a half-metal state. At the same time,  $\text{CuCr}_2\text{S}_3\text{Cl}$  and  $\text{CuCr}_2\text{S}_3\text{Br}$  are semiconductors (shown in Table 4.2), while  $\text{CdCr}_2\text{S}_3\text{P}$  and  $\text{CdCr}_2\text{S}_3\text{As}$  are metals.

However, the behavior of the selenides significantly differs from the sulfides, in being more

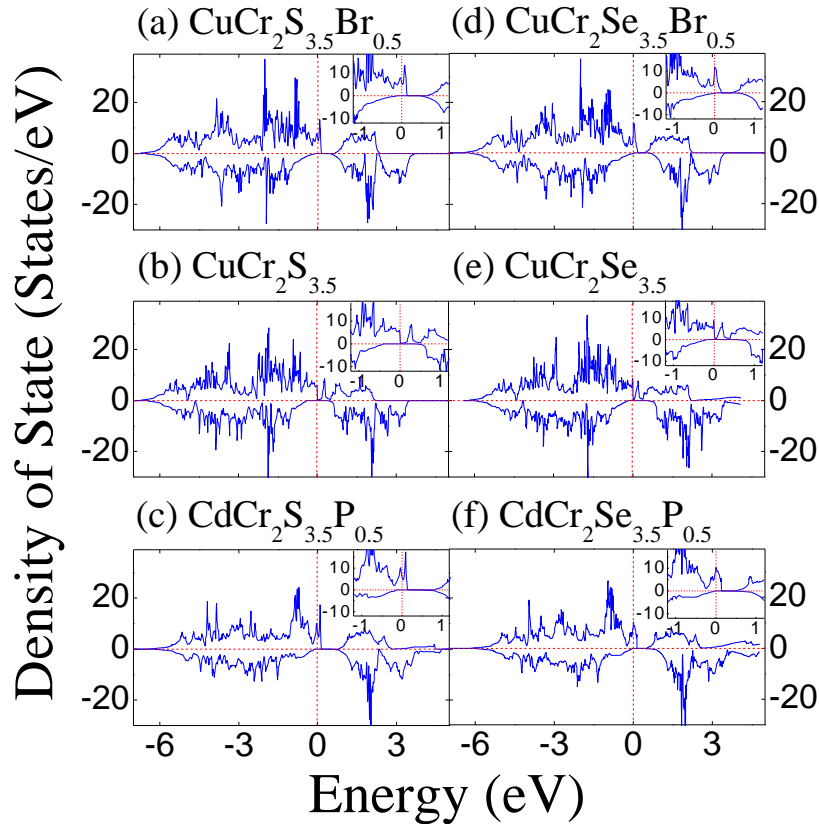


**Figure 4.4** Calculated total density of electronic states (DOS) of the  $\text{CuCr}_2\text{S}(\text{Se})_{3.5}\text{Br}_{0.5}$ ,  $\text{CuCr}_2\text{S}(\text{Se})_{3.5}$ , and  $\text{CdCr}_2\text{S}(\text{Se})_{3.5}\text{P}_{0.5}$  systems for both the majority and minority spin bands.

difficult to tune into half-metal. For the composition with  $x = 0.5$ ,  $\text{CuCr}_2\text{Se}_{3.5}$  (Fig. 4.4e),  $\text{CdCr}_2\text{Se}_{3.5}\text{N}_{0.5}$  and  $\text{CdCr}_2\text{Se}_{3.5}\text{P}_{0.5}$  (Fig. 4.4f) show half-metallic behavior while the others are metals ( $\text{CdCr}_2\text{Se}_{3.5}$  is a semiconductor). In Fig. 4.4d, we show the DOS for  $\text{CuCr}_2\text{Se}_{3.5}\text{Br}_{0.5}$ . It has a non-vanishing DOS in the minority band at the Fermi level so it is predicted to be a metal instead of a half-metal. For the composition with  $x = 1$ , only  $\text{CuCr}_2\text{Se}_3\text{Cl}$ ,  $\text{CuCr}_2\text{Se}_3\text{Br}$  and  $\text{CdCr}_2\text{Se}_3$  are predicted to be half-metals. In addition, we explored the composition with  $x = 0.25$  (one anion substituted) and 0.75 (three anions substituted). For these calculations a 28 atom supercell was used. In the case  $x = 0.25$ , fourteen compounds were investigated. Out of these, eleven compositions still showed half-metallic character while  $\text{CuCr}_2\text{Se}_{3.75}\text{E}_{0.25}$ , ( $\text{E} = \text{F}, \text{Cl}, \text{Br}$ ) did not. Compared to the case of  $x = 0.25$ , the case with composition  $x = 0.75$  show a more complicated behavior. For example,  $\text{CdCr}_2\text{S}_{3.25}\text{P}_{0.75}$  has lower energy and displays metallic behavior when three phosphorus atoms are placed in the same layer. However, configurations with different placement of phosphorus atoms are about 0.25 eV higher in energy and predicted to be half-metallic. On the contrary,  $\text{CuCr}_2\text{S}_{3.25}\text{Cl}_{0.75}$  results in the lowest energy when the three Cl at placed in different layers. In Fig. 4.5, we summarize results of ferromagnetic metal, ferromagnetic half-metal and ferromagnetic semiconductor as function of number of valence electrons per formula unit for all the different anion substitutions. It is clear that the sulfur-based systems can be induced to half-metallic state over a wider range of substitutions as compared to the selenium-based systems.

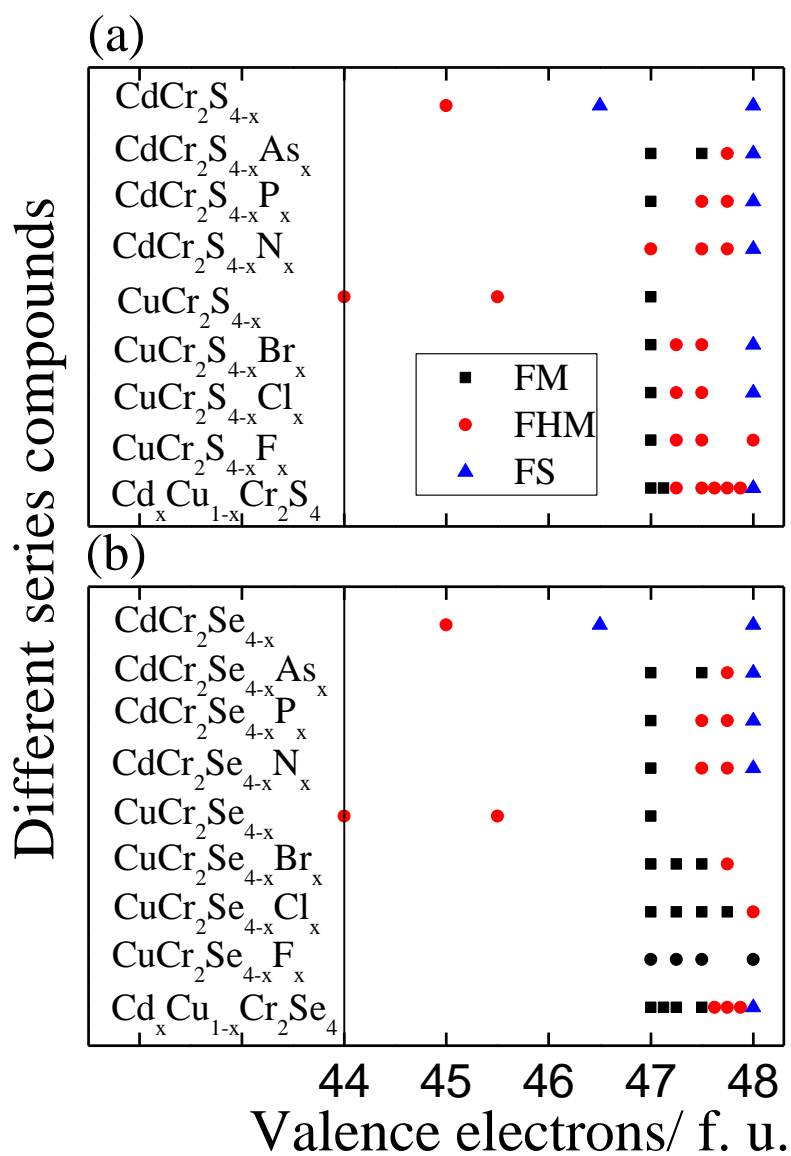


**Figure 4.5** The calculated range of ferromagnetic metal (FM), ferromagnetic half-metal (FHM) and ferromagnetic semiconductor (FS) as a function of total valence electrons per formula unit for the different anion substituted systems.

In addition to total energy and DOS calculations, the energy band in the symmetry directions,  $\Gamma$ -X,  $\Gamma$ -K and  $\Gamma$ -L are calculated. Figures 4.6a and 4.6b represent the majority and minority energy bands of  $\text{CuCr}_2\text{S}_4$  and  $\text{CuCr}_2\text{S}_{3.5}\text{Br}_{0.5}$ , respectively. Similarly, Figs. 4.7a and 4.7b show the energy bands of  $\text{CdCr}_2\text{S}_{3.5}\text{P}_{0.5}$  and  $\text{CdCr}_2\text{S}_4$ , respectively. Interestingly, the majority energy band at the Fermi level changes from bending down as one leaves the  $\Gamma$  point, to being

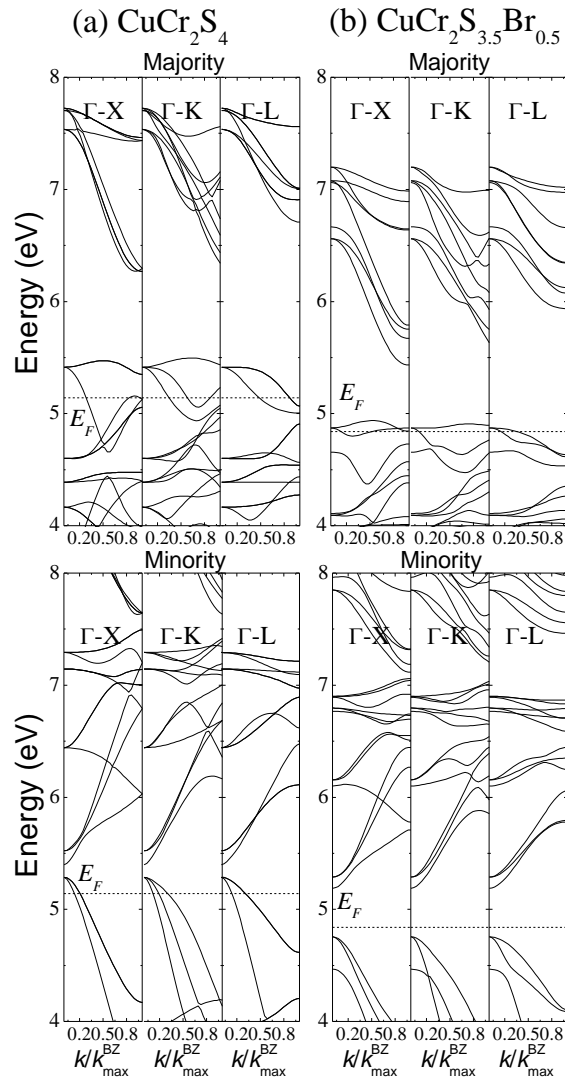


**Figure 4.6** Majority and minority energy bands near the Fermi energy (dashed line) along  $\Gamma$ -X,  $\Gamma$ -K and  $\Gamma$ -L directions for (a)  $\text{CuCr}_2\text{S}_4$  and (b)  $\text{CuCr}_2\text{S}_{3.5}\text{Br}_{0.5}$ .

approximately flat or to have higher energy away from  $\Gamma$  point. Similar behavior is seen in the selenium systems.

The magnetic moment per formula unit for all compounds is calculated and the values are listed in Table 4.2. In the case of  $A = \text{Cu}$  the moment is found to increase and scale approximately linearly with increasing  $x$  concentration. While for  $A = \text{Cd}$ , the moment decreases and scales approximately linearly with increasing  $x$  concentration.

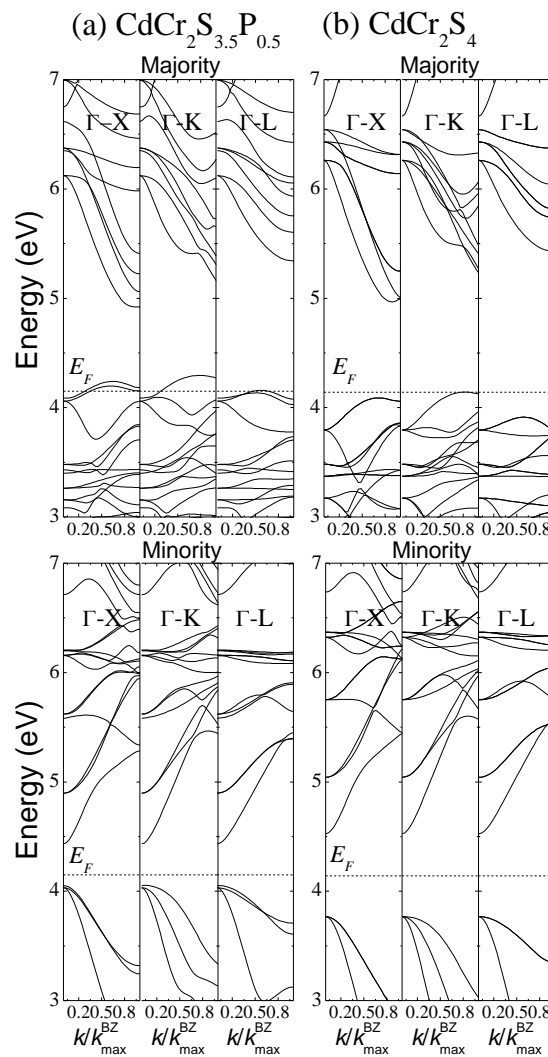


**Figure 4.7** Majority and minority energy bands near the Fermi energy (dashed line) along  $\Gamma$ -X,  $\Gamma$ -K and  $\Gamma$ -L directions for (a)  $\text{CdCr}_2\text{S}_{3.5}\text{P}_{0.5}$  and (b)  $\text{CdCr}_2\text{S}_4$ .

In conclusion of this chapter, the magnetotransport properties of A site substituted quaternary systems,  $\text{Cd}_x\text{Cu}_{1-x}\text{Cr}_2\text{Se}_4$  and  $\text{Cd}_x\text{Cu}_{1-x}\text{Cr}_2\text{S}_4$ , can be tuned by varying the Cu/Cd composition, with half-metallic behavior being predicted for a range of Cd concentration. The calculated results also indicate that for both the S and Se-based quaternary chalcospinels the magnetic moment scales approximately linearly with  $x$  until the system becomes half-metallic, at

**Table 4.2** Calculated structural and magnetic properties of relaxed  $\text{CuCr}_2\text{S}(\text{Se})_{4-x}\text{E}_x$  (E=F, Cl, Br),  $\text{Cu}(\text{Cd})\text{Cr}_2\text{S}(\text{Se})_{4-x}$  and  $\text{CdCr}_2\text{S}(\text{Se})_{4-x}\text{D}_x$  (D=N, P, As) supercells, along with comparison with the experimental data: lattice parameters, u parameters, and low temperature magnetic moment.

Supercell	Lattice parameter (Å)		“u” parameter		Magnetic moment ( $\mu_B/\text{f.u.}$ )		Total spin electrons	
	Exp.	Cal.	Exp.	Cal.	Exp.	Cal.	N $\uparrow$	N $\downarrow$
$\text{CuCr}_2\text{S}_4$	9.814	9.812	0.383	0.383	4.85	5.01	26.00(5)	20.99(5)
$\text{CuCr}_2\text{S}_{3.5}\text{F}_{0.5}$	-	9.862	-	0.387	-	5.50	26.5	21.0
$\text{CuCr}_2\text{S}_3\text{F}$	-	9.917	-	0.382	-	6.00	27.0	21.0
$\text{CuCr}_2\text{S}_{3.5}\text{Cl}_{0.5}$	-	9.923	-	0.387	-	5.50	26.5	21.0
$\text{CuCr}_2\text{S}_3\text{Cl}$	-	10.026	-	0.387	-	6.00	27.0	21.0
$\text{CuCr}_2\text{S}_{3.5}\text{Br}_{0.5}$	-	9.969	-	0.390	-	5.50	26.5	21.0
$\text{CuCr}_2\text{S}_3\text{Br}$	-	10.107	-	0.392	-	6.00	27.0	21.0
$\text{CuCr}_2\text{S}_{3.5}$	-	9.955	-	0.384	-	6.00	25.0	19.0
$\text{CuCr}_2\text{Se}_4$	10.337	10.374	0.382	0.383	5.20	5.10	26.05	20.95
$\text{CuCr}_2\text{Se}_{3.5}\text{F}_{0.5}$	-	10.394	-	0.384	-	5.53	26.51(5)	20.98(5)
$\text{CuCr}_2\text{Se}_3\text{F}$	-	10.476	-	0.380	-	6.01(5)	27.01	20.99(5)
$\text{CuCr}_2\text{Se}_{3.5}\text{Cl}_{0.5}$	-	10.415	-	0.384	-	5.50(3)	26.50(3)	21.0
$\text{CuCr}_2\text{Se}_3\text{Cl}$	-	10.538	-	0.383	-	6.00	27.0	21.0
$\text{CuCr}_2\text{Se}_{3.5}\text{Br}_{0.5}$	-	10.482	-	0.387	-	5.50(7)	26.50(7)	21.0
$\text{CuCr}_2\text{Se}_3\text{Br}$	-	10.579	-	0.387	5.99	6.00	27.0	21.0
$\text{CuCr}_2\text{Se}_{3.5}$	-	10.520	-	0.385	-	6.00	25.0	19.0
$\text{CdCr}_2\text{S}_4$	10.207	10.295	0.390	0.390	6.0	6.00	27.0	21.0
$\text{CdCr}_2\text{S}_{3.5}\text{N}_{0.5}$	-	10.064	-	0.380	-	5.50	26.5	21.0
$\text{CdCr}_2\text{S}_3\text{N}$	-	9.751	-	0.376	-	5.00	26.0	21.0
$\text{CdCr}_2\text{S}_{3.5}\text{P}_{0.5}$	-	10.303	-	0.391	-	5.50	26.5	21.0
$\text{CdCr}_2\text{S}_3\text{P}$	-	10.276	-	0.392	-	5.00	26.0	21.0
$\text{CdCr}_2\text{S}_{3.5}\text{As}_{0.5}$	-	10.346	-	0.392	-	5.50(5)	26.50(5)	21.0
$\text{CdCr}_2\text{S}_3\text{As}$	-	10.385	-	0.395	-	5.02	26.01	20.99
$\text{CdCr}_2\text{S}_3$	-	9.721	-	0.384	-	6.00	24.0	18.0
$\text{CdCr}_2\text{Se}_4$	10.721	10.839	0.390	0.390	5.98	6.00	27.0	21.0
$\text{CdCr}_2\text{Se}_{3.5}\text{N}_{0.5}$	-	10.519	-	0.380	-	5.50	26.5	21.0
$\text{CdCr}_2\text{Se}_3\text{N}$	-	10.098	-	0.381	-	5.02	26.01	20.99
$\text{CdCr}_2\text{Se}_{3.5}\text{P}_{0.5}$	-	10.768	-	0.387	-	5.50	26.5	21.0
$\text{CdCr}_2\text{Se}_3\text{P}$	-	10.670	-	0.387	-	5.06	26.03	20.97
$\text{CdCr}_2\text{Se}_{3.5}\text{As}_{0.5}$	-	10.827	-	0.390	-	5.50(5)	26.50(5)	21.0
$\text{CdCr}_2\text{S}_3\text{As}$	-	10.794	-	0.391	-	5.10	26.05	20.95
$\text{CdCr}_2\text{Se}_3$	-	10.173	-	0.381	-	6.00	24.0	18.0

which point it scales perfectly linearly with  $x$ . Similarly, for anion substitutions and vacancies,  $\text{CuCr}_2\text{S}(\text{Se})_{4-x}\text{E}_x$  ( $\text{E}=\text{F}, \text{Cl}, \text{Br}$ ),  $\text{Cu}(\text{Cd})\text{Cr}_2\text{S}(\text{Se})_{4-x}$  and  $\text{CdCr}_2\text{S}(\text{Se})_{4-x}\text{D}_x$  ( $\text{D}=\text{N}, \text{P}, \text{As}$ ), a wide range of possible half-metal compositions are predicted, which can be tuned from ferromagnetic metals to ferromagnetic semiconductors. The magnetic moment scales approximately linearly with anion substitution concentration.

#### 4.5 References

1. F. K. Lotgering, *Solid State Commun.* **2**, 55 (1964); F. K. Lotgering in *Proceedings of International Conference on Magnetism*, Nottingham, 1964 (The Institute of Physics and the Physical Society, London, 1965), p. 533.
2. P. K. Baltzer, H. W. Lehmann, and M. Robbins, *Phys. Rev. Lett.* **15**, 493 (1965); P. K. Baltzer, P. J. Wojtowicz, M. Robbins, and E. Lopatin, *Phys. Rev.* **151**, 367 (1966).
3. J. B. Goodenough, *Solid State Commun.* **5**, 577 (1967); J. B. Goodenough, *J. Phys. Chem. Solids* **30**, 261 (1969).
4. K. G. Nikiforov, *Prog. Cryst. Growth and Charact. of Mat.* **39**, 1 (1999); Landolt-Börnstein, *Magnetic and Other Properties of Oxides and Related Compounds: Vol. III/4b*, Springer, 1970.
5. A. P. Ramirez, R. J. Cava, and J. Krajewski, *Nature* **386**, 156 (1997).
6. J. Hemberger, P. Lunkenheimer, R. Fichtl, H.-A. Krug von Nidda, V. Tsurkan, A. Loidl, *Nature* **434**, 364 (2005); S. Weber, P. Lunkenheimer, R. Fichtl, J. Hemberger, V. Tsurkan, and A. Loidl, *Phys. Rev. Lett.* **96**, 157202 (2006).
7. M. S. Park, S. K. Kwon, S. J. Youn, and B. I. Min, *Phys. Rev. B* **59**, 10018 (1999).
8. S. Shanthi, P. Mahadevan, and D. D. Sarma, *J. Solid State Chem.* **155**, 198 (2000).
9. G. Kioseglou, A.T. Hanbicki, J. M. Sullivan, O.M.J. Van't Erve, C.H. Li, S.C. Erwin, R. Mallory, M. Yasar, A. Petrou and B.T. Jonker, *Nature Materials* **3**, 799 (2004).
10. K. Ramesha and R. Seshadri, *Solid State Sci.* **6**, 841 (2004).
11. G. Kresse and J. Hafner, *Phys. Rev. B* **47**, 558 (1993); G. Kresse and J. Hafner, *Phys. Rev. B* **49**, 14251 (1994); G. Kresse and J. Furthmüller, *Comput. Mat. Sci.* **6**, 15 (1996); G. Kresse and J. Furthmüller, *Phys. Rev. B* **54**, 11169 (1996).

12. J. P. Perdew, in *Electronic Structure of Solids '91*, edited by P. Ziesche and H. Eschrig (Akademie Verlag, Berlin, 1991), p. 11.
13. P. E. Blöchl, Phys. Rev. B **50**, 17953 (1994); G. Kresse and J. Joubert, Phys. Rev. B **59**, 1758 (1999).
14. H. B. Zhao, Y. H. Ren, G. Lupke, A. T. Hanbicki and B. T. Jonker, Appl. Phys. Lett. **82**, 1422 (2003).
15. R. C. LeCaw, H. von Philipsborn, and M. D. Struge, J. Appl. Phys. **38**, 965 (1967).
16. H. L. Pinch and H. B. Berger, J. Phys. Chem. Solids **29**, 2091 (1968).
17. E. Riedel and E. Hovath, Z. Anorg. Allg. Chem. **399**, 21 (1973).
18. W. L. Lee, S. Watauchi, V. L. Miller, R. J. Cava, N. P. Ong, Science **303**, 1647 (2004).

## CHAPTER 5

### THIN FILM GROWTH OF NICKEL FERRITE

#### 5.1 Introduction

There is considerable interest in the growth of spinel ferrites films because to their numerous technological applications in areas such as microwave integrated devices,<sup>1</sup> magnetoelectric (ME) coupling heterostructures<sup>2</sup> and potentially as an active barrier material in an emerging class of spintronic devices called spin filters.<sup>3</sup> This is in large part due to the unique property of a large class of the ferrites, including  $\text{NiFe}_2\text{O}_4$  (NFO) and  $\text{CoFe}_2\text{O}_4$  (CFO), of being magnetic insulators with a high magnetic ordering temperature. The net magnetization in these materials is due to the existence of two magnetic sublattices and they are thus strictly ferrimagnetic. Due of the high resistivity of the ferrites (spinel, garnets, hexaferrites) they are widely used as passive microwave components such as isolators, circulators, phase shifters and miniature antennas operating over a wide range of frequencies (1- 100 GHz).<sup>4</sup>

Microwave technology is expanding to operation at higher and higher frequencies - up to 100 GHz - for a variety of applications. Magnetic materials that are insulating are essential to ensure total penetration of electromagnetic fields. Ferrites are electrically insulating and possess both high permeability and moderate permittivity at frequencies from dc to millimeter.<sup>5</sup> Thus, because of their low eddy current losses, they are ideally suited for electrical applications in terms of power generation, conditioning, and conversion. These unique properties also make them attractive in microwave devices such as isolators, circulators and phase shifters.<sup>4,5</sup> Typically ferrites are primarily classified into three types: spinels, hexagonal ferrites and garnets. In ferrites, the magnetic interaction between cations is through superexchange mediated by the intermediate

oxygen ions, with the *A* and *B* sublattices coupling antiferromagnetically. Due to differences in the spin configuration of the cations in the different sublattices, the resulting magnetic moment gives rise to ferrimagnetism.<sup>4</sup>

Garnets are another important class of ferrites that have an oxygen close-packed-cubic structure.  $Y_3Fe_5O_{12}$  (YIG) is one of the most well known materials in this family. Even though YIG was discovered in 1956, it remains the ideal microwave material in the 1-10 GHz band. The garnet structure consists of oxygen polyhedra's surrounding the cations. The large  $Y^{3+}$  ions are surrounded by eight oxygen's in a distorted dodecahedral structure, while the five  $Fe^{3+}$  ions are divided between the three tetrahedral sites and two octahedral sites. Single crystal YIG possesses the narrowest ferromagnetic resonance (FMR) linewidth (0.6 Oe) of all materials and thus has very low microwave loss.<sup>6</sup> The magnetic properties of YIG can be tuned by substituting different cations, such as Al or Ga, at the three crystallographic sites.

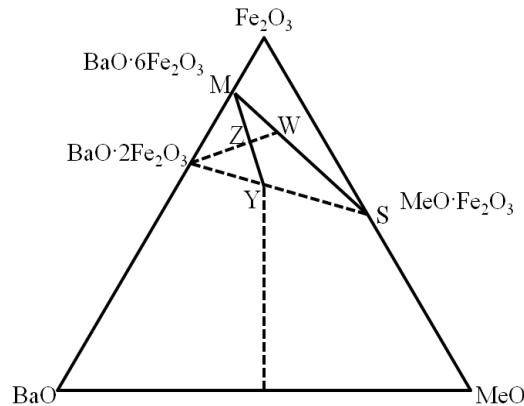


**Figure 5.1.** Phase diagram of hexaferrites. Reproduced with the permission of ref. [4].

Recently, hexagonal ferrites (hexaferrites) have attracted a lot of attention because they are suitable as microwave materials over a wider frequency range of 1-100 GHz, and also as permanent magnets. To achieve FMR conditions with garnets or spinels in the millimeter wave range, an external magnet is needed to provide a bias field. Because of very high magnetic

anisotropy, hexaferrites can operate to higher frequencies without any external bias, which is a significant advantage. There are four types of hexaferrites of different compositions, denoted as M, W, Y and Z, as shown in Fig. 5.1. The crystal and magnetic structure of different types of hexaferrites are remarkably complex, but all the types are interrelated. S and M indicate spinel  $\text{Me}^{2+}\text{Fe}_2\text{O}_4$  and  $\text{BaFe}_{12}\text{O}_{19}$ , respectively, and then the W type hexaferrite  $\text{BaMe}_2\text{Fe}_{16}\text{O}_{27}$  is  $\text{W}=\text{M}+2\text{S}$ . Y type is  $\text{Ba}_2\text{Me}_2\text{Fe}_{12}\text{O}_{22}$ , a planar hexaferrite, and Z equals  $\text{M}+\text{Y}$  is another planar hexaferrite. Due to the high anisotropy, the FMR linewidth and damping constant of hexaferrites are much larger than YIG. Nevertheless, their anisotropy and magnetic properties can be tuned by substitution. The magnetization and anisotropy of Ba-ferrite can be increased by substitution of  $\text{Al}^{3+}$ ,  $\text{Ga}^{3+}$  or  $\text{Cr}^{3+}$ ; while  $\text{Ti}^{4+}$  and  $\text{Ge}^{4+}$  substitution decrease the magnetization and anisotropy.<sup>7</sup>

Spinel ferrites remain the most frequently used material in microwave devices in the 3-30 GHz band.<sup>4</sup> One of the appealing properties of spinel ferrites is the possibility of mixing different compositions. Not only the magnetic moments, but the strength of the superexchange and Néel temperature ( $T_N$ ) of the ferrites can be changed and the degree of the inversion structure can be modified. There are numerous substitution possibilities to modify the properties of ferrites: addition of Al ion reduces the magnetization;  $\text{Co}^{2+}$  reduces the anisotropy; addition Mn ion reduces the dielectric losses; addition of  $\text{Zn}^{2+}$  increases the magnetization, but the  $T_N$  is decreased. For example,  $\text{NiFe}_2\text{O}_4$  is suitable for high-power applications; its saturation magnetic moment is  $300 \text{ emu/cm}^3$ ; and the Néel temperature is  $570^\circ\text{C}$ .<sup>8</sup> Li ferrite,  $\text{LiFe}_5\text{O}_8$ , is also frequently used because it is inexpensive, has a high Néel temperature ( $645^\circ\text{C}$ ), a square hysteresis loop, and a low linewidth,  $\Delta H \sim 3 \text{ Oe}$ .

Most microwave applications utilize bulk ferrite materials as discrete components. For future communication applications utilizing miniaturized rapid-response microwave components, the growth of high quality and thick (10-100 $\mu\text{m}$ ) films is an essential step. Spinel oxides have a large unit cell consisting of many interstitial sites and the transition metals can adopt several oxidation states. Thus, it is a challenging task to grow epitaxial spinel thick films with low defect density and excellent magnetic properties. Various thin film techniques, including pulsed laser deposition, sputtering, evaporation, etc. have been used to grow epitaxial ferrite films.<sup>9</sup> But the magnetic properties of epitaxial spinel ferrite films are generally far from ideal in comparison to those in the bulk, particularly for as-deposited films without post-annealing. Moreover, growth of thick films is not practical using these methods because of the low growth rate. We have used direct liquid injection chemical vapor deposition (DLI-CVD) for the epitaxial growth of ferrimagnetic nickel ferrite (NFO) films with high growth rate and excellent magnetic properties.

## 5.2 Experimental

We deposited ferrimagnetic NFO films with high growth rate on different substrates using DLI-CVD. The liquid precursor source was prepared by dissolving  $\text{Ni}(\text{acac})_2$  and  $\text{Fe}(\text{acac})_3$  in dimethylformamide (DMF). The metal-organic precursor solution is fed into a commercial vaporizer system (Brooks Instruments) through a liquid mass flow controller (10 g/h range), the output of which is then injected into a home-built CVD reactor. The films were grown at temperature of 450-830  $^{\circ}\text{C}$  and the base pressure was maintained at 10 to 20 Torr, with optimized oxygen and argon gas flow rates. The DLICVD optimum condition is as following list.

Precursor concentration    0.1 molar

Precursor flow rate	6 g/h
Vaporizer temperature	175 °C
Carrier gas (Ar) flow rate	300 sccm
Oxygen flow rate	400 sccm
Reaction chamber pressure	10-20 Torr
Substrate temperature	450-830 °C

After growth, the samples were maintained under the same oxygen flow rate condition until they cooled down to room temperature. A standard  $\theta-2\theta$  x-ray diffraction setup (Phillips X'pert Pro) was used to determine the phase and epitaxy of the films. XRD measurements were performed using a  $\text{CuK}\alpha$  source operating at 45 kV and 40 mA. The surface morphology of the films was characterized using atomic force microscopy (Veeco NanoScope) scanned in the tapping mode. The growth rate was calibrated using cross-section images obtained using a scanning electron microscope (SEM). Energy-dispersive x-ray spectroscopy (EDS) was used to determine the film cation stoichiometry. The magnetic property of NFO films measurements were performed using AGM, VSM and SQUID.

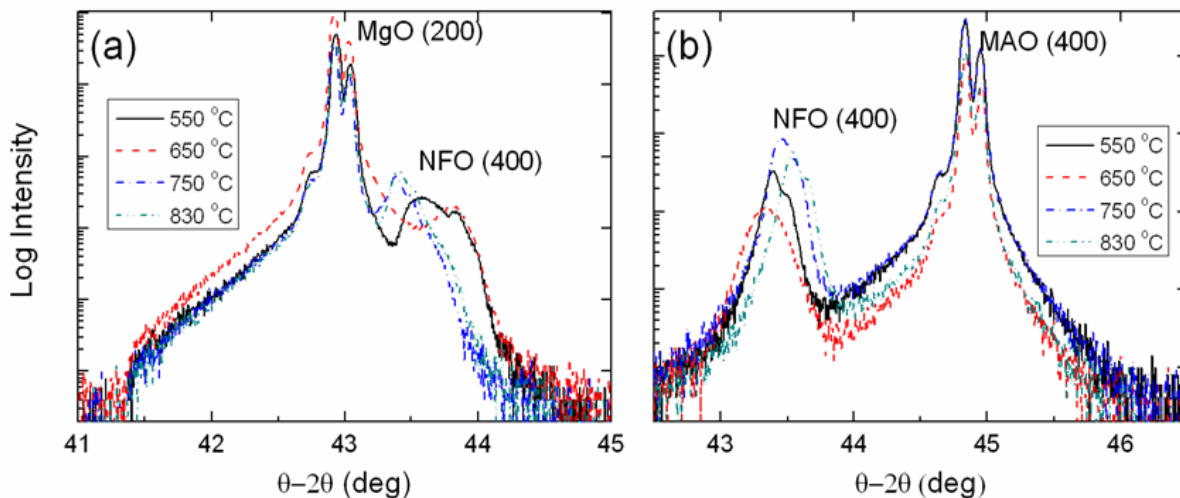


**Figure 5.2.**  $\theta-2\theta$  Bragg diffraction patterns of  $\text{NiFe}_2\text{O}_4$  films grown on: (a)  $\text{MgO}$  (100) and (b)  $\text{MgAl}_2\text{O}_4$  (100) substrates at various temperatures.

### 5.3 Results and Discussions

The  $\text{NiFe}_2\text{O}_4$  films ( $a = 8.34 \text{ \AA}$ ) have been grown epitaxially on  $\text{MgO}$  (100) and  $\text{MgAl}_2\text{O}_4$  (100) substrates. Rocksalt  $\text{MgO}$  ( $a = 4.2 \text{ \AA}$ , 0.8 % lattice mismatch) is closely lattice-matched to NFO, with a lattice parameter almost exactly half that of NFO. But, spinel ferrite films grown on  $\text{MgO}$  are prone to anti-phase boundaries (APBs) from cation stacking defects originating from equivalent nucleation sites. On the other hand,  $\text{MgAl}_2\text{O}_4$  ( $a = 8.08 \text{ \AA}$ , ~3 % lattice mismatch) has the iso-structural spinel structure, which despite the large lattice mismatch results in a reduced density of anti-phases boundaries.

Further insight regarding the structure and crystallinity of NFO films is obtained from x-ray diffraction studies, which provides information on texture of film grown on different substrates, film orientation with reference to the substrate, film lattice constants, etc. Large-angle  $2\theta$ - $\theta$  scans show only diffraction peaks corresponding to NFO and the substrate. No evidence of any secondary phases is found. Figure 5.2a and 5.2b display the result of the  $\theta$ - $2\theta$  Bragg diffraction scans showing that the NFO (400) peak shifts to relatively lower and higher angles for films

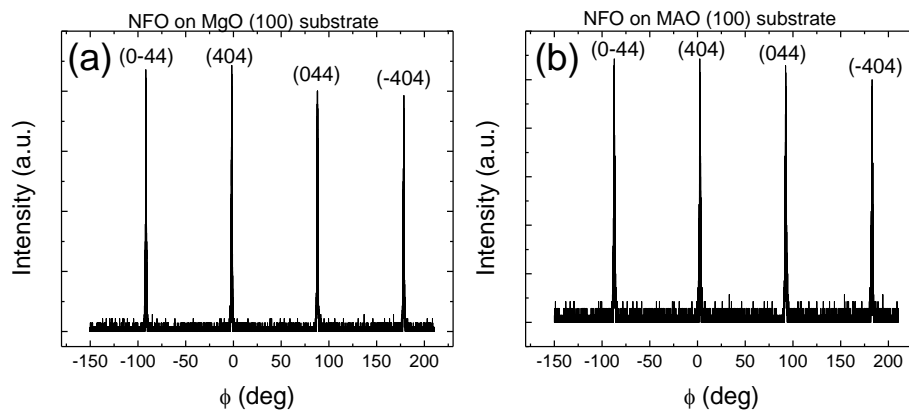


**Figure 5.3.**  $\phi$  scan for (404) reflection of  $\text{NiFe}_2\text{O}_4$  films grown on (a)  $\text{MgO}$  (100) and (b)  $\text{MgAl}_2\text{O}_4$  (100) substrates at  $650^\circ\text{C}$ .

deposited on  $\text{MgO}$  and  $\text{MgAl}_2\text{O}_4$  (MAO) substrates, respectively, with increasing deposition

temperature (except for the films grown at 650°C). Films grown at 450 °C show no diffraction peaks (not shown) and are amorphous. Epitaxial analysis has been further carried out by performing phi-scans around the (404) reflection of the film and substrate. Figure 5.3a and 5.3b shows the  $\phi$  scan of the off-axis (404) reflection for NFO films grown on MgO and MAO substrates, respectively. Four sharp peaks, 90 degrees apart, confirm cubic symmetry with perfect cube-on-cube epitaxial growth of the films.

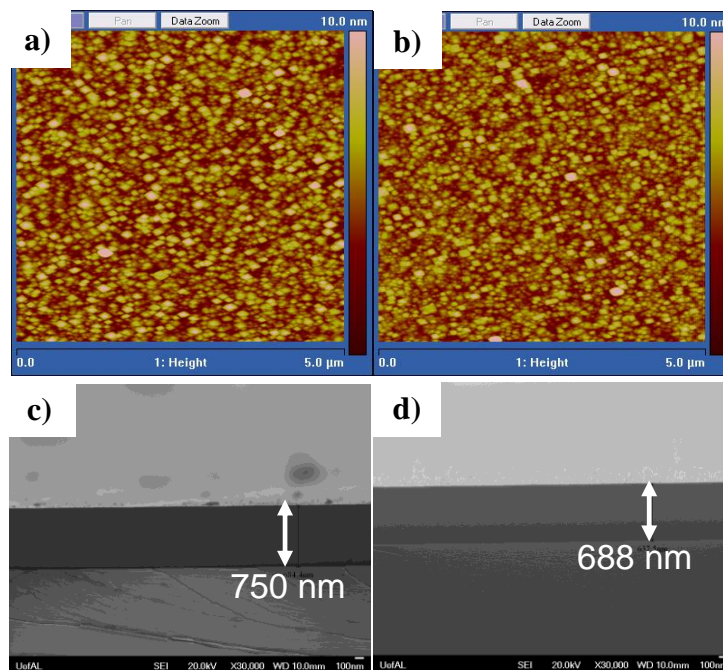


**Figure 5.4.** AFM images of  $\text{NiFe}_2\text{O}_4$  films grown on (a) MgO (100) and (b)  $\text{MgAl}_2\text{O}_4$  (100) substrates at 650°C. The SEM Cross-section view of  $\text{NiFe}_2\text{O}_4$  films grown on (c) MgO (100) and (d)  $\text{MgAl}_2\text{O}_4$  (100) substrates at 650°C.

The surface topology of the films has been imaged using atomic force microscopy (AFM). The films are generally smoother when grown at a lower temperature, *i.e.*, the roughness increases with increasing growth temperature for films grown on both substrates (see Table 5.1). As an example, Fig. 5.4a and 5.4b show the AFM images of NFO films grown at 650 °C on MgO and MAO substrate, respectively, with relatively smooth morphology. The film roughness

increases dramatically when the growth temperature is increased from 750 °C to 830 °C, which is likely due to the onset of three dimensions island growth mode leading to a rough surface morphology.<sup>10</sup> We have used the SEM to obtain cross-section images of the films and thereby accurately determine the film thickness (Fig. 5.4c and 5.4d). The growth rate varies with temperature and is in the range of 0.7-1.0 μm/hour, which is significantly higher than that reported using physical deposition techniques.

The film composition is obtained using EDS. The Ni:Fe ratio, as listed in Table 5.1, is close to the ideal 1:2 value for intermediate growth temperatures (650-750°C) but show some deviation both at lower and higher growth temperatures.

Up to date, various thin film techniques, including pulsed laser deposition (PLD), sputtering, evaporation and chemical techniques have been used to grow epitaxial ferrite films.<sup>7</sup> But the

**Table 5.1.** The properties of NiFe<sub>2</sub>O<sub>4</sub> films grown on MgO and MgAl<sub>2</sub>O<sub>4</sub> substrates at different temperatures.

Substrate	Substrate temp. (°C)	Lattice(Å) (2θ, deg)	FWHM (deg)	Thickness (nm)	Roughness (nm)	M <sub>S</sub> (emu/cc)	Ni:Fe
MgO	450	n/a	n/a	1000	4.37	25	1.0:2.69
	550	8.300 (43.58)	0.18	670	0.92	230	1.0: 2.22
	650	8.309 (43.53)	0.22	750	1.68	290	1.0:2.11
	750	8.338 (43.375)	0.20	860	24.6	247	1.0:2.08
	830	8.333 (43.40)	0.18	1028	37.7	263	1.0:1.66
MAO	450	n/a	n/a	1000	4.5	31	1.0:2.60
	550	8.333 (43.40)	0.62	640	0.81	290	1.0: 2.28
	650	8.346 (43.33)	0.48	688	1.92	323	1.0:2.12
	750	8.326 (43.44)	0.25	800	5.86	325	1.0:2.08
	830	8.308 (43.54)	0.20	1025	51.3	295	1.0:1.54

magnetic properties of epitaxially grown spinel ferrite films are generally far from ideal in comparison to those in the bulk, particularly for as-deposited films without post-anneal. For example, Venzke *et al.*<sup>8</sup> obtained a saturated magnetic moment ( $M_S$ ) value of 190 emu/cm<sup>3</sup> for NFO films deposited by sputtering, which is quite a bit lower than the bulk value of 300 emu/cm<sup>3</sup>.

Room-temperature magnetization loops (M-H) for our films were obtained using alternating gradient magnetometry (AGM) and vibrating sample magnetometry (VSM) with the field applied in the plane of the film. For NFO films grown at 650 °C the M-H curves, shown in Fig. 5.5, were obtained with the magnetic field in the plane of the film and the saturation moment

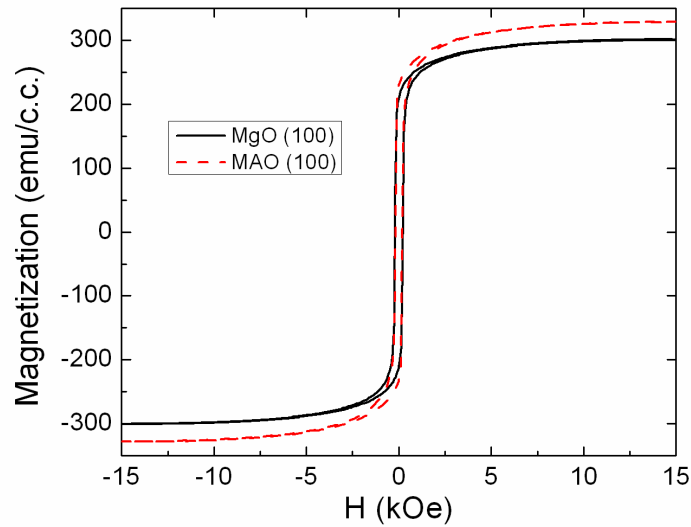


**Figure 5.5.** The magnetization of NiFe<sub>2</sub>O<sub>4</sub> films grown on MgO (100) and MgAl<sub>2</sub>O<sub>4</sub> (100) substrates at 650°C.

values are 302 and 325 emu/cc for growth on MgO and MAO substrates, respectively. The moments for these as-deposited films are very close to that obtained in bulk NFO. The coercivities of both films shown in Fig. 5.5 are around 200 Oe and the M-H loops are close to square, both of which are signatures of high quality films.<sup>11</sup> Quantitatively, for films grown on MgO substrate, those grown at 650 °C show the highest saturation moment, and the moment

decreases by about 30 to 40 emu/cc for films grown at higher temperatures. This is likely caused by higher temperature diffusion of Mg from the substrate into the films, as has been reported previously.<sup>12</sup> For films grown on MAO substrate, the saturation moment values are similar for all films grown at 550 °C and higher temperature.

In addition to the ferrites, we have begun investigating the growth of chalcospinels thin films (*e.g.*, CuCr<sub>2</sub>S<sub>4</sub>) using DLI-CVD. We have already tested several precursors as source materials, including metal dithiocarbamates and dithioacetates. Thus far all the deposited films have turned out to be amorphous, even for those exhibiting the correct cation stoichiometry. A likely cause is the anion deficiency in the film at the high growth temperature. Further optimization of process parameters, including provision for a separate source of chalcogen, is being explored for the successful epitaxial growth of chalcospinel thin films.

In summary, NFO films have been grown epitaxially on MgO (100) and MAO (100) substrates with high growth rate. The magnetic properties are comparable to those of the bulk material. For the future, growth of other ferrite materials that are suitable for microwave applications over different frequency ranges, such as lithium ferrite, garnets, hexaferrites, etc., will be explored using DLI-CVD. While the present work on the growth of spinel films has been motivated by microwave applications, the DLI-CVD growth process can readily be modified for growth of thin films of these materials needed for spintronic applications, which we plan to explore. Moreover, we will investigate the growth of chalcospinel thin films, which while being challenging are very attractive for spintronic device applications. Our ultimate goal is to synthesize a new class of chalcospinels, which are predicted to be half-metallic based on band-structure calculations discussed earlier, which can find applications in the field of spintronics and in other areas.

## 5.4 References

1. J. D. Adams, S. V. Krishnaswamy, S. H. Talisa, K. C. Yoo, *J. Magn. Magn. Mater.*, **83**, 419 (1990).
2. (a) C. Deng, Y. Zhang, J. Ma, Y. Lin, C.-W. Nan, *J. Appl. Phys.*, **102**, 074114 (2007). (b) Y. Zhang, C. Deng, J. Ma, Y. Lin, C.-W. Nan, *Appl. Phys. Lett.*, **92**, 062911 (2008). (c) J. J. Yang, Y. G. Zhao, H. F. Tian, L. B. Luo, H. Y. Zhang, Y. J. He, H. S. Luo, *Appl. Phys. Lett.*, **94**, 212504 (2009).
3. (a) U. Luders, A. Barthélemy, M. Bibes, K. Bouzehouane, S. Fusil, E. Jacquet, J.-P. Contour, J.-F. Bobo, J. Fontcuberta, A. Fert, *Adv. Mater.*, **18**, 1733 (2006). (b) M. G. Chapline, S. X. Wang, *Phys. Rev. B*, **74**, 014418 (2006). (c) A. V. Ramos, M.-J. Guittet, J.-B. Moussy, R. Mattana, C. Deranlot, F. Petroff, C. Gatel, *Appl. Phys. Lett.*, **91**, 122107 (2007).
4. M. Pardavi-Horvath, *J. Magn. Magn. Mater.* **215-216**, 171 (2000).
5. (a) J. D. Adams, S. V. Krishnaswamy, S. H. Talisa, K. C. Yoo, *J. Magn. Magn. Mater.* **83**, 419 (1990); (b) V. G. Harris, A. Geiler, Y. Chen, S. D. Yoon, M. Wu, A. Yang, Z. Chen, P. He, P. V. Parimi, X. Zuo, C. E. Patton, M. Abe, O. Acher, C. Vittoria, *J. Magn. Magn. Mater.* **321**, 2035-2047 (2009).
6. (a) R. C. Linares, *J. Cryst. Growth*, **3-4**, 443 (1968). (b) J. Desvignes, D. Mahasoro, H. Gall, *IEEE Trans. Magn.*, **23**, 3724 (1987).
7. (a) V. Babu, P. Padaikathan, *J. Magn. Magn. Mater.* **241**, 85 (2002); (b) P. Shi, H. How, X. Zuo, S. D. Yoon, S. A. Oliver, C. Vittoria, *IEEE Trans. Magn.* **37**, 2389 (2001); (c) P. Hernandez-Gomez, C. De Francisco, V. A. M. Braders, J. H. J. Dalderop, *J. Appl. Phys.* **87**, 3576 (2000); (d) P. Brahma, S. Banerjee, S. Chakraborty, D. Chakravorty, *J. Appl. Phys.* **88**, 6526 (2000); (e) P. A. Marino-Casterllanos, J. Anglada-Rivera, A. Cruz-Fuentes, R. Lora-Serrano, *J. Magn. Magn. Mater.* **280**, 214 (2004).
8. S. Venzke, R. B. van Dover, J. M. Phillips, E. M. Gyorgy, T. Siegrist, C. H. Chen, D. Werder, R. M. Fleming, R. J. Felder, E. Coleman, R. Opila, *J. Mater. Res.* **11**, 1187 (1996).
9. (a) C. M. Williams, D. B. Chrisey, P. Lubitz, K. S. Grabowski, C. M. Cotell, *J. Appl. Phys.* **75**, 1676 (1994); (b) R. B. van Dover, S. Venzke, E. M. Gyorgy, T. Siegrist, J. M. Phillips, J. H. Marshall, R. J. Felder, *Mater. Res. Soc. Symp. Proc.* **341**, 41 (1994); (c) Z.-J. Zhou, J. J. Yan, *J. Magn. Magn. Mater.* **115**, 87 (1992); (d) D. T. Margulies, F. T. Parker, F. E. Spada, A. E. Berkowitz, *Mater. Res. Soc. Symp. Proc.* **341**, 53 (1994); (e) S. A. Chambers, F. F. C. Farrow, S. Maat, M. F. Toney, L. Folks, J. G. Catalano, T. P. Trainor, G. E. Brown Jr., *J. Magn. Magn. Mater.* **246**, 124 (2002).
10. F. K. LeGoues, M. Copel, R. Tromp, *Phys. Rev. Lett.* **63**, 1826 (1989).
11. J. Roberts, *High Frequency Applications of Ferrites*, edited by P. A. Porter, Princeton, New

Jersey, 1960.

12. A. G. Fitzgerald, *J. Mater. Sci.* **22**, 1887 (1987).

## CHAPTER 6

### CONCLUSIONS

This dissertation work can be divided into three major research projects. All of them are related to spinel-based materials and their properties, both experimental and theoretical. The significant results from each project are summarized below.

#### SYNTHESES OF SPINEL FERRITES AND COPPER CHROMIUM SELENIDE NANOCRYSTALS

We have developed a novel and facile solution-based technique using mixed metal-oleate precursors for the synthesis of monodisperse nanocrystals of a wide variety of magnetic ferrite materials ( $\text{CoFe}_2\text{O}_4$ ,  $\text{NiFe}_2\text{O}_4$ ,  $\text{FeFe}_2\text{O}_4$ , etc.). The saturation magnetization of the different nanocrystals is close to their respective theoretical values. Other than  $\text{CoFe}_2\text{O}_4$ , the hysteresis loops for the other ferrites display very low coercivities, with no remanence, as would be expected for superparamagnetic behavior. The process has been extended to the synthesis of different size chalcospinels ( $\text{CuCr}_2\text{Se}_4$ ) and also chalcopyrites ( $\text{CuIn}_x\text{Ga}_{1-x}\text{Se}_2$  and  $\text{CuFeS}_2$ ) nanocrystals using different precursors. The magnetic properties of  $\text{CuCr}_2\text{Se}_4$  chalcospinel and the optical properties of the chalcopyrites have been studied in detail. It would be useful to further expand the process for the synthesis of other chalcospinel ( $\text{CuCr}_2\text{S}_4$ ,  $\text{CdCr}_2\text{S}_4$ ,  $\text{CdCr}_2\text{Se}_4$  etc.) nanocrystals, which exhibit unusual magnetic and transport properties. Some of the synthesis techniques we have developed can likely be utilized for synthesis of these materials with suitable modification.

## FIRST-PRINCIPLES CALCULATIONS ON CHROMIUM-BASED CHALCOSPINELS

We have theoretically investigated the electronic band structure of the two quaternary systems,  $\text{Cd}_x\text{Cu}_{1-x}\text{Cr}_2\text{S}_4$  and  $\text{Cd}_x\text{Cu}_{1-x}\text{Cr}_2\text{Se}_4$ , and also a number of anion-substituted Cr-based chalcospinels. We predict a wide range of possible half-metal compositions which can be tuned both from ferromagnetic metals and ferromagnetic semiconductors. Our calculations indicate that for  $A = \text{Cu}$  and  $\text{Cd}$ -based chalcospinels the magnetic moment scales approximately linearly with anion substitution concentration. In the future it would be useful to investigate other half-metal in the chalcospinels family, particularly ones with a high Curie temperature.

## THIN FILM GROWTH OF NICKEL FERRITE

We have expanded the synthesis of spinels to the growth of  $\text{NiFe}_2\text{O}_4$  ferrite films using the direct liquid injection CVD (DLI-CVD) technique. The preliminary results obtained for the growth of epitaxial  $\text{NiFe}_2\text{O}_4$  films on (100)-oriented  $\text{MgO}$  and  $\text{MgAl}_2\text{O}_4$  substrates are very encouraging. They exhibit very good structural properties and the magnetic properties are comparable to those observed in the bulk, even for films grown at a high deposition rate. We believe that the process can be readily extended to the growth of films of other ferrite materials, including  $\text{LiFe}_5\text{O}_8$  and the hexaferrites, which are suitable for microwave applications over a wide frequency range. Another exciting possibility is the use of direct liquid injection CVD technique for the growth of chalcospinels films - in particular those predicted to be half-metallic - which have the potential for realizing a new class of spintronics devices.

## APPENDIX I

### SYNTHESIS OF TERNARY AND QUATERNARY $\text{CuIn}_x\text{Ga}_{1-x}\text{Se}_2$ ( $0 \leq x \leq 1$ ) SEMICONDUCTOR NANOCRYSTALS

Reproduced in part with permission from [Wang, Y.-H. A. *et al. Solid State Sci.* **11**, 1961-1964 (2009) ] Copyright [2009] Elsevier Masson SAS.

#### 1. Introduction

A wide variety of materials have been utilized for solar cells ranging from elemental Si to the binary group III-V and II-VI semiconductors, and the more complex ternary alloys - such as  $\text{CuInS}(\text{Se})_2$ . Because of the large absorbance coefficient, small band gap and good radiation stability, the I-III-VI<sub>2</sub> chalcopyrites are of considerable interest as the photon absorber material in thin-film solar cells.<sup>1,2</sup> Substituting Ga for In in the Se-based chalcopyrite  $\text{CuIn}_x\text{Ga}_{1-x}\text{Se}_2$  (CIGS) enables continuous tuning of the band gap from 1.07 to 1.7 eV<sup>3</sup>. Single-junction solar cells fabricated using polycrystalline CIGS as an absorber layer have already demonstrated efficiencies close to 20 %.<sup>4,5</sup>

Recently, the use of semiconducting colloidal nanocrystals (NCs) has shown promise as a low-cost approach for the fabrication of photovoltaics.<sup>6-9</sup> The composition, size and shape of the nanocrystals all play an important role in determining the performance of these cells. It is well established that semiconductor NCs exhibit a blue-shift in the optical spectra with decreasing particles size due to quantum confinement.<sup>10</sup> Both the tunability and the possibility of forming multiple electron-hole pairs<sup>11</sup> in NCs are attractive features for enhancing solar cell efficiency. For CIGS, it is important to synthesize NCs with a narrow size distribution to investigate their optical properties and explore their utility in fabricating low-cost solar cells.

Unlike binary chalcogenides,<sup>12-15</sup> the synthesis of ternary or quaternary CIGS nanocrystals is complicated - in particular controlling the stoichiometry. Nevertheless, some of the chalcopyrites

- especially  $\text{CuInS}_2$  and  $\text{CuInSe}_2$  - have been synthesized as NCs using different solution routes.<sup>16-24</sup> Yoon and co-workers have reported a solvothermal method for the synthesis of CIGS NCs over a limited range of In/Ga concentration. While it is possible to obtain phase-pure material, the solvothermal reaction results in the formation of relatively large crystallites with a broad size distribution. More recently, Panthani *et al.* have reported the synthesis of CIGS nanocrystals ranging from ~5 nm to ~25 nm in diameter by arrested precipitation in solution, but with limited control of the shape and size distribution.<sup>24</sup> Herein, we report on the facile synthesis of phase-pure CIGS NCs (~20-30 nm) of both cubic and spherical morphology across the whole composition range ( $0 \leq x \leq 1$ ) with a narrow size distribution that readily form a colloidal suspension.

## 2. Experimental

The synthesis process involves the thermal decomposition and reaction of metal-acetylacetonate precursors with selenium-oleylamine (OLA) as the selenium source.<sup>25</sup> All the reactions were performed in a fume hood, under inert condition, and elemental selenium (Se) was disposed off using safe laboratory techniques. The details of the experimental setup for the reaction is described in section 2.1. In a typical reaction for the synthesis of NCs with cubic morphology, 1.5 mmol Se powder was dissolved in 10 ml of OLA at 330-340 °C under nitrogen atmosphere and then cooled down to 150 °C. 1.2 mmol tri-n-octylphosphine oxide (TOPO) was added at this temperature while maintaining a continuous flow of nitrogen. Separately, 0.25 mmol of copper (II) acetylacetonate (acac), 0.25 mmol indium/gallium acetylacetonate (acac), in the desired In:Ga mole ratio of the CIGS product, and 1.2 mmol 1,2-hexadecanediol were mixed in 3 ml of 1-octadecene (ODE) at ~170 °C under vacuum and then backfilled with nitrogen. The

Se/OLA/TOPO solution was heated and after the temperature reached 220 °C the cation mixture was injected under nitrogen atmosphere and the resultant mixture heated to 280 °C in 30 minutes. The reaction mixture was then maintained at this temperature for another 30 minutes while being continually stirred, during which a yellowish black solution was formed. After cooling down to room temperature, a mixture of hexane and ethanol was added to the solution and a black product precipitated via centrifugation. A similar procedure was used for the synthesis of spherical NCs. The difference being that the metal acetylacetonate precursors were dissolved in 2 ml oleic acid (OA) and 1.2 mmol 1,2-hexadecanediol and was added to the Se solution simultaneously with TOPO.

The morphology and size distribution of the NCs was determined using transmission electron microscopy (TEM, FEI Tecnai F-20). For this purpose the NCs were dispersed in hexane and spray-dried on a TEM copper grid. X-ray powder diffraction (XRD, Bruker D8) was used to study the structure of the NCs, and the optical property was measured using UV–Vis diffuse reflectance spectra (UV-Vis-NIR, Varian Cary 5G). The samples for UV-Vis measurement was dispersed in hexane with ~0.02 % OLA as surfactant. The composition of the NCs was obtained using atomic absorption spectroscopy (AAS, PerkinElmer AAnalyst 400). The NC compounds were dissolved in nitric acid and appropriately diluted for the measurements.

### 3. Results and Discussion

By varying the synthesis conditions, we have determined that Se with 200 % excess during reaction is optimum for obtaining NCs with the required anion stoichiometry and a narrow size distribution. For lower Se concentrations, the NCs are Se deficient. Also, lower reaction temperatures results in the formation of impurity phase(s). Using OLA as a solvent for dissolving

the precursors is not suitable, since Ga-acac is readily reduced to Ga metal and the morphology of the NCs also degrades for higher Ga concentrations. The addition of TOPO as a surfactant

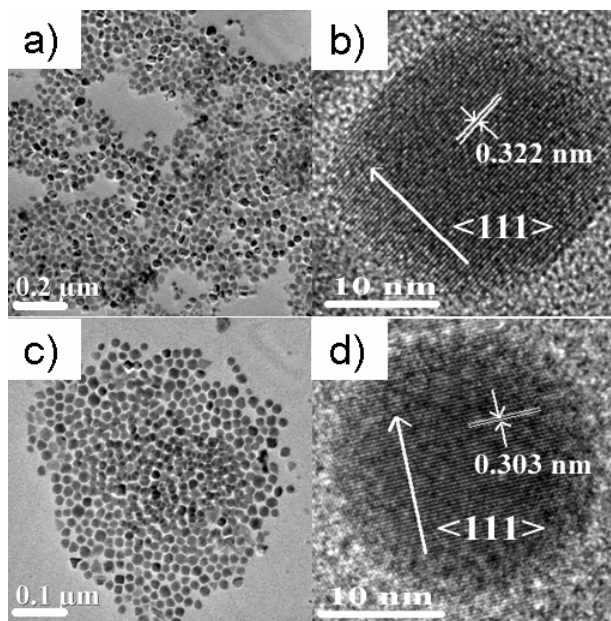


**Figure 1.** TEM images of  $\text{CuIn}_x\text{Ga}_{1-x}\text{Se}_2$  NCs with a) cubic ( $x = 0.5$ ) and c) spherical ( $x=0$ ) morphology and the respective HRTEM images b) and d).

helps control the morphology and also improves the dispersity of the product.

The morphology of the synthesized materials has been investigated using TEM. As seen in Fig. 1, the NCs obtained using ODE as solvent exhibit close to cubic morphology (Fig. 1a), while those using OA exhibit a spherical morphology (Fig 1c), with an average size of 25 nm and 20 nm, respectively. In both cases, the NCs have a size distribution of  $\pm 15\%$  (the size distribution is obtained by measuring the size of hundreds of nanocrystals and then calculation the deviation). The high resolution TEM (HRTEM) images of the NCs are shown in Fig. 1b and 1d. Clear lattice fringes are observed in the magnified images with spacings of  $d=0.322$  nm (Fig. 1b) and 0.303 nm (Fig 1d), corresponding to the (111) lattice planes for the respective compositions. With use of both solvents, the size distribution is observed to improve in going from  $\text{CuInSe}_2$  to  $\text{CuGaSe}_2$ .

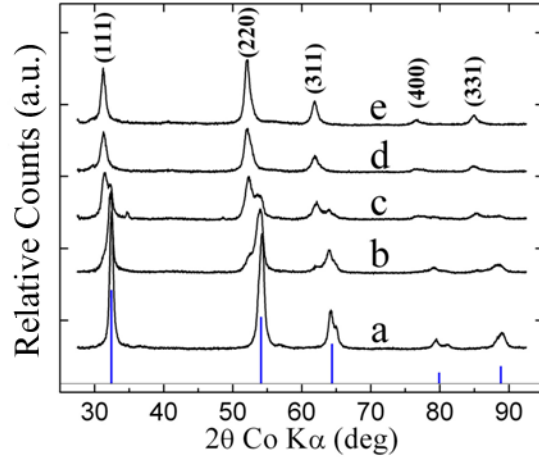


**Figure 2.** X-ray powder diffraction patterns (using Co K $\alpha$  source,  $\lambda = 1.789 \text{ \AA}$ ) of near-cubic morphology a) CuGaSe<sub>2</sub>, b) CuIn<sub>0.25</sub>Ga<sub>0.75</sub>Se<sub>2</sub>, c) CuIn<sub>0.5</sub>Ga<sub>0.5</sub>Se<sub>2</sub>, d) CuIn<sub>0.75</sub>Ga<sub>0.25</sub>Se<sub>2</sub> and e) CuInSe<sub>2</sub>. The simulated XRD pattern of the sphalerite phase of CuGaSe<sub>2</sub> is shown at the bottom.

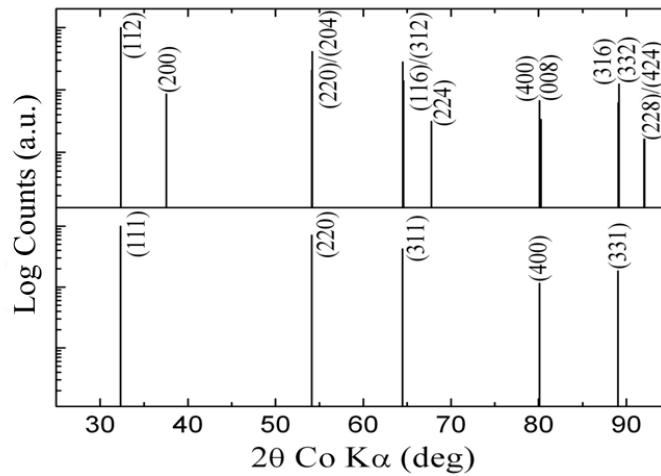


**Figure 3.** Simulated XRD patterns of CuGaSe<sub>2</sub> having the chalcopyrite (top) and sphalerite (bottom) phase.

As seen in Fig. 2a, the major XRD diffraction peaks for CGS ( $x = 0$ ) NCs appear at  $2\theta$  values of 32.4, 54.2, 64.2, 79.8 and 88.8°. The experimental pattern matches well with the simulated pattern shown below for the cubic sphalerite phase with zinc blende structure having a random distribution of the cations. While the simulated pattern in Fig. 3 for the chalcopyrite phase is quite similar, two additional weak intensity peaks (at 37.5 and 67.8°) because of complete cation ordering are expected. Since these peaks are not observed for CGS ( $x = 0$ , Fig. 2a), or the other CuIn <sub>$x$</sub> Ga<sub>1- $x$</sub> Se<sub>2</sub> compositions (Figs. 2b-e), we conclude that the NCs lack complete cation

ordering.<sup>18</sup> Because of tetragonal distortion ( $a, b \neq c$ ), a splitting of the peaks is observed in all

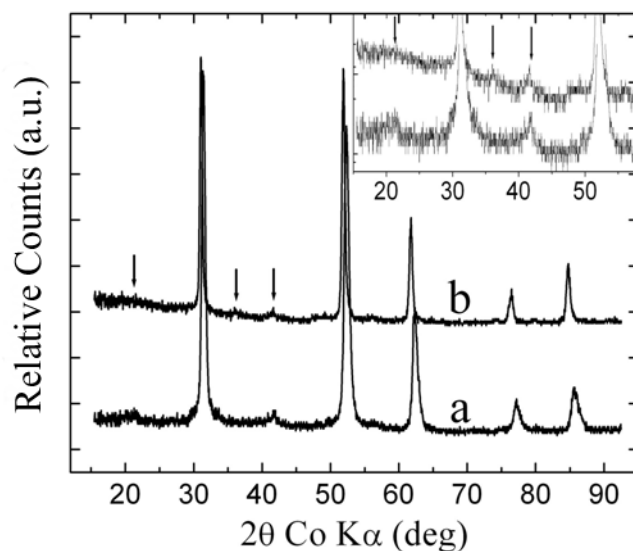


**Figure 4.** X-ray powder diffraction patterns (using a Co K $\alpha$  source,  $\lambda = 1.789 \text{ \AA}$ ) of: a) CuIn<sub>0.5</sub>Ga<sub>0.5</sub>Se<sub>2</sub> and b) CuInSe<sub>2</sub> after annealing at 350 °C for 30 minutes. The additional peaks from the chalcopyrite phase are marked by arrows.

the spectra except for those with high In concentration. The distortion likely results from partial cation ordering. Indeed, a brief anneal of the as-synthesized NCs at 350 °C is sufficient for the formation of the ordered chalcopyrite phase for all the different compositions (see Fig.4).

A systematic shift in the peaks to lower angles is noted in Fig. 2 with increasing In substitution, as is expected because of its larger size as compared to Ga. From the peak widths, the average crystalline size is estimated to be in the range of 22 - 30 nm, and is in good agreement with the TEM results. The average composition of the NCs determined using atomic absorption spectroscopy (AAS) is shown in Table 1. It is apparent that the Cu:In:Ga:Se concentration is very close to the expected ratio over the whole composition range. The composition of some of the samples has been further confirmed using energy dispersive x-ray analysis (EDX), with no significant particle to particle composition variation being observed.

The optical absorbance spectra of the NCs for all the compositions, measured in dilute hexane dispersion, exhibit a broad absorption in the visible with a tail extending to longer

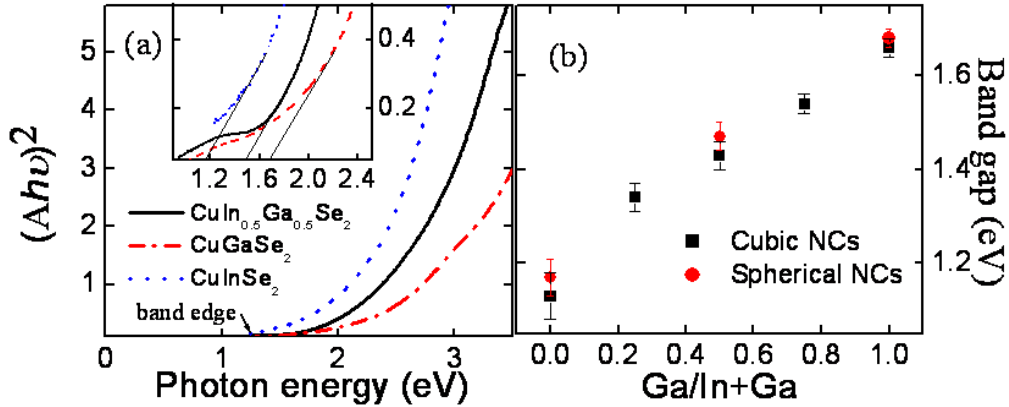


**Figure 5.** (a) Room temperature absorption spectra of  $\text{CuGaSe}_2$ ,  $\text{CuIn}_{0.5}\text{Ga}_{0.5}\text{Se}_2$  and  $\text{CuInSe}_2$  spherical NCs. Inset shows extrapolation of the spectra in the band edge region to determine the band gap; (b) plot of the band gap as a function of  $\text{Ga}/\text{In}+\text{Ga}$  concentration for both cubic and spherical shape NCs.

wavelengths. We have determined the absorbance onset by plotting  $(Ah\nu)^2$  versus  $h\nu$  ( $A$  = absorbance,  $h$  = Planck's constant and  $\nu$  = frequency ) and extrapolating the slope in the band edge region, as shown in Fig. 5a.<sup>24-28</sup> A plot of the band gap versus  $\text{Ga}/\text{In}+\text{Ga}$  concentration for both the cubic and spherical morphology NCs, along with the associated error in determination, is shown in the Fig. 5b. The band gap increases with increasing Ga concentration, with values ranging between 1.13 to 1.67 eV. These values are close to those observed in the bulk (1.07 to 1.7 eV).

It is well known that size quantization in semiconductor nanocrystals occur at dimensions smaller than the Wannier-Mott (WM) exciton of the corresponding bulk phase.<sup>29</sup> We have used the WM-exciton Bohr radius formula

$$R_B = \frac{\epsilon_\infty}{\mu} \times a_B, \quad (1)$$

where  $\epsilon_\infty$  is dielectric constant;  $\mu$  (equal to  $(\mu_e^{-1} + \mu_h^{-1})^{-1}$ ) = reduced effective excitation mass;  $a_B$  = Bohr radius of hydrogen atom, to estimate the WM-exciton size for  $\text{CuInSe}_2$  and  $\text{CuGaSe}_2$  to be

17.9 nm and 6.7 nm, respectively.<sup>30-33</sup> Since these values are smaller than the actual size of the nanocrystals, it is unlikely that the observed difference in the band gap with respect to the bulk is due to size confinement effect. Instead, we believe that the small differences are likely due to molecularity ( $\Delta m$ ) and valency ( $\Delta s$ ) deviations (see Table 1).<sup>34,35</sup> Both  $\Delta m$  and  $\Delta s$  are useful for quantifying the deviation of the composition of I-II-VI<sub>2</sub> compounds from their ideal stoichiometric values.

#### 4. Conclusions

In conclusion, we have synthesized both cubic and spherical CuIn<sub>x</sub>Ga<sub>1-x</sub>Se<sub>2</sub> semiconductor NCs across the whole composition range via a simple solution-based route involving the thermal decomposition and reaction of metal-acetylacetonate precursors with selenium-oleylamine (OLA). The as-synthesized NCs have close to the sphalerite structure and can be converted to the

**Table 1.** The composition, molecularity deviation and valence deviation of synthesized CuIn<sub>x</sub>Ga<sub>1-x</sub>Se<sub>2</sub> ( $0 \leq x \leq 1$ ) nanocrystals.

	CuInSe <sub>2</sub>	CuIn <sub>0.75</sub> Ga <sub>0.25</sub> Se <sub>2</sub>	CuIn <sub>0.5</sub> Ga <sub>0.5</sub> Se <sub>2</sub>	CuIn <sub>0.25</sub> Ga <sub>0.75</sub> Se <sub>2</sub>	CuGaSe <sub>2</sub>
Cu	23.46	26.04	20.86	21.61	25.22
In	21.90	19.74	15.57	7.77	-
Ga	-	9.91	12.60	22.63	26.83
Se	54.64	44.31	50.97	47.99	47.95
$\Delta s$	0.225	-0.229	-0.033	-0.149	-0.093
$\Delta m$	0.072	-0.121	-0.259	-0.289	-0.060

$$\Delta s = \frac{2 \times [VI]}{[I] + 3 \times [III]} - 1 \quad \Delta m = \frac{[I]}{[III]} - 1$$

[I]: Concentration of A side cation, Cu<sup>+</sup>; [III]: Concentration of B side cations, In<sup>3+</sup> and Ga<sup>3+</sup>; [VI]: Concentration of anion, Se<sup>2-</sup>.

chalcopyrite phase after a mild thermal treatment. As expected, the band gap of the NCs increases with increasing Ga and the values are close to those in the bulk. The formation of CIGS absorber film from a colloidal ink of NCs is potentially attractive for the low-cost fabrication of thin-film solar cells.

## 5. References

1. V. Nadenau, D. Braunger, D. Hariskos, C. Kaiser, M. Ruckh, R. Schaffer, T. Schmid, *Prog. Photogr. Res. Appl.* **3**, 363 (1995).
2. S. Niki, P. J. Fons, A. Yamada, O. Hellman, T. Kurafuji, S. Chichibu, H. Nakanishi, *Appl. Phys. Lett.* **69**, 647 (1996).
3. S.-H. Wei, S. B. Zhang, A. Zunger, *Appl. Phys. Lett.* **72**, 3199 (1998).
4. A. Rockett, R. W. Birkmire, *J. Appl. Phys.* **70**, R81 (1991).
5. K. Ramanathan, M. A. Contreras, C. L. Perkins, S. Asher, F. S. Hasonn, J. Keane, D. Young, M. Pomero, W. Metzger, R. Noufi, J. Ward, A. Duda, *Prog. Photovol. Res. Appl.* **11**, 225 (2003).
6. R. P. Raffaele, S. L. Castro, A. F. Hepp, S. G. Bailev, *Prog. Photovolt. Res. Appl.* **10**, 433 (2002).
7. W. Huynh, J. J. Dittmer, A. P. Alivisatos, *Science* **295**, 225 (2002).
8. V. L. Colvin, M. C. Schlamp, A. P. Alivisatos, *Nature* **380**, 354 (1994).
9. B. Q. Sun, E. Marx, N. C. Greenham, *Nano Lett.* **3**, 961 (2003).
10. A. P. Alivisatos, *Science* **271**, 225 (1996).
11. A. J. Nozik, *Chem. Phys. Lett.* **457**, 3 (2008).
12. J. Joo, H. B. Na, Y. Yu, J. H. Yu, Y. W. Kim, F. Wu, J. Z. Zhang, T. Hyeon, *J. Am. Chem. Soc.* **125**, 11100 (2003).
13. U. K. Gautam, R. Seshadri, *Mater. Res. Bull.* **39**, 669 (2004).
14. C. B. Murray, D. J. Norris, M. G. Bawendi, *J. Am. Chem. Soc.* **115**, 870 (1993).

15. T. Hyeon, Chem. Comm. **8**, 927 (2003).
16. X. Gou, F. Cheng, Y. Shi, L. Zhang, S. Peng, J. Chen, P. Shen, J. Am. Chem. Soc. **128**, 7222 (2006).
17. H. Zhong, Y. Li, M. Ye, Z. Zhu, Y. Zhou, C. Yang, Y. Li, Nanotechnology **18**, 025602 (2007).
18. Q. Guo, S. J. Kim, M. Kar, W. N. Shafarman, R. W. Birkmire, E. A. Stach, R. Agarwal, H. W. Hillhouse, Nano Lett. **8**, 2982 (2008).
19. P. M. Allen, M. G. Bawendi, J. Am. Chem. Soc. **130**, 9240 (2008).
20. D. Pan. L. An, Z. Sun, W. Hou, Y. Yang, Z. Yang, Y. Lu, J. Am. Chem. Soc. **130**, 5620. (2008).
21. D. Wang, W. Zheng, C. Hao, Q. Peng, Y. Li, Chem. Commun. 2556 (2008).
22. K. H. Kim, Y. G. Chun, B. O. Park, K. H. Yoon, Mater. Sci. Forum **449-452**, 273 (2004).
23. J. Tang, S. Hinds, S. O. Kelly, E. H. Sagent, Chem. Mater. **20** (2008) 6906.
24. M. G. Panthani, V. Akhavan, B. Goodfellow, J. P. Schmidtke, L. Dunn, A. Dodabalapur, P. F. Barbara, B. A. Korgel, J. Am. Chem. Soc. **130** (2008) 16770.
25. Y.-H. A. Wang, N. Bao, L. Shen, P. Padhan, A. Gupta, J. Am. Chem. Soc. **129**, 12408 (2007).
26. H. Onnagawa, K. Miyashita, Jpn. J. Appl. Phys. **23**, 965 (1984).
27. J. L. Shay, J. H. Wemick, *Ternary Chalcopyrite Semiconductors*, Pergamon: Oxford, 1975, p. 118.
28. P. Rajaram, R. Thanagaraj, A. K. Sharma, A. Raza, O. P. Agnihotri, Thin Solid Films **100**, 111 (1983).
29. A. L. Efros, Sov. Phys. Semicond. **16**, 772 (1982).
30. P. W. Li, R. A. Anderson, R. H. Plovnick, J. Phys. Chem. Solids **40**, 333 (1979).
31. J. H. Schön, E. Bucher, Appl. Phys. Lett. **73**, 211 (1998).
32. S. Siebentritt, Thin Solid Films **480-481**, 312 (2005).
33. S. Levchenko, N. N. Syrbu, V. E. Tezlevan, E. Arushanov, J. M. Merino, J. Phys. D: Appl. Phys. **41**, 055403 (2008).

34. T. M. Hsu, *J. Appl. Phys.* **59**, 2538 (1986).

35. B. J. Stanbery, *Crit. Rev. Solid State Mater. Sci.* **27**, 73 (2002).

## APPENDIX II

### SHAPE-CONTROLLED SYNTHESIS OF SEMICONDUCTING CuFeS<sub>2</sub> NANOCRYSTALS

Reproduced in part with permission from [Wang, Y.-H. A. *et al. Solid State Sci.* **12**, 387-390 (2009) ] Copyright [2010] Elsevier Masson SAS.

#### 1. Introduction

Chalcopyrite, CuFeS<sub>2</sub> (CFS), is a naturally occurring mineral that was used as a material in ancient statuettes 2500 years ago.<sup>1</sup> CFS has a tetragonal structure with space group  $I\bar{4}2d$  and lattice constants  $a=5.289$  Å and  $c=10.423$  Å. The structure can be considered as a double sphalerite cell with an ordered arrangement of Cu and Fe ions in the lattice that are in tetrahedral coordination with sulfur. CuFeS<sub>2</sub> is a semiconductor with unusual optical, electrical and magnetic properties.<sup>2-4</sup> It has a small band gap of about 0.5-0.6 eV with a golden luster, but the conductivity is anomalously low.<sup>3</sup> CFS is also antiferromagnetic with a relatively high Néel temperature of 823 K.<sup>4</sup>

A number of compounds of the I-II-VI<sub>2</sub> family have the chalcopyrite structure, including CuInS<sub>2</sub>, CuInSe<sub>2</sub> and CuGaSe<sub>2</sub>. The In,Ga-based compounds and their solid solutions have band gaps in the range of 1.0 - 1.8 eV, and are of considerable interest as the photon absorber material in thin-film solar cells.<sup>5,6</sup> Use of semiconducting colloidal nanocrystals (NCs) of the chalcopyrites is a promising approach for low-cost fabrication of photovoltaics.<sup>7-9</sup> Both the tunability and the possibility of forming multiple electron-hole pairs<sup>10</sup> in NCs are attractive features for enhancing solar cell efficiency. Using composites consisting of a mixture of CuFeS<sub>2</sub> with In,Ga-based chalcopyrites NCs can potentially help extend the absorption of solar radiation to longer wavelengths (< 1.0 eV).

Most of the reported results thus far on CFS have been in the bulk, either using naturally occurring or synthetic single crystal and polycrystalline samples. There has been very limited work on the synthesis and characterization of nanocrystalline CFS. Silvester *et al.* in 1991 reported the use of a hydrothermal method for the preparation and characterization of optically transparent colloidal CFS.<sup>11</sup> More recently, Wang *et al.* used a modified solvothermal method utilizing the metal halides and ammonium sulfide in a solution of ethylenediamine for the synthesis of CFS nanowires.<sup>12</sup> In recent years, a variety of metal-organic precursors have been utilized extensively for the synthesis of metal sulfide NCs and thin films. In particular, metal dithiocarbamates and thiocarboxylates are attractive single molecular precursors since the thio-ligands can be readily detached and metal sulfides can form at relatively low temperature.<sup>13-16</sup> Monodisperse CdS and ZnS semiconducting nanocrystals have been synthesized using bis[methy(n-hexane)dithio]carbamate precursor.<sup>14</sup> Heavy metal sulfides, such as EuS, PtS and PdS, nanocrystals have also been synthesized using similar dithiocarbamate precursors.<sup>15,16</sup> Herein, we report on the facile synthesis of shape-controlled CuFeS<sub>2</sub> nanocrystals that are nearly monodisperse and readily form a colloidal suspension. The process involves the thermal decomposition and reaction of the metal-dithiocarbamate or acetylacetonate precursors with sulfur in an organic solvent mixture.

## 2. Experimental

For the synthesis of spherical CuFeS<sub>2</sub> nanocrystals, copper (II) ethyldithiocarbamate and iron ethyldithiocarbamate were used as precursors. The dithiocarbamate-based precursors were prepared in the laboratory following synthesis procedures reported in the literature.<sup>17,18</sup> All the reactions were performed in a fume hood under an inert atmosphere. In a typical reaction for the synthesis of CFS NCs with spherical morphology, 2 mmol of sulfur (S) was dissolved

completely in 1 ml tri-octylphosphine (TOP). Subsequently, 10 ml of oleylamine (OA) was added and the mixture heated up to 180°C. Separately, 0.2 mmol each of  $\text{Cu}[\text{S}_2\text{CN}(\text{C}_2\text{H}_5)_2]_2$  and  $\text{Fe}[\text{S}_2\text{CN}(\text{C}_2\text{H}_5)_2]_3$  were dissolved in a mixture of 2 ml oleic acid (OA) and 2 ml dichlorobenzene (DCB) at 50 °C under vacuum and then backfilled with nitrogen. After the S/TOP/OA solution reached 180°C, the cation mixture was injected under nitrogen atmosphere and the resultant mix heated back to 180°C. The reaction mixture was maintained at this temperature for one hour while being continually stirred, during which the color of the solution turned increasingly dark. After cooling down to room temperature, a mixture of hexane and ethanol was added to the solution and a black product precipitated via centrifugation.

A similar procedure was used for the synthesis of pyramidal  $\text{CuFeS}_2$  NCs. The difference being that copper acetylacetonate and  $\text{Fe}[\text{S}_2\text{CN}(\text{C}_2\text{H}_5)_2]_3$  were used as precursors. The copper precursor was obtained commercially from Aldrich while the Fe precursor was prepared in the laboratory as mentioned earlier. Unlike the synthesis of spherical nanocrystals, both the precursors were dissolved in 2 ml DCB without any OA. Addition of OA resulted in a broad size distribution of the NC product with non-uniform geometry.

The morphology and size distribution of the NCs was determined using transmission electron microscopy (TEM, FEI Tecnai F-20). For this purpose the NCs were dispersed in hexane and spray-dried on a TEM copper grid. X-ray powder diffraction (XRD, Bruker D8) was used to study the structure of the NCs, and the optical properties determined from measurement of the UV–Vis diffuse reflectance spectra (UV-Vis-NIR, Varian Cary 5G). For the UV-Vis measurements, the samples were dispersed in hexane with ~0.02 % OLA added as surfactant. The composition of the NCs was determined using energy-dispersive x-ray analysis (Philips XL-

30). X-ray photoelectron spectroscopies (XPS) measurements were performed using a Kratos Axis 165 XPS.

### 3. Results and Discussions

By varying the synthesis conditions we have determined that about 100 % excess sulfur is optimum for obtaining NCs with more uniform morphology, stoichiometric composition and a narrow size distribution. For the synthesis of the spherical NCs, OA by itself is not suitable as a solvent for completely dissolving the precursors. Hence a mixture with DCB is used. Besides acting as a surfactant, the presence of OA also prevents formation of  $\text{Cu}_2\text{S}$ . With using only DCB as a solvent  $\text{Cu}_2\text{S}$  is produced as a secondary phase. As mentioned earlier, for the synthesis of pyramidal NCs only DCB is used as solvent to obtain a narrow size distribution.

The morphology of the synthesized materials has been investigated using TEM. As seen in Fig. 1, the NCs synthesized using iron and copper dithiocarbamates as precursors exhibit a

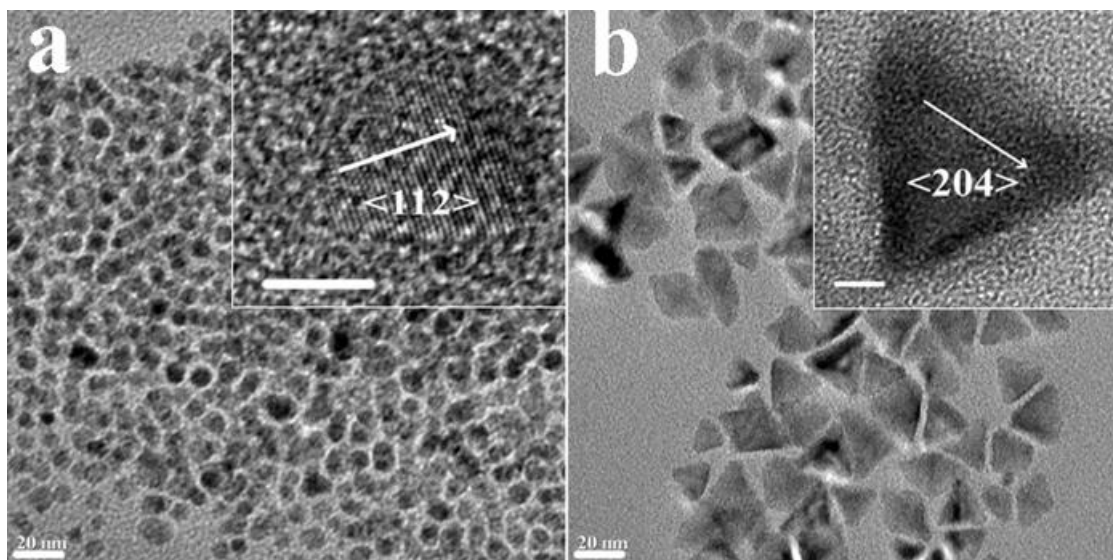


**Figure 1.** TEM images of  $\text{CuFeS}_2$  NCs with a) spherical and b) pyramidal morphology (marked scale bars are 20 nm) with HRTEM images shown in the insets (marked scale bars are 5 nm)

spherical morphology (Fig 1a), while those obtained from a mixture of iron diethyldithiocarbamate and copper acetylacetonate display a pyramidal morphology (Fig. 1b). The average sizes of the spherical and pyramidal NCs are  $12\pm 4$  nm and  $30\pm 5$  nm, respectively, which calculated by 200 nanocrystals. The high resolution TEM (HRTEM) images of the NCs are shown in the insets to the two figures, with the marked scale bar corresponding to 5 nm. Clear lattice fringes are observed in the HRTEM image with a spacing of  $d = 0.303$  nm (spherical NCs) and 0.185 nm (pyramidal NCs), corresponding to the (112) and (204) lattice planes of the chalcopyrite phase, respectively.

As seen in Fig. 2, the peak positions and relative intensities of all the x-ray diffraction peaks for both the spherical and pyramidal morphology NCs match well with the powder diffraction data for the chalcopyrite  $\text{CuFeS}_2$  phase which has a tetragonal structure (JCPDS No. 83-0983). The broad background signal centered at around  $25^\circ$  is from the glass slide used to hold the powder sample. As expected, the sample peaks are quite broad because of the small

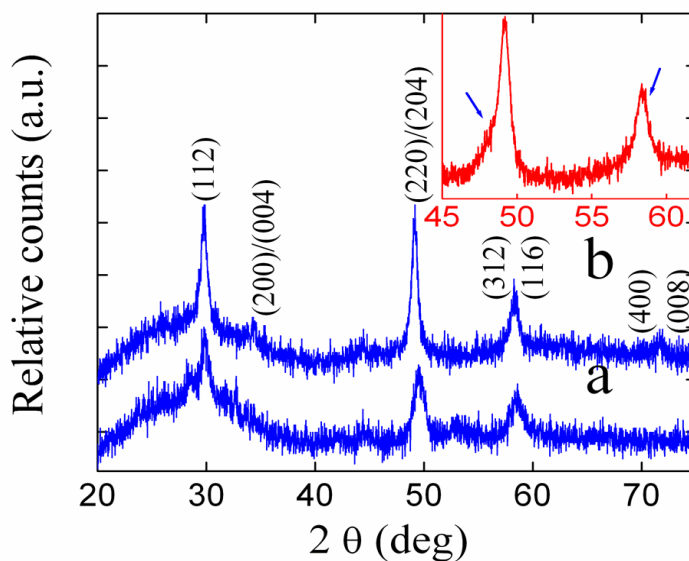


**Figure 2.** X-ray powder diffraction pattern of a) spherical, and b) pyramidal morphology  $\text{CuFeS}_2$  NCs. The inset shows the diffraction peaks of the pyramidal NCs displayed on an expanded scale in the  $2\theta$  range of  $45\text{--}65^\circ$

particle size, with the peak width increasing with decreasing size. From the peak width, the average particle size can be estimated using Debye-Scherrer equation. The peak at  $30^\circ$  is used to determine the average particle size and the calculated average particles sizes are 15.1 nm and 31.5 nm for spherical morphology and pyramidal morphology NCs, respectively. These values are very close to the average sizes observed in the TEM images. The inset shows the diffraction pattern of the pyramidal NCs on an expanded scale in the  $2\theta$  range of  $45\text{-}65^\circ$ . Because of the small particle size, splitting of the 220/240 and 312/116 peaks, which is expected because of the tetragonal distortion, is not observed. Instead, broad unsymmetrical peaks are observed in both regions. We have confirmed the composition of the NCs using energy dispersive x-ray analysis, which indicates that the Cu:Fe:S concentration to be very close to the expected 1:1:2 ratio for both the samples.

The optical absorbance spectra of NCs for both morphologies, measured in dilute hexane dispersion, exhibit a broad absorption in the visible with a tail extending to longer wavelengths. We have determined the absorbance onset by plotting  $(Ah\nu)^2$  versus  $h\nu$  ( $A$  = absorbance,  $h$  =

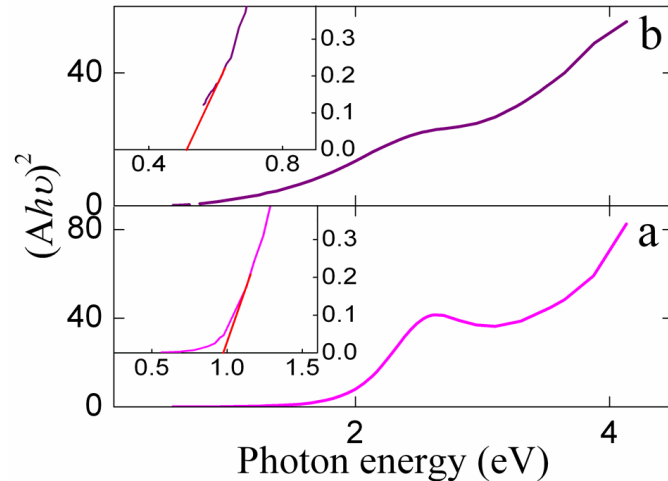


**Figure 3.** Room temperature absorption spectra of a) spherical and b) pyramidal NCs. Insets show the extrapolation of the spectra in the band edge region for determining the band gap.

Planck's constant and  $\nu$  = frequency ) and extrapolating the slope in the band edge region, as shown in Fig. 3.<sup>8,19-21</sup> The absorbance peaks for the spherical and pyramidal NCs occur at around 480 nm and 550 nm, respectively. From the long wavelength extrapolation of the band edges, the band gaps are determined to be 0.95 eV and 0.52 eV for the spherical and pyramidal NCs, respectively. While the band gap of the pyramidal NCs is very close to the bulk value (0.5-0.6 eV), the band gap determined for the spherical nanocrystals is significantly larger. This is likely because of size confinement effect for the much smaller size spherical NCs.<sup>22</sup>

The XPS spectra of CuFeS<sub>2</sub> NCs with spherical morphology are shown in Fig. 4. Based on the complete spectra, all the peaks can be assigned to copper, iron or sulfur. From the Cu2*p* core-

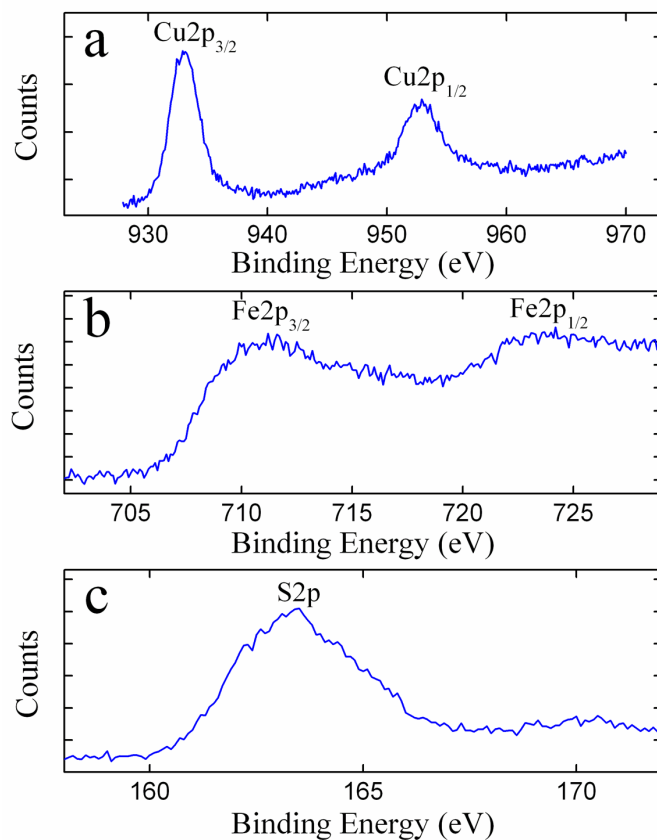


**Figure 4.** XPS measurements of spherical CuFeS<sub>2</sub> NCs in the region of: (a) Cu 2*p* core level, (b) Fe 2*p* core level, and (c) S 2*p* core level.

level spectral region (Fig. 4a), the observed binding energy value for  $\text{Cu}2p_{3/2}$  (932.8 eV) is close to the reported value for  $\text{Cu}^+$ <sup>23</sup>. No  $\text{Cu}2p_{3/2}$  satellite peak around 942 eV<sup>24</sup> attributed to  $\text{Cu}^{2+}$  is observed. Similarly, the binding energy of observed  $\text{Cu}2p_{1/2}$  (952.8 eV) peak can be attributed to  $\text{Cu}^+$ . The  $\text{Fe}2p$  core-level spectra region (Fig. 4b) indicates that the binding energy for  $\text{Fe}2p_{3/2}$  (710.8 eV) and  $\text{Fe}2p_{1/2}$  (723.6 eV) are in good agreement with the respective values for  $\text{Fe}^{3+}$ . The  $\text{S}2p$  core-level spectral region (Fig. 4c) provides the binding energy value for  $\text{S}2p_{3/2}$  (163.2 eV), which is similar to that reported by Hu *et al.*<sup>25</sup> Similar XPS spectra have been obtained for the pyramidal morphology NCs. Hence, the XPS analysis is consistent with the valence states for  $\text{CuFeS}_2$  NCs being  $\text{Cu}^+$ ,  $\text{Fe}^{3+}$  and  $\text{S}^{2-}$ .<sup>26</sup>

#### 4. Conclusion

In conclusion, we have synthesized both spherical and pyramidal geometry  $\text{CuFeS}_2$  semiconductor NCs via a simple solution-based route involving the reaction of metal-dithiocarbamate or metal-acetylacetonate precursors. The NCs exhibit a tetragonal structure with the expected valence states of  $\text{Cu}^+$ ,  $\text{Fe}^{3+}$  and  $\text{S}^{2-}$  for the ions. While the larger size pyramidal NCs exhibit a band gap (0.52 eV) close to the bulk, a larger band gap (0.95 eV) is obtained for the smaller spherical NCs because of size confinement effect. Because of the very broad absorption characteristics and tunable band gap, the  $\text{CuFeS}_2$  NCs are potentially useful for the fabrication of solar cells in combination with In, Ga - based chalcopyrites.

#### 5. References

1. P. Manca, *Nuovo Cimento D* **2**, 1609 (1983).
2. I. G. Austin, G. Goodman, A. Pengelly, *J. Electrochem. Soc.* **103**, 609 (1956).

3. B. I. Boltaks, N. N. Tarnovski, *Zh. Tekh. Fiz.* **25**, 402 (1955).
4. G. Donnay, L. M. Corliss, J. D. H. Donnay, N. Elliott, J. M. Hastings, *Phys. Rev.* **112**, 1917 (1958).
5. V. Nadenau, D. Braunger, D. Hariskos, C. Kaiser, M. Ruckh, R. Schaffer, T. Schmid, *Prog. Photogr. Res. Appl.* **3**, 363 (1995).
6. S. Niki, P. J. Fons, A. Yamada, O. Hellman, T. Kurafuji, S. Chichibu, H. Nakanishi, *Appl. Phys. Lett.* **69**, 647 (1996).
7. J. Tang, S. Hinds, S. O. Kelly, E. H. Sagent, *Chem. Mater.* **20**, 6906 (2008).
8. M. G. Panthani, V. Akhavan, B. Goodfellow, J. P. Schmidtke, L. Dunn, A. Dodabalapur, P. F. Barbara, B. A. Korgel, *J. Am. Chem. Soc.* **130**, 16770 (2008).
9. Y.-H. A. Wang, C. Pan, N. Bao, A. Gupta, *Solid State Sci.* **11**, 1961 (2009).
10. A. J. Nozik, *Chem. Phys. Lett.* **457**, 3 (2008).
11. E. J. Silvester, T. W. Healy, F. Grieser, B. A. Sexton, *Langmuir* **7**, 19 (1991).
12. M. X. Wang, L. S. Wang, G. H. Yue, X. Wang, P. X. Yan, D. L. Peng, *Mater. Chem. Phys.* **115**, 147 (2009).
13. J. J. Vittal, M. T. Ng, *Acc. Chem. Res.* **39**, 869 (2006).
14. B. Ludolph, M. A. Malik, P. O'Brien, N. Revaprasadu, *Chem. Comm.* 1849 (1998).
15. M. D. Regulacio, S. Kar, E. Zuniga, G. Wang, N. R. Dollahon, G. T. Yee, S. L. Stoll, *Chem. Mater.* **20**, 3368 (2008).
16. M. A. Malik, P. O'Brien, N. Revaprasadu, *J. Mater. Chem.* **12** (2002) 92.
17. J.-H. Park, M. Afzaal, M. Kemmler, P. O'Brien, D. J. Otway, J. Raftery, J. Waters, *J. Mater. Chem.* **13**, 1942 (2003).
18. X. Chen, Z. Wang, X. Wang, J. Wan, J. Liu, Y. Qian, *Inorg. Chem.* **44**, 951 (2005).
19. H. Onnagawa, K. Miyashita, *Jpn. J. Appl. Phys.*, **23**, 965 (1984).
20. J. L. Shay, J. H. Wemick, *Ternary Chalcopyrite Semiconductors*, Pergamon: Oxford, 1975, p. 118.
21. P. Rajaram, R. Thanagaraj, A. K. Sharma, A. Raza, O. P. Agnihotri, *Thin Solid Films* **100**, 111 (1983).

22. A. P. Alivisatos, *Science* **271**, 225 (1996).
23. T. Kuzuya, K. Itoh, M. Ichidate, T. Wakamatsu, Y. Fukunaka, K. Sumiyama, *Electrochimica Acta* **53**, 213 (2007).
24. L. D. Partain, R. A. Schnerder, L. F. Donaghey, P. S. Meleod, *J. Appl. Phys.* **57**, 5056 (1985).
25. J. Q. Hu, B. Deng, K. B. Tang, C. R. Wang, Y. T. Qian, *J. Mater. Res.* **12**, 3411 (2001).
26. C. Boekema, A. M. Krupski, M. Varasteh, K. Parvin, F. van Til, F. van der Woude, G. A. Sawatzky, *J. Mag. Mag. Mater.* **272-276**, 559 (2004).